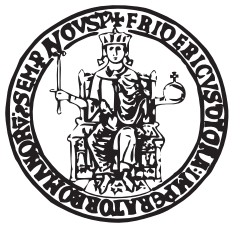

Università degli Studi di Napoli
Dipartimento di Ingegneria Industriale
Scuola di dottorato in Ingegneria Aerospaziale,
Navale e della Qualità - XXV ciclo

Tesi di dottorato in
Ingegneria Aerospaziale

INTERFACIAL INSTABILITIES OF TWO-FLUID FLOWS

ANNAGRAZIA ORAZZO

Tutor:
Prof. Ing. Luigi de Luca
Prof. Ing. Gennaro Coppola

Coordinatore:
Prof. Ing. Luigi de Luca

Aprile 2013

ANNAGRAZIA ORAZZO

INTERFACIAL INSTABILITIES OF TWO-FLUID FLOWS

Tornano in alto ad ardere le favole.
Cadranno colle foglie al primo vento.
Ma venga un altro soffio,
ritornerà scintillamento nuovo.

— Giuseppe Ungaretti

Dedicato a colui che mi ha insegnato a guardare le stelle …

Abstract

Many flows in industry and in nature are two-fluid flows of immiscible fluids. Among them, the cases of parallel flowing gas-liquid layers in plane geometry and of oil-water arranged as Core-Annular Flow (CAF) in circular pipe are deeply investigated here. These are significant configurations, respectively, for the atomization of fuel in thermal engine and for the lubricated pipelining in petroleum industry.

Two-fluid flows are often unstable. Aim of this thesis is to analyze the development of instability taking into account all the typical features associated with two-fluid flows: large density and viscosity ratios, surface tension acting on the interface separating the different fluids and the different spatial scales interested by the evolution of the interface.

This analysis is very complex because it is necessary to distinguish between linear and nonlinear effects, normal mode and transient growth and delicate effects of viscosity even at high Reynolds numbers. Both linear stability theory and direct numerical simulations have been used.

A linear stability analysis of these flows has been worked out only recently (see [1], [2], etc ...). It has let to verify that interfacial modes are the most unstable ones and represent the leading mechanism of primary instability.

Numerical simulations, based on Volume of Fluid (VOF) method, have allowed to investigate the nonlinear development of this interfacial instability that, for gas-liquid flows characterizing the atomization process, is the main responsible of breakup and droplets formation. These simulations have displayed the formation and the evolution of a new type of instability: a nonlinear

single wave Kelvin-Helmholtz instability. This structure has been extensively discussed and characterized.

Two different codes have been used: an in-house modified version of SURFER [3] and GERRIS flow solver, a new generation VOF code coupling classical VOF algorithms with the adaptive mesh refinement [4].

Regarding CAF, in order to explain the disagreement between classic results of linear modal stability analysis and some experimental findings [5], a nonmodal analysis has been performed. It has highlighted how the instability of this flow is governed by transient energy amplification of infinitesimal three-dimensional disturbances that lead to particular flow patterns, such as emulsifications or water drops in oil, and play an important role in transition to turbulence.

KEY WORDS: gas-liquid flows, interfacial instability, VOF simulations, single Kelvin-Helmholtz wave, linear stability analysis, CAF, transient growth.

Preface

This doctoral thesis is a theoretical/numerical thesis and deals with the analysis of interfacial instabilities of two-fluid flows. The main advisor of this project is Prof. Luigi de Luca and Prof. Gennaro Coppola acts as co-advisor.

The first chapter is an introduction to the basic characteristics of the considered flows and to the numerical methods used. The presented results are divided in two chapters: in chapter 2 a two-phase flow typical of atomization process is analyzed by means of both linear stability theory and Volume Of Fluid simulations in plane geometry; in chapter 3 the instability of a two-fluid flow arranged as Core-Annular Flow in cylindrical pipe is investigated from the point of view of linear nonmodal analysis.

The atomization studies have been inspired by an academic collaboration with AVIO s.p.a. and part of them has been developed during a stage at *Institute Jean Le Ronde d'Alembert* under the supervision of Prof. Jérôme Hœpffner.

Journal papers arisen from this work are:

1. A. Orazzo, G. Coppola, L. de Luca, 2011, Single-Wave Kelvin-Helmholtz instability in non-parallel channel flow, *Atomization and Spray*, **21** 775-785.

2. G. Coppola, A. Orazzo, L. de Luca, 2012, Non-modal instability of core-annular flow, *International Journal of Nonlinear Science and Numerical Simulations*, **13**, 405-416.

3. A. Orazzo, J. Hœpffner, 2012, The evolution of a localized nonlinear wave of the Kelvin-Helmholtz instability with gravity, *Physics of Fluids*, **24**, 112106.

4. A. Orazzo, G. Coppola, L. de Luca, 2013, Transient amplifications of energy in Core-Annular Fow, submitted to *Journal of Fluid Mechanics*.

Parts of the results have been presented at:

1. **9th European Fluid Mechanics Conference - EFMC9**, Rome, Italy, 9th-13th September 2012.
2. **64th Annual Meeting of the APS Division of Fluid Dynamics**, Baltimore, USA, 20th-22nd November 2011.
3. **International Conference on Multiphase Flow in Industrial Plants**, Ischia, Italy, 21st-23rd September 2011.
4. **24th European conference on Liquid Atomization and Spray Systems- ILASS**, Estoril, Portugal, 5th-7th September 2011.
5. **8th European Fluid Mechanics Conference - EFMC8**, Bad Reichenhall, Germany, 13th-16th September 2010.
6. **62th Annual Meeting of the APS Division of Fluid Dynamics**, Minneapolis, USA, 22nd-24th November 2009.
7. **3rd European Postgraduate Fluid Dynamics Conference**, University of Nottingham, 13th-16th July 2009.

Contents

List of Figures

1

Introduction

Bicomponent flows are coupled flows of a fluid and another constituent, either solid or another fluid, with different material properties. The examples that will be treated in this thesis are the flow of two immiscible liquids and the gas-liquid flow, called two-phase flow.

Two-fluid flows play an essential role in many natural phenomena (geophysics, meteorology...), fig. 1.1, and human enterprises. We come across examples of these flows, in particular of gas-liquid flows, in our everyday life, such as in the kitchen (drinking, washing, cooking...), taking a shower, using pharmaceutical sprays and cosmetics. They are also used for our entertainment, just think about water games of fountains, and for our security, for example to help firemen. Similarly these flows are present in abundance in industrial applications: lubricated transports, sprays, jet engine technology (fig. 1.2), manufacturing, etc...

Understanding the dynamics of two-fluid flows is a challenging subject of both engineering and scientific importance and the literature is very extensive. From a mathematical point of view, multifluid problems are notoriously difficult: not only the governing equations are highly nonlinear, but the position of the fluid boundary must generally be found as a part of the solution. The basic analytical tool used is the linear stability analysis which does not allow to investigate the effects of nonlinear mechanisms, dominant in the break-up and instability process. On the experimental side, the phenomena characterizing these flows often happen on

Figure 1.1: Waves on the sea. From flickr.com.

scales of space and time where the visualization is difficult or impossible. For all these reasons numerical simulations seem to be the most valuable means to treat these problems.

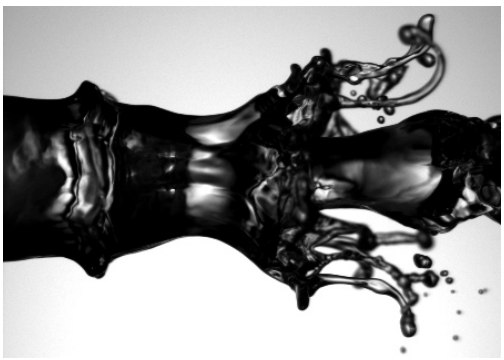

Figure 1.2: Destabilization of slow water jet by a fast coaxial air stream. From [6].

1.1 Basic equations

The derivation of the equations governing the flows where an interface separates the fluids is based on three general hypothesis: the continuum hypothesis, the hypothesis of a sharp interface and the consideration of only the intermolecular forces (the van der Waals forces) that play an important role in the interface physics and are modeled as surface tension.

Although real fluids are made by atoms and molecules, the

assumption that they can be treated as a continuum is usually an excellent approximation. In fact, molecular simulations, where the motion of many individual molecules is followed for long times, show that the fluid behaves as a continuum for a surprisingly small number of molecules (see [13]). The assumption of a sharp interface is justified by considering that the transition from one fluid to another, and thus the change of density, viscosity, and all the material properties of fluids, occurs on very small scales that allow us to assume the interface with a vanishing thickness.

Beyond these three hypothesis, we mostly deal with incompressible flows and Newtonian fluids.

The basic principles to obtain the governing equations of two-fluid flows are the same used for the single-fluid flows: the conservation of mass, momentum and energy (the latter will be not considered here because for the flow configurations investigated the variations of energy are neglected). Of course, after the derivation of the governing equations for each fluid in play, it is necessary to discuss the mathematical representation of a moving interface and the appropriate jump conditions needed to couple the equations across the interface.

The principle of conservation of mass states that mass cannot be created or destroyed. Therefore, if we considered a volume V, fixed in the space, the mass inside this volume can only change if mass flows in or out through its boundary S. Similarly, the momentum conservation principle states that the rate of change of fluid momentum in the fixed volume V is the difference in momentum flux across the boundary S plus the forces acting on the volume (the gravitational force, $\mathrm{f} = \rho \mathrm{g}$). The equations of fluid motion for incompressible Newtonian flow in convective form are:

$$\begin{aligned} \nabla \cdot \mathrm{V} &= 0 \\ \rho \frac{\mathrm{D}\mathrm{V}}{\mathrm{D}t} &= -\nabla p + \mathrm{f} + \nabla \cdot (2\mu \mathbf{D}) \end{aligned} \tag{1.1}$$

where the last term in the momentum equation, $\mathbf{D}$, represents the deformation part of the symmetric stress tensor $\mathbf{T}$, which for Newtonian fluids is expressed by the following constitutive relation:

$$\mathbf{T} = (-p + \lambda \nabla \cdot \mathrm{V})\mathbf{I} + 2\mu \mathbf{D} \tag{1.2}$$

Here, $\mathbf{I}$ is the unit tensor, p is the pressure, μ the viscosity, $\mathbf{D} = \frac{1}{2}(\nabla \mathbf{V} + \nabla \mathbf{V}^T)$ and λ is the second coefficient of viscosity, usually negligible.

The second of equations 1.1 is the *Navier-Stokes* equation.

1.2 Interface description

Following the motion in time of a deformable interface separating different fluids or phases is the central point of analyzing multi-fluid flows. There are several different ways in which the interface can be described geometrically. All the possible representations can be divided in two groups: explicit representations and implicit representations.

Belonging to the first group is the description of the location of the interface by a single-valued function of one (in two dimensions) or two (in three dimensions) coordinates. For example, for a thin liquid layer in two dimensions, it is possible to define the height function h

$$y = h(x, t) \tag{1.3}$$

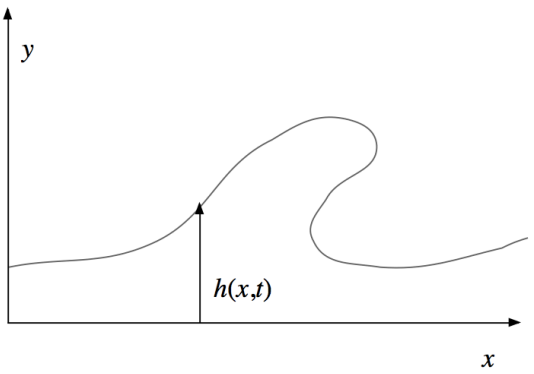

Figure 1.3: The simplest way to parametrize an interface through the heigh function $y = h(x, t)$. From [7].

The fig. 1.3 shows the limitation of this approach: if part of the interface overhangs, h becomes a multivalued function.

To handle interfaces of arbitrary shape it is possible to parametrize them by introducing, in two dimensions, a new coordinate u, such that the location of the interface is given by

$$\mathrm{x} = (x(u), y(u)) \tag{1.4}$$

(for three-dimensional space we need to take two independent coordinates). Fig. 1.4 shows a closed contour separating fluid 1 from fluid 2 described in this way. Although u can be any parametrization of the curve shown, the simplest case is to choose the arc length s, where $\mathrm{d}s^2 = \mathrm{d}x^2 + \mathrm{d}y^2$.

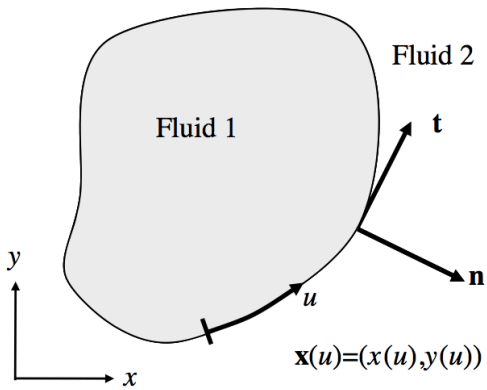

Figure 1.4: Parametric representation of the interface where the coordinate u follows the interface. From [7].

Implicit representations of the interface are the ones in which the interface is not described by identifying the location of every point belonging to it but by a marker function defined in the whole domain. These marker function may assume many forms. For example, we can use a characteristic discontinuous functions, also know as the step function or the *Heaviside function*, defined by:

$$H(x) = \begin{cases} 1 & \text{fluid 1} \\ 0 & \text{fluid 2} \end{cases} \tag{1.5}$$

Given H, the interface is identified with the sharp change from one value to the other (fig. 1.5).

The interface can be described also by a a smooth function F and, in this case, its position is identified with a particular value of this function, say $F = 0$ (fig. 1.6). Obviously, on one side of the interface we have $F < 0$ and on the other side $F > 0$. This representation as a contour line with a specific value is used in *level set* methods.

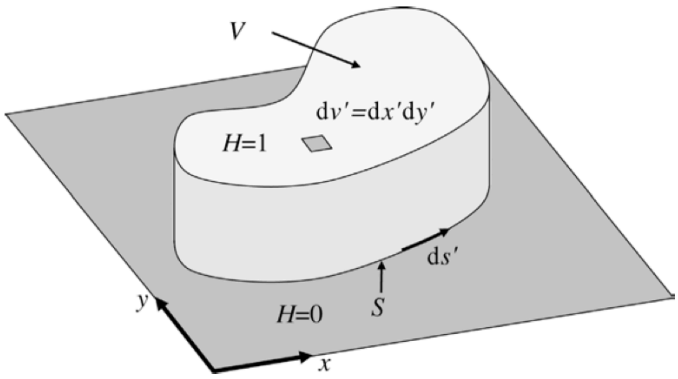

Figure 1.5: Implicit representation of the interface where a step function identify the region occupied by a specific fluid. From [7].

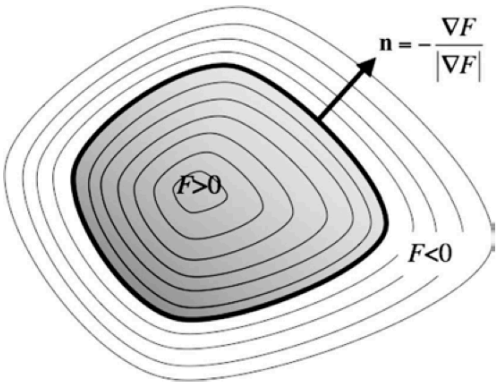

Figure 1.6: Identification of the interface by a level-set function. From [7].

Surface tension

A liquid flows readly and yet it can adopt extremely stable shapes, for istance a drop of oil in water forms a perfect sphere that is smooth on an atomic scale and is hardly deformable (fig. 1.7). Here we summarize the physical origin of the phenomenon of surface tension.

Figure 1.7: Oil bubbles in a glass of water. From the album of m_elam, flickr.com.

At the interface between two different fluids all the material properties change rapidly over distances comparable to the molecular separation scale. Since a molecule at the interface is exposed to a different environment than inside the material, it will also have a different binding energy (the boundary molecules have a higher energy). In the continuum limit this difference in molecular binding energy manifests itself as a macroscopic *surface energy density*. To reduce the energy state of a fluid, it is necessary to have less high energy molecules: this results into a minimized surface area. Consequently, a surface will assume the smoothest shape it can. The excess of energy at the interface is expressed as

$$\mathrm{d}E^{\sigma} = \sigma \mathrm{d}s \tag{1.6}$$

where $\mathrm{d}s$ is the infinitesimal interface (or, in three dimensions,

surface) area and σ is a material property, usually referred to as *surface tension*.

In fluid mechanics the surface tension is not defined in terms of a surface energy, but rather as a force per unit of length acting perpendicularly on any segment of the interface. Suppose we want to increase the surface area by an amount $\mathrm{d}A$. The work required is proportional to the number of molecules that must be brought up to the surface:

$$\delta W = \sigma \mathrm{d}A \tag{1.7}$$

where dimensionally $[\sigma] = N/m$.

As explained in the work of Laplace [14], surface tension is at the origin of a jump in pressure which occurs passing through a curved interface. We take the example of a drop of oil (o) in water (w), fig. 1.7. In order to lower its surface energy, the drop adopts a spherical shape of radius R. If the oil-water interface is displaced by an amount $\mathrm{d}R$, the work done by the pressure and capillary force can be written as

$$\delta W = -p_o \mathrm{d}V_o - p_w \mathrm{d}V_w + \sigma_{ow} \mathrm{d}A \tag{1.8}$$

where $\mathrm{d}V_o = 4\pi R^2 \mathrm{d}R = -\mathrm{d}V_w$ and $\mathrm{d}A = 8\pi R \mathrm{d}R$ are the increase in volume and surface, p_o and p_w are the pressure in the oil and the water, and σ_{ow} is the interfacial tension between oil and water.

The condition for a mechanical equilibrium is $\delta W = 0$, which amounts to

$$\triangle p = p_o - p_w = \frac{2\sigma_{wo}}{R} \tag{1.9}$$

It is possible to generalize this law to a generic interface considering that the increase in hydrostatic pressure $\triangle p$ that occurs upon traversing the boundary between two fluids is equal to the product of the surface tension σ and the curvature of the surface $c = \frac{1}{R} + \frac{1}{R'}$, where R and R' are the curvature radii.

$$\triangle p = \sigma c \tag{1.10}$$

Capillary effects may be represented numerically by a tensor $\mathbf{T}^\sigma$ tangent to the interface and given by

$$\mathbf{T}^\sigma = \sigma(\mathbf{I} - \mathrm{nn}) \tag{1.11}$$

where $\mathbf{I}$ is the Kronecker symbol tensor, δ_{ij}, and n is the unit vector normal to the interface.

The force on a surface element of area S, bounded by a contour L, is the integral of $\mathbf{T}^{\sigma}$ on its edges:

$$\delta \mathrm{F}_{\sigma} = \oint_{L} \mathbf{T}^{\sigma} \cdot \mathrm{n}\, \mathrm{d}l = \int_{S} \nabla \cdot \mathbf{T}^{\sigma}\, \mathrm{d}s \tag{1.12}$$

Taking the limit of eq. 1.12 as the surface area shrinks to a point, we define the surface force per unit of area as

$$\mathrm{f}_{\sigma} = \nabla \cdot \mathbf{T}^{\sigma} = \nabla \cdot \sigma \mathbf{I} = \sigma \nabla \cdot \mathbf{I} + \mathbf{I} \cdot \nabla \sigma \tag{1.13}$$

The first term can be shown to be $\sigma c \mathrm{n}$ and the second term is simply $\nabla \sigma$. Thus,

$$\mathrm{f}_{\sigma} = \sigma c \mathrm{n} + \nabla \sigma \tag{1.14}$$

where c represents the curvature of the interface and the last term, the surface gradient of σ, is obviously zero for constant surface tension (the case considered in this thesis).

"Two-fluid formulation": jump conditions

The two-fluid formulation of the flow of two immiscible fluids is based on the decomposition of the domain into two subdomains filled with an individual fluid. The usual Navier-Stokes equations have to be written for any subdomain and, to unify the flow field, we need to derive some interface conditions. These conditions are derived using the mass and momentum conservation, introducing an additional term for surface tension.

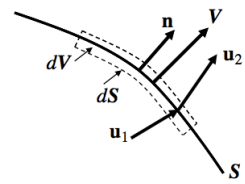

Figure 1.8: A thin control volume dV with boundary dS including a portion of the interface S. From [7].

The jump condition for normal velocity is derived applying the conservation principle to the control volume dV shown in fig. 1.8. Since the thickness is taken to zero, the mass flow into the control volume must be equal to the flow out. If the velocity on the two side are V_1 and V_2 and the normal velocity of the interface is V, we have

$$\rho_1(\mathrm{V}_1 \cdot \mathrm{n} - V) = \rho_2(\mathrm{V}_2 \cdot \mathrm{n} - V) = \dot{m} \tag{1.15}$$

This is the Rankine-Hugoniot condition. If there is no change of phase, then $\dot{m} = 0$. For incompressible flow this condition must

hold for arbitrary density ratio, thus

$$V = \mathrm{V}_1 \cdot \mathrm{n} = \mathrm{V}_2 \cdot \mathrm{n} \tag{1.16}$$

Mass conservation does not impose restriction on the tangential velocity components. Indeed, inviscid fluids are usually assumed to slip at the interface, while, for viscous fluid it is experimentally observed that no slip takes place.

In conclusion, without phase change and with incompressible fluids, the interfacial condition for viscous fluid is simply $\mathrm{V}_1 = \mathrm{V}_2$, or

$$\langle \mathrm{V} \rangle = \mathbf{0} \tag{1.17}$$

where the symbol $\langle \cdot \rangle$ represents the jump of a quantity across the interface.

Applying the conservation of the momentum (the second eq. of 1.1), including the surface force f_σ, to the control volume of fig. 1.8, we obtain a jump of the stress tensor $\mathbf{T}$ across the interface

$$-\langle \mathbf{T} \rangle \cdot \mathrm{n} = \sigma c \mathrm{n} \tag{1.18}$$

This condition may be split into a normal and tangential stress components

$$\begin{aligned} -\langle -p + 2\mu \mathrm{n} \cdot \mathbf{D} \cdot \mathrm{n} \rangle &= \sigma c \\ -\langle 2\mu \mathrm{t} \cdot \mathbf{D} \cdot \mathrm{n} \rangle &= 0 \end{aligned} \tag{1.19}$$

where t is the unit tangent vector to the interface for the two-dimensional case.

The jump conditions and the partial differential equations for a Newtonian, incompressible fluid without phase change are summarized in the following system

$$\begin{aligned} \langle \mathrm{V} \rangle &= \mathbf{0} \\ -\langle -p + 2\mu \mathrm{n} \cdot \mathbf{D} \cdot \mathrm{n} \rangle &= \sigma c \\ -\langle 2\mu \mathrm{t} \cdot \mathbf{D} \cdot \mathrm{n} \rangle &= 0 \\ \nabla \cdot \mathrm{V} &= 0 \\ \rho \frac{\mathrm{D}\mathrm{V}}{\mathrm{D}t} &= -\nabla p + \mathrm{f} + \mu \nabla^2 \mathrm{V} \end{aligned} \tag{1.20}$$

The first three jump conditions are applied on the interface while the last two in the bulk of each fluid. Together with boundary conditions on the wall and exit and entry conditions, the eqs. 1.20 form a complete set for flows with interfaces.

1.3 Linear Stability Analysis

The "two-fluid" formulation is used to perform the linear stability analysis of two-fluid flows.

Investigations on linear stability for a single fluid date back to Kelvin and Helmholtz in the 19th century, but only in the early 20th century, Heisenberg, Lin, Tollmien and Schlicting found that viscosity may produce or contribute to the instability by modifying the inviscid perturbations, [15].

Viscosity effects are even more significant for two-fluid flows: the viscosity difference at the interface can give rise to instabilities neither inviscid nor Tollmien-Schlichting type. The first who studied this instability was Yih [16]. Subsequent works on this subject were made by Özgen [17], Renardy [18], as well as Hooper and Boyd [19].

The huge amount of literature on the stability of parallel two-fluid flows, both in the context of liquid-liquid as well of gas-liquid flows, shows that this type of flow is susceptible to instabilities of various kinds. Besides instability caused by viscosity stratification, mentioned above, instability can results from density stratification, velocity profile curvature or from shear effects in one of the constitutive phases. In fact, unlike for the single-fluid case stability problem where the Reynolds number is the only parameter in play, the formulations of two-fluid stability problem requires at least six dimensionless parameters: the viscosity, the density and the thickness ratio between the two fluids, the Reynolds number, the Froud number and a parameter taking into account the effects of surface tension, the Weber number.

The purpose of this section is to give a brief overview of the metology used to analyze the instability of a two-fluid flow, so the formulation of the stability problem reported here is very general and it is possible to apply it to widely divergent flow systems like, for instance, wind over a the surface of the ocean, liquid-liquid

flow in a channel and thin liquid films.

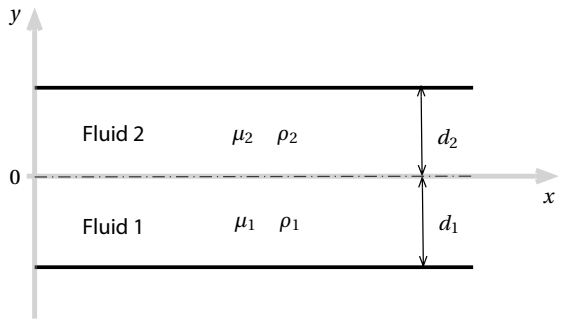

Figure 1.9: Flow configuration and parameters used for the stability study.

The flow of interest is a parallel flow of two immiscible fluids having different densities, ρ_1 and ρ_2, and different viscosities, μ_1 and μ_2, found in two layers of depths d_1 and d_2, as depicted in fig. 1.9. It is possible to obtain a steady solution of the Navier-Stokes equations by solving each layer and matching the stress and the velocity on the interface. Using the fluid 1 as reference, the dimensionless parameters governing the problem are $d = d_2/d_1$, $r = \rho_2/\rho_1$, $m = \mu_2/\mu_1$, the Reynolds number of each layer, $Re_j = \frac{\rho_j U_0 d_j}{\mu_j}$ and the Weber number, $We = \frac{\rho_1 U_0^2 d_1}{\sigma}$. Normally for plane problem it is possible to neglect the effects of buoyancy, thus the Froud number is not introduced.

Following the classical steps of linear stability analysis, the base state (a steady solution of governing equations) is perturbed by adding an infinitesimal disturbance obtained by means of Fourier decomposition along the directions x and z

$$(\mathrm{V}_j, p_j) = (\tilde{\mathrm{V}}_j(y,t), \tilde{p}_j(y,t))\mathrm{e}^{\mathrm{i}(kx+\beta z)} \tag{1.21}$$

where $\mathrm{V} = (u, v, w)$, p is the pressure and the subscript $j = 1, 2$ identifies the layer. k and β are two real numbers representing respectively the wavenumber along x direction and the wavenumber along z direction. We are considering three-dimensional perturbations for which it is possible to define the wavenumber vector, k, whose components are k and β, $\mathrm{k}^2 = k^2 + \beta^2$. Imposing this disturbance to the the base flow it is possible to linearize the governing equations, the boundary and the jump conditions, neglecting

all the quadratic perturbation terms. These linear equations governing the behavior of the perturbations can be written in terms of normal velocity $\tilde{v}_j$ and normal vorticity $\tilde{\eta}_j = \mathrm{i}\beta\tilde{u}_j - \mathrm{i}k\tilde{w}_j$

$$\begin{aligned}\frac{\partial}{\partial t}(D^2-\mathrm{k}^2)\tilde{v}_j + \mathrm{i}kU_j(D^2-\mathrm{k}^2)\tilde{v}_j - \mathrm{i}kD^2U_j - \frac{1}{Re_j}(D^2-\mathrm{k}^2)^2\tilde{v}_j = 0\\ \frac{\partial}{\partial t}\tilde{\eta}_j + \mathrm{i}kU_j\tilde{\eta} + \mathrm{i}\beta DU_j\tilde{v}_j - \frac{1}{Re_j}(D^2-\mathrm{k}^2)\tilde{\eta}_j = 0\end{aligned} \tag{1.22}$$

where $D = \frac{\mathrm{d}}{\mathrm{d}y}$. These equations represent the well-know *Orr-Sommerfeld* and *Squire* equations. The scalar displacement $\tilde{\delta}$ of the interface can be defined by the kinematic condition

$$\frac{\mathrm{D}\tilde{\delta}}{\mathrm{D}t} = (\frac{\partial}{\partial t} + \mathrm{i}kU_j)\tilde{\delta} = \tilde{v}_j \tag{1.23}$$

On the interface, $y = 0$, the normal velocity $\tilde{v}_j$, the streamwise velocity $\tilde{u}_j = \mathrm{ik}^{-2}(kD\tilde{v}_j - \beta\tilde{\eta}_j)$ and the spanwise velocity $\tilde{w}_j = \mathrm{ik}^{-2}(\beta D\tilde{v}_j - k\tilde{\eta}_j)$ must satisfy respectively the following matching conditions

$$\begin{aligned}\tilde{v}_2 &= \tilde{v}_1,\\ (D\tilde{v}_2 - D\tilde{v}_1) - \beta(\tilde{\eta}_2 - \tilde{\eta}_1) &= \mathrm{ik}^2(DU_2 - DU_1)\tilde{\delta},\\ \beta(D\tilde{v}_2 - D\tilde{v}_1) &= k(\tilde{\eta}_2 - \tilde{\eta}_1).\end{aligned} \tag{1.24}$$

Similarly the tangential stress components, τ_{xy} and τ_{yz}, must satisfy

$$\begin{aligned}m[k(D^2+\mathrm{k}^2)\tilde{v}_2 - \beta D\tilde{\eta}_2 - \mathrm{ik}^2D^2U_2\tilde{\delta}]\\ = k(D^2+\mathrm{k}^2)\tilde{v}_1 - \beta D\tilde{\eta}_1 - \mathrm{ik}^2D^2U_1\tilde{\delta},\\ m[\beta(D^2+\mathrm{k}^2)\tilde{v}_2 - kD\tilde{\eta}_2] = \beta(D^2+\mathrm{k}^2)\tilde{v}_1 - kD\tilde{\eta}_1,\end{aligned} \tag{1.25}$$

while the normal stress τ_{yy} condition is

$$\begin{aligned}r(\frac{\partial}{\partial t}D\tilde{v}_2 + kDU_2\tilde{v}_2) - (\frac{\partial}{\partial t}D\tilde{v}_1 + kDU_1\tilde{v}_1) +\\ \frac{m(D^3\tilde{v}_2 - 3\mathrm{k}^3D\tilde{v}_2)}{\mathrm{i}Re_1} - \frac{(D^3\tilde{v}_1 - 3\mathrm{k}^3D\tilde{v}_1)}{\mathrm{i}Re_1} = -\frac{\mathrm{k}^4}{\mathrm{i}We}\tilde{\delta}.\end{aligned} \tag{1.26}$$

The system 1.22 - 1.26, with the suitable boundary conditions, can be considered in operator form

$$\frac{\partial}{\partial t}\mathbf{M}\mathrm{q} = \mathbf{A}\mathrm{q} \tag{1.27}$$

where $\mathbf{M}$ and $\mathbf{A}$ are, respectively, the unsteady and the convective-diffusive operator. It is possible to define a new matrix operator $\mathscr{L}$, the operator of the linearized problem, as $\mathscr{L} = \mathbf{M}^{-1}\mathbf{A}$. In this way the operator form of the previous problem becomes

$$\frac{\partial \mathrm{q}}{\partial t} = \mathscr{L}\mathrm{q} \tag{1.28}$$

This is an abstract Cauchy problem with solution

$$\mathrm{q}(t) = \mathrm{q}(0)\mathrm{e}^{t\mathscr{L}} \tag{1.29}$$

where $\mathrm{q}(0)$ is an initial disturbance propagated forward in time by the exponential operator $\mathrm{e}^{t\mathscr{L}}$.

Modal analysis

Introducing $\mathrm{q} = \tilde{\mathrm{q}}\mathrm{e}^{-\mathrm{i}\omega t}$, where $\tilde{\mathrm{q}} = (\tilde{v}_1, \tilde{\eta}_1, \tilde{v}_2, \tilde{\eta}_2, \tilde{\delta})$, the 1.28 can be written as a generalized eigenvalue problem

$$-\mathrm{i}\omega\tilde{\mathrm{q}} = \mathscr{L}\tilde{\mathrm{q}} \tag{1.30}$$

where ω is a complex number representing the eigenvalue of the linearized problem.

Modal instability is identified with the presence in the spectrum of $\mathscr{L}$ of at least one eigenvalue in the upper half complex plane, $\omega_i > 0$. The spectrum thus determines the behavior of the disturbances, and therefore the stability of the system, at large times.

As shown by Squire (1933), it is possible to restrict the modal analysis to the behavior of only two-dimensional disturbances, since the most unstable disturbances are the ones in the streamwise direction, thus $\beta = 0$ and $\mathrm{k} = k$.

Nonmodal analysis

For most shear flows the spectrum is a poor proxy for the disturbance behavior as it only describes the asymptotic ($t \to \infty$) fate of the perturbation and fails to capture short-term characteristics ([20]). This is due to the non-normality of the linearized operator $\mathscr{L}$ that have a set of nonorthogonal eigenfunction, $\tilde{\mathrm{q}}$. Systems

governed by non-normal matrices can exhibit a large transient amplification of energy contained in the initial condition.

In recent years, indeed, the focus of flow stability study has shifted to also consider the transient growth of disturbances and it has been shown that, like for single-fluid shear flows, also for two-fluid flows, even though the leading eigenmode is stable, it is possible for the energy of certain mode combinations to grow transiently before decaying to zero (see [2] and [1]) and, moreover, the disturbances that reach the highest level of energy amplification are three-dimensional.

To capture the transient behavior of infinitesimal disturbances we have to solve the initial value problem 1.28 and to fix an appropriate measure of the disturbance size. A natural measure is provided by energy that allow to define an energy norm:

$$\begin{aligned}\|\tilde{\mathrm{q}}\|_{\mathrm{E}}^2 = \frac{1}{2\mathrm{k}^2}\int_{-1}^{0}(|D\tilde{v}_1|^2+\mathrm{k}^2|\tilde{v}_1|^2+|\tilde{\eta}_1|^2)\mathrm{d}y+ \\ \frac{r}{2\mathrm{k}^2}\int_{0}^{d}(|D\tilde{v}_2|^2+\mathrm{k}^2|\tilde{v}_2|^2+|\tilde{\eta}_2|^2)\mathrm{d}y+\frac{\mathrm{k}^2|\tilde{\delta}|^2}{We}\end{aligned} \tag{1.31}$$

where the two integrals represent the kinetic energy of the disturbance in the two layer and last term characterizes the contribution of interfacial capillary energy. Following the approach of Schmid and Henningson [20], we use this norm to measure the transient growth of an initial disturbance, $G(t)$, defined as

$$G(t) = \|\mathrm{e}^{t\mathscr{L}}\|_{\mathrm{E}}^2 = \max_{\tilde{\mathrm{q}}(0)\neq 0}\frac{\|\tilde{\mathrm{q}}(t)\|_{\mathrm{E}}^2}{\|\tilde{\mathrm{q}}(0)\|_{\mathrm{E}}^2} \tag{1.32}$$

In computing transient growth, an arbitrary disturbance is expressed as an expansion in the eigenfunctions of $\mathscr{L}$, $\tilde{\mathrm{q}} = \sum_{n=1}^{K}\mathscr{K}_n\tilde{\mathrm{q}}_n$. $G(t)$ is then computed approximately not in the full space of $\mathscr{L}$ but in the subspace defined by the K least-stable eigenfunctions. The value of K is selected large enough to achieve convergence of the approximated $G(t)$. It has been noted, see [2], that when in a two-fluid flow the interfacial energy term is not present ($We \to \infty$ or the surface tension vanishes) the computation of $G(t)$ in the reduced subspace of the K least-stable eigenfunctions does not converge to a limit as K is increased. The reason is that the displacement of the interface $\tilde{\delta}$ is an essential

part of the disturbance eigenfunction and must be included in the energy norm. Thus, in these cases, the solution found by South and Hooper [2] and Malik and Hooper [21] is to introduce in the norm a term of the form $|\tilde{\delta}|^2$ but with a constant coefficient that should be much smaller than unity to work well.

It is important to highlight that the curve given by $G(t)$ represents the maximum possible energy amplification, which for each instant of time is optimized over all possible initial conditions with unit energy norm. The initial condition that optimizes the amplification factor might be different for different times, so $G(t)$ curve should be thought as the envelope of the energy evolution of individual initial conditions with unit energy norm. However it is not difficult to determine the initial condition that will reach the maximum possible amplification at a given time t_0 and that will be tangent to $G(t)$ at t_0 by means of the Singular Value Decomposition (SVD) of the matrix exponential $G(t) = \|e^{t\mathscr{L}}\|_E^2$, as described in [20].

Another useful tool to analyze the behavior of non-normal operators is the ϵ-pseudospectrum introduced by Trefethen [22]. A complex number z lies in the ϵ-pseudospectrum of the operator $\mathscr{L}$, denoted by $\Lambda_\epsilon(\mathscr{L})$, if either of the following equivalent condition is satisfied:

1. z is an eigenvalue of $\widetilde{\mathscr{L}} = \mathscr{L} + E$, for some perturbation matrix E with $\|E\| \leq \epsilon$;

2. z is a complex number and $\left\|(zI - \Lambda)^{-1}\right\| \leq \epsilon^{-1}$

The most basic role of plots of pseudospectra is to define the situation in which eigenvalues are likely to be of limited physical significance.

Description of pseudospectral code

The generalized eigenvalue problem 1.30 has been discretized separately for each fluid by means of a Chebyshev pseudospectral code written in MATLAB programming language. For both fluids, the finite domain is mapped to the standard interval $[-1, 1]$ via a linear transformation. The *DMSuite* package of [23] has been used in order to obtain the discretized differential operators.

Boundary conditions are enforced by the technique of replacing rows and interface conditions are treated as boundary conditions for each phase.

A procedure to eliminate the spurious eigenvalues has been implemented in the code. As reported by Boyd [24] it is possible to distinguish between two different types of spurious eigenvalue: the *physically spurious* eigenvalues (numerically-computed eigenvalues which are in error because of misapplication of boundary conditions or some other misrepresentation of the physics) and the *numerically spurious* eigenvalues (approximations to exact eigenvalues because the mode is oscillating too rapidly to be resolved by N degrees of freedom). A given numerically spurious eigenvalue can always be computed accurately by using sufficiently large number of degrees of freedom N.

In the used code each calculation is repeated twice with different number of collocation points N to verify that the solution is well-resolved. To know how many modes are "good" the lists of eigenvalues for two different N are compared and only those which are the same (within some user-set tolerance) on both lists are accepted. For separating "good" eigenvalues from trash we use a simple numerical method which yields to a plot on a logarithmic scale of the reciprocal of the difference between corresponding eigenvalues as calculated at different resolutions N, scaled by some measure of the size of the eigenvalues. The reciprocal of the difference is plotted so that the "good" eigenvalues are at the top of the graph. The obvious scaling for the j-th eigenvalue is $|\lambda_j|$ itself, anyway, since an eigenvalue may accidentally be very close to zero, it is convenient to use a different scaling defining the *intermodal separation*

$$\begin{aligned} \sigma_1 &\equiv |\lambda_1 - \lambda_2| \\ \sigma_j &\equiv \frac{1}{2}\left(|\lambda_j - \lambda_{j-1}| + |\lambda_{j+1} - \lambda_j|\right), \qquad j > 1 \end{aligned} \tag{1.33}$$

In many problems, the eigenvalue ordering is invariant when the resolution is changed, thus it is sufficient to compare with the set tolerance and to plot the reciprocal of the *ordinal difference*

$$\delta_{j,\text{ordinal}} \equiv |\lambda_j(N_I) - \lambda_j(N_{II})|/\sigma_j \tag{1.34}$$

where N_I and N_{II} denote the collocation points in the low and

high resolution computation. The parameter $1/\delta_j$, as shown in fig. 1.10, is many order of magnitude larger for the good modes that for the bad ones.

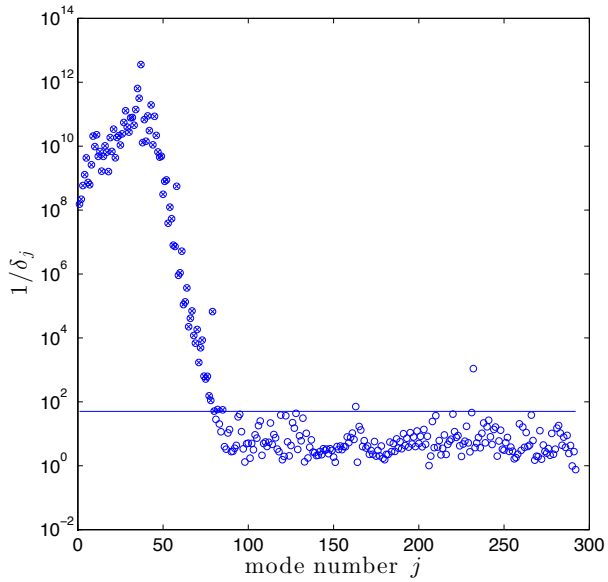

Figure 1.10: The reciprocal ordinal difference $1/\delta_j$ are plotted on a logarithmic scale versus mode number j. The continuous blue line represent the value of the set tolerance (in this case, referred to a typical configuration of Core-Annular Flow, see chapter 3, the value of the tolerance is 50). The eigenvalue are ordered by imaginary part being $j = 1$ the bigger. $N_I = 150$ and $N_{II} = 170$.

The spectral discretization of the spatial operator has been used also to compute the transient growth function $G(t)$. The *Matrix Exponential* technique of [20] has been employed by adapting their schemes to the two-fluid flow case. The matrix exponential of eq. 1.32 is approximated using the first K least-stable eigenmodes sufficient to assure the convergence. The energy norm is calculated by transforming it into a standard 2-norm by employing an SVD decomposition of the matrix of inner products between the eigenvectors (see [20]).

The so called *optimal perturbation*, the initial condition tangent to the maximum of the curve $G(t)$ at $t = t_{G_{\text{MAX}}}$, has been calculated via the SVD of the transformed matrix exponential, modifying the classical procedure reported in [20] for the two-fluid case.

Standard algorithm to compute the ϵ-pseudospectrum, adapted

from routine of Trefethen [25], is implemented in the code.

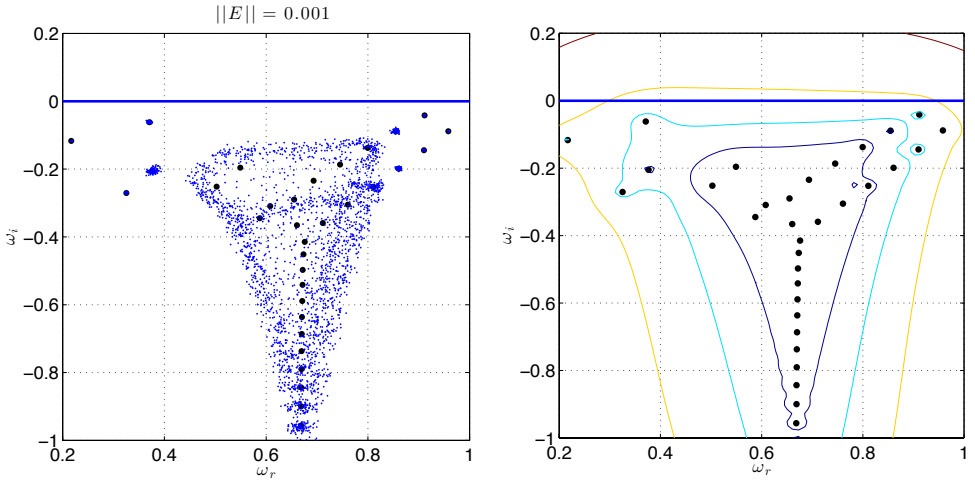

Figure 1.11: The described pseudpsectral code has been used to compute the ϵ-pseudospectrum of a typical configuration of Hagen-Poiseuille flow (see fig. 3 in [8]). Two representations of the ϵ-pseudospectrum are reported: on the left superposition of a perturbed matrix of energy norm 10^{-3} to the spectrum of the linearized operator; on the right the boundaries of the ϵ-pseudospectrum (from outside in, the curves correspond to $\epsilon = 10^{-1}, 10^{-2}, 10^{-3}, 10^{-4}$).

1.4 Direct Numerical Simulation

Numerical simulations may improve our understanding of two-fluid flow dynamics, above all the origins of the instabilities ruled especially by nonlinear effects, of course not explained by linear theory. Moreover, it has been noticed that agreement between linear theory and numerical simulation is particularly difficult to obtain because of the complex effect of viscosity on the base profile and on the instability growth rates and modes.

The simulation of Navier-Stokes equation with interfaces, on one hand uses numerical methods analogous to otherwise well-known methods in the bulk of the phases, such as finite volumes, finite elements and finite differences; on the other hand, presents specific problems due to the presence of the interface: location of the discontinuity and computation of surface stresses. Most of two-fluid flow problems exhibit all or several of the following characteristics: high surface tension, low viscosity, high density ratio, complex and evolving interface topologies and spatial scales ranging over several orders of magnitude. In this context, an

ideal numerical method for the solution of two-fluid Navier-Stokes equations with surface tension should have the following properties:

- robust representation of evolving, complex interfaces;
- accurate representation of surface tension;
- robust and accurate handling of large density and viscosity ratio;
- efficient representation of the flow features on the different characteristics spatial scales.

"One-fluid" formulation

In contrast to the approach described in section 1.3, where the governing equations are written separately for each phase and jump conditions are used to couple the solutions at the fluid interface, it is possible to write one set of governing equations for the whole flow domain occupied by the various phases, without resorting to jump conditions. The various phases are treated as one fluid with variable material properties that change abruptly at the phases boundary. To account for the effects of surface tension at the interface it is necessary to add a singular term to the Navier-Stokes equation. This term is the counterpart of the jump condition for the normal stress, first of eqs. 1.19.

This form of equations is often referred to as the "one-fluid" approach. Since the solution can change discontinuously across the interface, we have to admit solution of governing equations that include generalized functions, such as delta functions or step functions. This formulation is the starter point for several numerical methods.

The formulation of the equations is the same of section 1.1 except that we need to add the surface tension as a body force to the momentum equation. For a control volume including an interface, the surface tension force f_σ is given by integrating over S, the part of the surface enclosed in the control volume. It is possible to convert the surface integral to a volume integral

$$\int_S \mathrm{f}_\sigma \mathrm{d}S = \int_V \mathrm{f}_\sigma \delta_S \mathrm{d}V \tag{1.35}$$

where $\delta_S = \delta_S(\mathrm{x} - \mathrm{x}_S)$. Adding this force to the integral form of the momentum equation we obtain the one-fluid version of the Navier-Stokes equation for incompressible Newtonian flows with sharp interfaces:

$$\rho \frac{\mathrm{D}\mathrm{V}}{\mathrm{D}t} = -\nabla p + \rho g + \nabla \cdot \mu(\nabla \mathrm{V} + \nabla \mathrm{V}^T) + \mathrm{f}_\sigma \delta_S \qquad (1.36)$$

For constant surface tension, the surface force is $\mathrm{f}_\sigma \delta_S = \sigma c \mathrm{n} \delta_S$.

Using one set of equations for the whole flow field, the different fluids must be identified in some way. This is generally done by means of a marker function that takes different values in the different fluids. As the fluids move, and the boundary between them changes location, the marker function must be updated. Updating marker function accurately is critical for the success of the simulations of multiphase flows and is surprisingly difficult. Various methods have been developed to overcome these difficulties and it is possible to divide them into two groups: methods that advect directly the marker function ("front-capturing" methods) and methods that track the boundary between different fluids using marker points and then the marker function is reconstructed from the location of the interface ("front-tracking method"). In addition to the possible ways to update the marker function, surface tension can be included in disparate modes.

Volume Of Fluid method

The Volume Of Fluid (VOF) method is the oldest method (see [26]) to advect a marker function and, after many improvements and innovations, continues to be widely used. Historically it was adopted for free surface flows with only one fluid, now it is routinely used for two-fluid flows. In the VOF method the marker function used is the characteristic discrete function H (see formula 1.5). The direct advection of this function is based on a simple state: as the interface moves, the shape of the region occupied by each fluid changes, but each fluid particle retains its identity. Thus the material derivate (following the motion of a fluid particle) of H is zero

$$\frac{\mathrm{D}H}{\mathrm{D}t} = \frac{\partial H}{\partial y} + \mathrm{V} \cdot \nabla H = 0 \qquad (1.37)$$

Following the flow computationally, we have to work with an approximation of H. Several approximations are possible: in VOF method the color function C (or volume fraction) is used. This function represents the fraction of a computational grid cell which is occupied by the fluid assumed to be the reference one. Considering a Cartesian grid with square cells of side $h = \Delta x = \Delta y$

$$C_{i,j} = \frac{1}{h^2} \int_V H(x, y) \mathrm{d}x \mathrm{d}y \tag{1.38}$$

The function C varies between the constant value of one in full cells to zero in empty cells, while mixed cells with an intermediate value of C define the transition region where the interface is localized ($0 < C < 1$).

The use and the effectiveness of VOF methods are widespread for several reasons:

- they preserve mass in a natural way, as a direct consequence of the advection algorithm based on a discrete representation of the conservation law (eq. 1.37);
- the change of topology of the interface (reconnection or breakup) are implicit in the algorithm;
- they can be relatively simply extended from two-dimensional to three-dimensional domains;
- since only the values of C of the neighboring cells are needed to update C value in the cell (i, j), it is relatively simple to implement these algorithms in parallel.

In general, the VOF algorithm solves the problem of updating the volume fraction field C given the fixed grid, the velocity field and the field of C at the previous step. In low-order VOF methods, the interface line in each mixed cell, in the two dimensions case, is represented by a segment parallel to one of the two coordinate axes. The interface is clearly not continuous across the cell boundary, and the jump is usually of order h, $\mathcal{O}(h)$. High-order methods reconstruct the interface in various ways. The standard one is the PLIC (Piecewise Linear Interface Calculation) reconstruction (see [27]), where the interface in each mixed cell is represented by a

segment perpendicular to the local gradient of C, $\mathrm{m} = -\nabla C$. However, there is still no requirement to the continuity of the interface at the cell boundary, but now the discontinuity is usually smaller and it is function of the grid spacing and of the local curvature, c, thus whenever the curvature is small (i.e. the curvature radius is large with respect to the grid size) the method will be accurate. However PLIC is a quite robust: it does not have catastrophic behavior when the curvature increases.

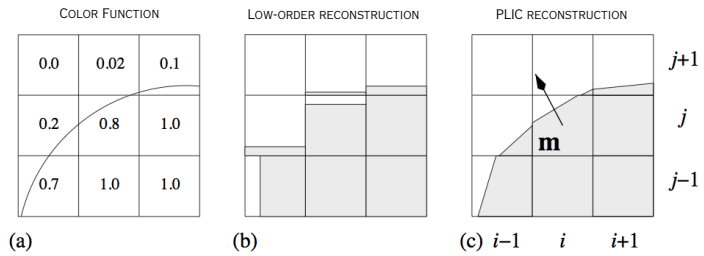

Figure 1.12: (a) a portion of the interface line and the value of color function in each cell; (b) a low-order reconstruction of the interface; (c) PLIC reconstruction of the interface with unconnected segments in each cell.

Thus, a VOF/PLIC algorithm proceeds in two steps:

1. reconstruction of the interface shape from the knowledge of volume fraction in each cell;

2. advection of the reconstructed interface in a given velocity field.

For PLIC method the reconstruction is basically a two-step procedure. In any given cell the normal m is first determined from knowledge of the color function in this cell and in the neighboring ones. Several algorithms have been developed for the calculation of the normal vector: they can be based on a finite-difference approximation of the volume fraction gradient ∇C (see [28]) or satisfy some other minimizing criteria (see [29]). Most of these algorithms uses a 3×3 block of cells (remember that we are considering the two-dimensional case) to determine the approximate interface in the central cell of the block, in fig. 1.12-(c) this central cell in denoted by the two indices (i, j).

In the second part of the reconstruction, a linear interface, that divides the cell into two parts containing the proper area of each

fluid, must be found. In two dimensions, given a square cell of side h and a straight line (HE of fig. 1.13) with normal vector m, we have to find the area of the region below this line and that also lies within the square cell: we have to find the area of the polygon $ABFGD$ of fig. 1.13. The most general equation for a straight line in the (x, y) plane with normal m is

$$\mathrm{m} \cdot \mathrm{x} = m_x x + m_y y = \alpha \tag{1.39}$$

where α is a parameter to be adjusted until the difference between the area of the gray region in fig. 1.13 and the value of $\Delta x \Delta y C(i, j)$ is below a prescribed tolerance.

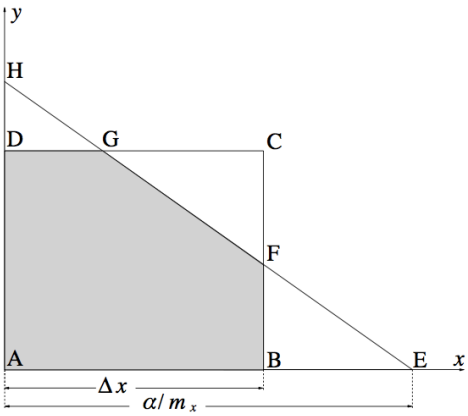

Figure 1.13: Geometrical basis for the expression 1.39.

The second step of VOF algorithm is propagation of the interface. Once the interface has been reconstructed, its motion by the underlying flow field must be modeled by a suitable advection algorithm. The most used is the fractional step (or operator split) method, which updates the volume fraction C by advecting the interface along one spatial direction at a time. Intermediate C values are calculated during this process and the final C field is obtained only after advection of the interface along all the coordinate directions. In these calculations it is used a Lagrangian approach, i. e. the motion of the interface segments is computed directly (see [30]). Because in practice the time-stepping is performed separately in each spatial direction, it is possible to only described the advection of the interface just along x-direction.

For each cell, three contributions are calculated: the area fluxes

ϕ^- and ϕ^+ entering the cell (i, j), respectively, from the cells $(i-1, j)$ and $(i+1, j)$ and the area ϕ^0 of the fluid contained at the beginning of the step in control cell. The updated volume fraction in each cell after the fraction step along the x-direction is then given by

$$C^x_{i,j} = [\phi^-_{i,j} + \phi^0_{i,j} + \phi^+_{i,j}] \tag{1.40}$$

The Lagrangian advection method allows to take into account the stretching or compression of the interface during each single fractional step. The procedure can be made second-order accurate by alternating the advection directions at each time.

One of the most critical aspect of the VOF methods is the accurate computation of the surface tension. The surface tension term in the Navier-Stokes equation creates a most obvious difficulty since it is a singular term. In several implementations of the method, this difficulty is manifested in both numerical instabilities and in poor accuracy of capillary effects.

A whole family of methods for surface tension have been developed for the use of the marker function; the standard approaches are the *Continuous Surface Tension* (CSF) and the *Continuous Surface Stress* (CSS).

The surface tension is added as a body force to the discrete version of the Navier-Stokes equation in the form $\mathrm{f}_\sigma = \sigma c \mathrm{n} \delta_S$. In the CSF method (see [31]) the δ_S distribution is approximated by $|\nabla C|$. This approximation seems to be natural since the marker function C approximates the Heaviside function H. Thus, to the interface cells is added the following force $\mathrm{f}_{i,j}$

$$\mathrm{f}_{i,j} = \sigma c |\nabla C| \mathrm{n} \tag{1.41}$$

Sometimes it is necessary to smooth this approximation of δ_S using a filter for the color function. Anyway, the unsmoothed version allows a remarkable exact balance between pressure and surface tension, $-\nabla p + \mathrm{f}_\sigma \delta_S = 0$.

Very important in this algorithm is to find an approximation of the curvature c. There are many suggestions, but a particularly simple one consists into using the curvature-divergence relation $\nabla \cdot \mathrm{n} = -c$. Thus, the force to add to the cells where the interface is localized is

$$\mathrm{f}_{i,j} = \sigma (\nabla \cdot \mathrm{n}) |\nabla C| \mathrm{n} \tag{1.42}$$

where the approximation of the unit normal vector is $\mathrm{n} = \frac{\nabla C}{|\nabla C|}$.

In the CSS, instead of discretizing the force representation of the surface tension, one may start from eq. 1.11

$$\mathrm{f}_\sigma \delta_S = \nabla \cdot \mathbf{T}_S^\sigma \delta_S = \nabla \cdot [\sigma(\mathbf{I} - \mathrm{nn})\delta_S] \tag{1.43}$$

The discretization of eq. 1.43 without any smoothing is

$$\mathrm{f}_{i,j} = \nabla \cdot (\mathbf{T}_S^\sigma |\nabla C|) = \nabla \cdot [\sigma(\mathbf{I} - \mathrm{nn})|\nabla C|] \tag{1.44}$$

These two methods give unsatisfactory results, to improve them it is convenient to smooth the color function taking into account other neighbor cells (the use of a filtered surface tension is connected with the idea of an interface with a finite thickness). One of the most common filter is the "five-point smoothing":

$$\widetilde{C}_{i,j} = \frac{1}{2} C_{i,j} + \frac{1}{8}(C_{i,j-1} + C_{i,j+1} + C_{i-1,j} + C_{i+1,j}) \tag{1.45}$$

1.5 SURFER vs. GERRIS code

Two different numerical codes have been used to perform the numerical simulation reported in this thesis: an "ad-hoc" version of SURFER and GERRIS, a new generation VOF code. Both are open-source flow solvers.

SURFER is a fixed-grid numerical code developed in the 90s by Lafaurie et al. [3] for the simulation of two and three-dimensional flows with several fluid phases and free interfaces between them. It is based on the VOF/PLIC method and its two essential features are the ability to capture the interface and a computationally efficient algorithm for surface tension. The initial idea for SURFER, and in particular for the 2D version of the code, was developed by Zaleski.

The governing equations are solved trough a projection method using staggered finite difference on a MAC grid and a split-explicit first-order accurate time differencing scheme. The velocity is first updated with the viscous and capillary tensors, then with the advection term. In this way it is computed a provisional velocity field V^* that have to be projected on a divergence free field (in this way incompressibility is enforced). The velocity

field at time step t_{n+1}

$$V^{n+1} = V^* - \frac{\tau}{\rho}\nabla p \tag{1.46}$$

where $\tau = t_{n+1} - t_n$ is the time step and p is the solution of Poisson problem with homogeneous Neumann boundary conditions

$$\nabla \cdot (\frac{1}{\rho}\nabla p) = \frac{1}{\tau}\nabla \cdot V^* \tag{1.47}$$

Thus the velocity field V^{n+1} has to verify the incompressibility equation

$$\nabla \cdot V^{n+1} = 0 \tag{1.48}$$

Using an explicit-in-time, centered-in-space finite-difference scheme introduces classical limitations on the time step and on the mesh Reynolds number, see [32].

The estimation of density and viscosity is made trough a simple volume average over the cell

$$\begin{aligned} \rho &= \rho_1 C + \rho_2 (1 - C) \\ \mu &= \mu_1 C + \mu_2 (1 - C) \end{aligned} \tag{1.49}$$

In this way both the viscous term in Navier-Stokes equation and the Poisson problem depend implicitly on the color function. In particular the first term of eq. 1.47 may be singular for two different reason, first because the pressure p jumps across the interface, and second because also ρ jumps. For these reason, although a sharp interface is more accurate and somewhat prevents the diffusion of density and momentum, sometimes gets a slower convergences of the SOR algorithm (that we have implemented in the "in-house" modified SURFER to solve the Poisson problem, in spite of its slow convergence, because of its extreme simplicity) and does not allow to obtain a second-order spatial accuracy for the solution of pressure field.

In the used version of SURFER the surface tension is computed trough the CSF algorithm.

This code is stable in an appreciable range of parameters, although it appears difficult to treat large density ratios and large surface tensions simultaneously. Especially linked to the surface tension algorithm, all long a weak point of method using an implicit representing of the interface, is the presence of "parasite"

or "spurious "currents. These currents are vortices appearing in numerical simulations in the neighborhood of the interfaces despite the absence of any external forcing. It is difficult to give a systematic expression for the amplitude of spurious currents because they often fluctuate in time, but direct measurements have shown that it depends on parameters such as the viscosity, the density and the time step. At worst these parasitic currents can be strong enough to dominate the solution. A not perfect equilibrium between the pressure jump across the interface and the surface tension force (Laplace's law 1.10) is also due to the presence of these currents.

GERRIS Flow Solver is successful to overcome the problem of spurious flows and allows to have more accurate simulation reducing the computational time. This code, developed by Popinet (see [33] and [4]), presents the current advances in the numerical simulations of two-fluid flows combining two classical methods, namely the VOF method and the Adaptive Mesh Refinement (AMR) method, that lead to an optimization of numerical calculations.

Dynamic mesh-adaptive methods can deal efficiently with the phenomena involving a wide range of spatial scales, typical of two-fluid flows. Simulations with AMR are extremely efficient both in term of resolution and in term of CPU time, because we have fewer cells and smaller CPU time than an uniform mesh with the highest resolution. The AMR implemented in GERRIS is based on a discretization using square (cube in in three dimensions) finite volumes organized hierarchically as quadtree (octree in three dimensions). In this organization each cell may be the *parent* of up to four *children* (eight in 3D). The *root cell* is the base of the tree and a *leaf cell* is a cell without any child. One of the advantage of this spatial discretization is that mesh refinement, or coarsening, can be performed at every time-step if necessary by means of different several refinement criteria that can be used simultaneously. For example, the criteria that have been used in our simulation are based on the vorticity $\nabla \times V$ and on the gradient of the color function ∇C: in this way a finer resolution has been ensured in areas of high vorticity and around the interface.

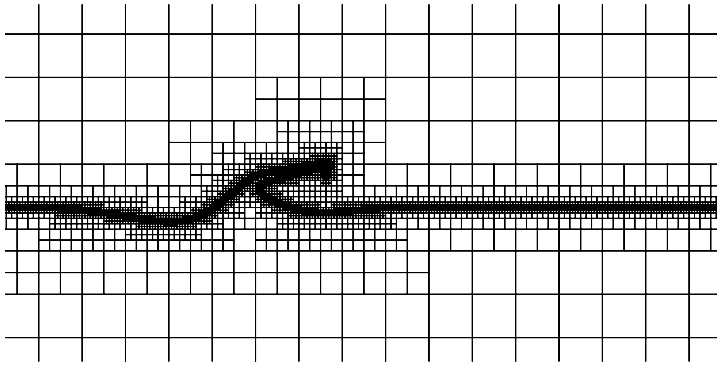

Figure 1.14: Example of AMR of the simulation domain. The case reported is discussed in chapter 2, section 2.1.

All the variables are collocated at the center of each cell (a collocated grid makes momentum conservation simpler when dealing with mesh adaptation) and a staggered second-order accurate time discretization is considered.

In SURFER, such as in almost all the previous VOF based code, obtaining accurate values for useful geometrical properties, i. e. interface normal direction and curvature, has traditionally been the Achille's heel. Besides the original curvature estimation of [31], already discussed at the beginning of this section, several methods have been proposed for estimating curvature from volume fraction field. The "Heigh-Function" (HF) scheme, developed by François et al. [34], is simpler to implement than other high-order methods, but it is limited when the interface is bad-resolved and the curvature becomes comparable to mesh-size. In GERRIS we find a new generalized to quad/octree discretization HF method which assures consistent second-order convergence even for low resolutions, [4].

Although computing accurate curvature is an essential step to obtain an accurate surface tension formulation, it is not sufficient. For this reason in GERRIS is implemented a method that stresses the importance of the concept of "balance-force" continuum formulation [35] to be coupled with the generalized HF. This method uses the standard CSF and is characterized by a pressure correction algorithm that leads to an exact balance between ∇p and surface tension force.

Another classical difficulty of methods with an implicit rep-

resentation of the interfaces is to handle large density ratios. It is tempting, and often necessary, to smooth the jumps in physical properties, but, in this way, the resulting numerical approach can lead to physical inconsistent results. A related problem for large density ratio is that the Poisson equation 1.47 becomes stiffer. GERRIS uses the multigrid Poisson solver presented by Popinet [33] for single-fluid flows that fits nicely with the quad/octree discretization and works well also for two-fluid flows, [4]. Its performance, in terms of convergence speed, depends on the consistency of the representation of the domain topology (i.e. interface) on successively coarser grids.

All the presented advances in numerical simulation are allowing to go deep into the understanding of the physical processes underlying multifluid flows. The accurate schemes described, indeed, have made possible to perform simulation even in critical regimes of two-fluid systems, for example the ones found in the atomization process, and, the adaptive mesh has shown to provide a gain of about three order of magnitude in simulation size compared to an equivalent regular-Cartesian-grid simulation.

2

Two-fluid flows in plane geometry

The incompressible flow made by two horizontal parallel infinite streams of different velocities, densities and viscosity represents a classical stability problem. We find many realizations of such flow in geophysics: thermally stratified layers in oceans, for instance, or in the atmosphere. This is also the case at the surface of the sea: the wind blowing destabilizes the surface of the sea generating waves that may propagate and grow. This mechanism is a shear-layer instability and was initially studied by Helmholtz [36] who described it as the evolution of a localized irregularity on a thin shear layer. Few years later, Kelvin [37] gave a description of this instability using the powerful mathematical framework of low-amplitude sinusoidal perturbations. Therefore this shear instability is generally referred to as *Kelvin-Helmholtz instability* (KH).

Two-phases flows of immiscible fluids are found also in industrial applications. For example, the case of parallel flowing layers is one prototypical and important configuration for the atomization of fuels in thermal engines. In the atomization process the flow is unstable due to the exponential growth of small perturbations to the base flow. This primary shear instability, a typical KH mechanism, produces waves formation at the gas-liquid interface and represents the first of several processes on increasingly smaller length scales which leads to the eventual production of droplets.

Linear stability theory is the first method used to examine this phenomenon, but to understand the effects of the nonlinear

disturbances amplitude growth and to study their subsequent breakup into drops, numerical simulations are indispensable. These are the two tools that will be used in this chapter to analyze some examples of gas-liquid flows.

2.1 The evolution of a localized nonlinear Kelvin-Helmholtz wave with gravity

In this section it is highlighted how the approaches of Helmholtz and Kelvin are critically opposed: the one considers the nonlinear evolution of a localized perturbation, and the other considers the linear evolution of a periodic wave. This critical opposition was the central topic of a recent article [38]. In this paper, numerical simulations of a shear layer was performed and the differences between a weak sinusoidal initial condition (Kelvin) and a strong localized initial condition (Helmholtz) were studied. In the case of a localized initial condition of amplitude sufficient to create immediately a nonlinear wave, a self similar growth of the wave can be observed. The localized and nonlinear wave grows algebraically in time without changing its shape. This self-similar growth can be understood from the fact that the Euler equations have no intrinsic length scale, thus the only length scale is inertial $L = Ut$, with U the velocity jump across the shear layer and t the time. The wave grows self-similarly according to the growth of this inertial length-scale. In the case of a sinusoidal initial condition, on the other hand, like the classical case of Kelvin's analysis, the self-similar growth cannot be observed since the periodic initial condition pollutes the dynamics with the scale of its wavelength: the dynamical structures appearing during the natural evolution of the instability (rolled-up vortices, also known as *Kelvin-Helmholtz billows*) are locked at this externally imposed wavelength.

The aim of this section is to pursue the analysis of the self-similar solution observed in [38] with direct numerical simulations. The self-similar solution is possible only when there is no intrinsic length scale in the problem, so, if we chose to consider the effect of viscosity and surface tension, we would add a viscous length scale and a capillary length scale. We can consider these

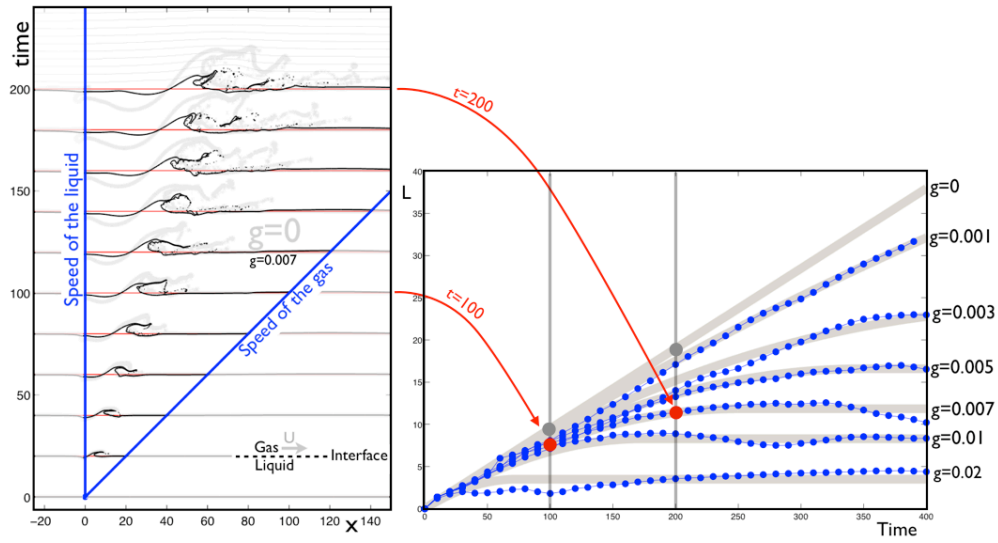

Figure 2.1: a) Evolution in time of the wave interface for a gas (fluid over the shear layer) ten times lighter than the liquid (the fluid below the shear layer) for a weightless wave $g = 0$ (light gray interface) and for $g = 0.007$ (black interface). b) Evolution in time of the size of the wave while varying the intensity of the gravity. (From [9].)

scales as *small length scales*. Nevertheless, when the instability is initiated locally, the wave may grow quickly beyond these two small length scales toward its self similar regime: the bigger the wave, the lesser the impact of viscosity and capillarity; these two effects will play their role during the initial transient from the initial condition. In the case of a shear layer between two fluids of different densities and in the presence of gravity, there is yet another length scale, which is a *large length scale*: the bigger the wave the larger the impact of its weight. Basically in this section the study of the self-similar wave is extended to the case where gravity is present.

Numerical experiments of a shear layer initially perturbed at a given location with an initial force large enough to create a wave immediately nonlinear are reported. After a short initial transient, the wave tends to its self-similar algebraic growth, but once the wave becomes large, the volume force of its weight starts to play its role against instability and against self-similarity as shown in fig. 2.1.

Model

The wave is considered as an obstacle to the gas stream such that the flow above its head is accelerated. This acceleration induces a pressure drop which is the driving force for the vertical growth of the wave. The intensity of this pressure drop does not depend on the size of the wave: this is the main ingredient for self similarity. Since the wave grows, it will eventually reach a size at which volume forces like gravity become comparable to the aerodynamic surface forces. Once the hydrostatic pressure drop in the liquid body of the wave equals the aerodynamic pressure drop, there is no longer a driving power and the wave has reached its maximum size. Fig. 2.1 displays the archetypal configurations: in gray the evolution of the weightless wave, that grows in size without changing shape; in black the wave with gravity, that reaches a stationary height after an initial transient. These simulations correspond precisely to the case and parameters of [38], except that a vertical acceleration is included to model gravity.

The main parameters are U the velocity difference between the gas and liquid, g the acceleration of gravity, ρ_{gas} and ρ_{liq} the densities of the gas and liquid (respectively above and below the shear layer). Dimensional analysis tells that the wave should reach its maximum size $L_{\text{apex}} \propto U^2/g$ in a time $T_{\text{apex}} \propto U/g$. Once time and space are made nondimensional using these relevant scales, the remaining parameters are the Reynolds and the Weber number (quantifying respectively the effect of viscosity and surface tension), the ratio of the shear layer thickness and wave height δ/L_{apex} and the density ratio $r = \rho_{\text{gas}}/\rho_{\text{liq}}$. Considering the ideal limit in which Reynolds and Weber numbers are large and the mixing layer is thin, the only remaining parameter is the density ratio r.

It is possible to inspect the wave growth using a simple analysis based on the Bernoulli equation. See fig. 2.2 for a sketch of the wave configuration. The aerodynamic pressure drop due to the narrowing of the streamlines above the liquid obstacle is $\Delta p_{\text{gas}} \propto \rho_{\text{gas}} U^2$. In parallel, the pressure drop in the liquid due to the acceleration of the liquid sucked from its bottom at speed v and the gravity is $\Delta p_{\text{liq}} \propto \rho_{\text{liq}}(v^2 + gL)$. Since in the region of the wave

head the pressure is the same in the liquid and in the gas, these two terms are equal yielding the suction velocity at the bottom of the wave

$$v^2 \propto rU^2 - CgL \tag{2.1}$$

with C a geometrical constant. This expression is characteristic of the counteracting effects of inertia and weigh. Now, the law describing the evolution of the wave size can be simply obtained: considering that the wave area grows in time proportionally to the amount of the liquid sucked at speed v from the bottom section of the wave of length L, we get $\dot{L} \propto v$, which yields upon integration

$$\begin{array}{ll} \overbrace{L = a\sqrt{r}Ut}^{\text{Weightless law}} - bgt^2, & t < T_{\text{apex}} \\ L = L_{\text{apex}}, & t \geq T_{\text{apex}}. \end{array} \tag{2.2}$$

The weightless algebraic growth is recognisable for short times, with the constant a, which is counteracted by a gravity term growing like the square of time, until $t = T_{\text{apex}}$ when it forbids any more growth, after this threshold time, our simple analysis predicts that the wave keeps its maximum size L_{apex}

$$L_{\text{apex}} = \alpha r \frac{U^2}{g}, \quad T_{\text{apex}} = \beta\sqrt{r}\frac{U}{g} \tag{2.3}$$

with $\alpha = a^2/4b$, $\beta = a/4b$.

This law of growth and saturation of the wave under the combined action of wind and weight is compared to computed data in fig. 2.1b). We show the evolution in time of the wave size while varying g from 0 (the self similar evolution) up to $g = 0.02$. The equation (2.2) has been drawn superimposed to the numerical data with constant a adjusted on the weightless algebraic law, and b such as to fit best the data for all shown values of g. Indeed all curves start with the same slope as the weightless case, and saturate at a height compatible with the scaling on U^2/g from (2.3).

The integration in (2.3) predicts an evolution of the wave in two sequences, first a growth where the algebraic law of the weightless wave is progressively compensated with a gravity term growing like the square of time, followed by a state with a wave of constant size.

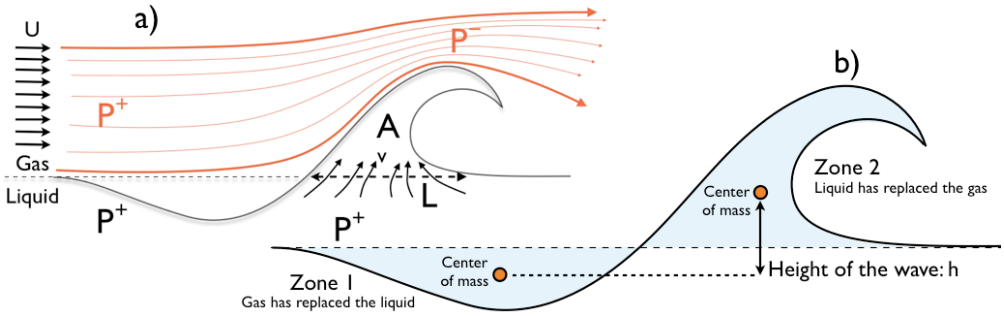

Figure 2.2: Schematic representation of the growing wave. a) Illustration of the streamline and pressure relevant to the dynamic model of the wave (2.1), and b) wave structure used to define the height of the wave from consideration of its gravity potential energy in (2.4). (From [9].)

This quantitative model only describes the global behavior of the liquid structure, we thus need to chose an observable that overlooks the small scale details. Since the wave with gravity is characterized by a strong anisotropy that prevents the wave from growing in vertical direction, to measure the height of the wave we use a devise inspired by considerations of gravity potential energy of the liquid system.

The gravity potential energy of a fluid element at altitude y is $\mathrm{d}E_p = \rho g y \mathrm{d}S$. Thus the variation of total gravity potential energy from initial time to time t is

$$\Delta E_p = g \int_{xy} [\rho(x,y,t) - \rho(x,y,0)] y \mathrm{d}S.$$

The density ρ in this equation can be either that of the liquid or that of the gas. Considering an arbitrary point x, y in space, the contribution of this point to the integral is zero if the fluid has not changed from time 0 to time t. We may thus define two zones which contribute to this variation of energy: zone 1 where gas has replaced the liquid, and zone 2 where liquid has replaced the gas, see fig. 2.2. The change of potential energy is thus

$$\Delta E_p = g \int_1 (\rho_{\mathrm{gas}} - \rho_{\mathrm{liq}}) y \mathrm{d}S + g \int_2 (\rho_{\mathrm{liq}} - \rho_{\mathrm{gas}}) y \mathrm{d}S$$

which we can rewrite

$$\Delta E_p = g(\rho_{\mathrm{liq}} - \rho_{\mathrm{gas}})(\underbrace{\int_2 y \mathrm{d}S}_{Ah_2} - \underbrace{\int_1 y \mathrm{d}S}_{Ah_1}) = g(\rho_{\mathrm{liq}} - \rho_{\mathrm{gas}}) Ah \qquad (2.4)$$

where A is the surface of the zones (the two surfaces are equal due to conservation of volume) and h_1 and h_2 are the altitudes of the center of mass of zone 1 and 2. This last expression shows that $h = h_2 - h_1$ is a measure of the wave height relevant in terms of the potential energy related to gravity. This is the measure that we will use to test our theory for the plateau induced by gravity.

Numerical Experiments

The tool of experimentation is numerical simulations of the Navier-Stokes equations for a system of two interacting fluids. Memory and computation time limitations impose moderate values of the Reynolds, Weber and δ. We have chosen U^2/g and U/g as reference length and time, and to vary the density ratio r while keeping the Reynolds and Weber fixed. Also the value of the initial mixing layer thickness is given in proportion of the predicted maximum wave size.

We use the open source software Gerris Flow Solver [4] to perform numerical simulations. Sizes are made nondimensional using the reference size U^2/g and times with U/g; this is equivalent to taking $U = g = 1$ in our simulations. In preliminary computations it was found that the top of the liquid wave reaches approximately the height $L_{\text{apex}} = 0.7rU^2/g$ in time $T_{\text{apex}} = 5\sqrt{r}U/g$, so we set the parameters in proportion to these references. The box height is $8L_{\text{apex}}$ to avoid confinement from the boundary conditions, while retaining the resolution of the wave when it reaches its plateau. The box is four time longer than high. The initial shear layer thickness δ is set to $L_{\text{apex}}/20$. The viscous law of diffusion of the *error function* velocity profile is $\text{erf}(y/2\nu(t - t_0))$ with ν the kinematic viscosity of each fluid. The viscosity is set in each fluid such that the mixing layer thickness is multiplied by 3 by viscous growth at time T_{apex}

$$\nu = 4\delta^2/T_{\text{apex}}$$

This choice of viscosity gives a Reynolds based on δ and proportional to $1\sqrt{r}$, thus ≈ 110 for $r = 0.1$ and ≈ 360 for $r = 0.01$. The Reynolds based on L_{apex} is twenty times these values: 2200 and 7200. Surface tension σ is chosen such that the Weber number $We = \rho_{\text{gas}}U^2L_{\text{apex}}/\sigma$ is 500.

The software affords adaptive grid refinement based on vorticity and interface curvature. Here the smallest mesh size is 2^{-10} times the box height, amounting to 128 mesh cells in the wave height L_{apex}.

The initial condition is a parallel mixing layer satisfying the continuity of velocity and shear strain at the interface location $y = 0$

$$u(y) = \begin{cases} \frac{1}{1+r}(\text{erf}(y/\delta) + r), & y > 0 \\ \frac{r}{1+r}(\text{erf}(y/\delta) + 1), & y < 0. \end{cases}$$

This velocity field is initially disturbed by a local vertical acceleration

$$f(x, y, t) = \kappa\phi(t)\text{e}^{(-(x/\ell)^2-(y/\ell)^2)}$$

with its amplitude quickly fading

$$\phi(t) = \begin{cases} \cos(\pi t/2t_{\text{stop}}) & t < t_{\text{stop}} \\ 0, & t > t_{\text{stop}}. \end{cases}$$

We took $\ell = \delta$, a forcing patch of the size of the mixing layer, and $t_{\text{stop}} = T_{\text{apex}}/100$. The amplitude of the forcing is $\kappa = 0.1/t_{\text{stop}}$.

Results

The evolution of the wave interface is shown in fig. 2.3 for four successive times. The first one is $T_{\text{apex}}/10$ where we can see the start of the wave as the result of the initial localized impulse. The wave has not taken yet its own distinctive shape. This is a time of the initial transient, where the cause of the wave is not yet forgotten. The second interface corresponds to $T_{\text{apex}}/2$, half way on the growth of the wave to reaching its peak height. Already at this time, we can observe the flapping of the wave's tongue and shedding of a liquid film. At $t = T_{\text{apex}}$, the wave has reached its maximum height, with a value corresponding approximately to $L_{\text{apex}} = 0.7rU^2/g$, materialized on the four graphs as a horizontal dashed line. At this time of largest size, we see that there has already been a strong activity of shedding liquid films and drops, some of which have free-fallen down to the original interface height. The last displayed interface position corresponds to $t = 1.5T_{\text{apex}}$: after reaching its maximum size, the wave collapses

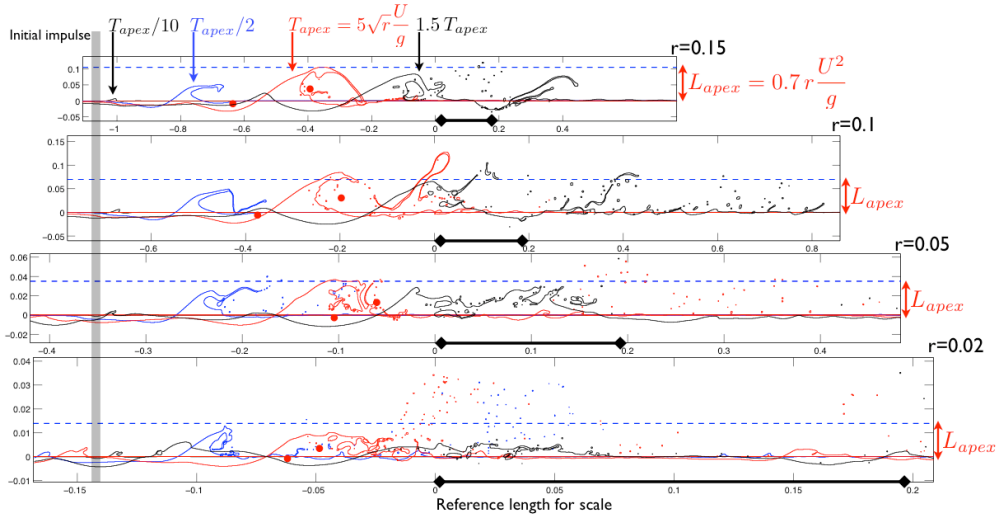

Figure 2.3: Position of the interface from numerical simulations at four instants of time and for four values of the density ratio. Relative sizes are scaled such as to emphasize the theoretical prediction.The positions of the center of mass of zones 1 and 2 at time T_{apex} are drawn as red dots. (From [9].)

progressively, losing its impetus into an intricate organization of vortices and drops.

The graphs for the four values of the density ratio r are displayed scaled such as to emphasize the theoretical scaling law. We can observe that the shape and behavior does not change significantly once properly scaled, at least for the values of r which we were able to simulate. The most significant difference comes from the behavior of shed drops downstream of the wave. Indeed, the present choice of the Weber number based on the gas speed U does not account for the fact that the wave has a slower speed as r is lowered. Thus the shearing power of the free-stream upon the tensed interface is larger for the lower gas densities. The second reason for difference in the drop behavior comes from the fact that once the drops have left the liquid wave, they are advected at the free-stream velocity while free-falling with little or no influence from the density ratio.

The effect of the density ratio on the wave height is displayed in fig. 2.4. The size of the wave is quantified using the measure inspired from the variation of the gravity potential energy h. Looking at the initial growth of the wave height, we would have expected initially different slopes, in agreement with the algebraic

law for the self-similar growth as shown on fig. 2.1. This is not observed here since with the present choice of parameters due to mesh size limitations, the wave unfortunately does not have time to realize its self-similar regime before reaching the size at which volume forces start to act. After this initial growth, the height shows a peak and subsequent decay as expected from the progressive collapse seen in fig. 2.3 after the apex. The simulation performed for the smallest value of the density ratio $r = 0.01$, a gas hundred times lighter than the liquid, could not complete to time T_{apex} and does not show the peak. The computation is characterized by an increasing difficulty as the the fluids have strongly different physical properties.

The test of the model for the wave growth is shown in fig. 2.4b); the scaling of the time as

$$t' = \frac{t}{\sqrt{r}U/g}$$

and height as

$$h' = \frac{h}{rU^2/g}$$

yields a gathering of the time evolution of the wave height for the five values of the density ratio, showing a coordinated behavior of the physical system as the density of the gas is progressively lowered. The plateau value for h' is about 0.45, and the peak is observed at a time t' of about 5.

2.2 Single-wave Kelvin-Helmholtz instability in channel flow

Contrary to the previous section in which we have studied the evolution of an isolated KH wave produced by a localized impulse force, here a more physical situation is considered. The configuration presented refers to an initially stratified two-phase gas-liquid flow confined in an horizontal channel. This kind of flow has just been analyzed theoretically from the point of view of the linear theory of temporal normal modes in the paper of Funada and Joseph [39], on the ground of viscous-potential theory. They obtained an explicit dispersion relation including the effects

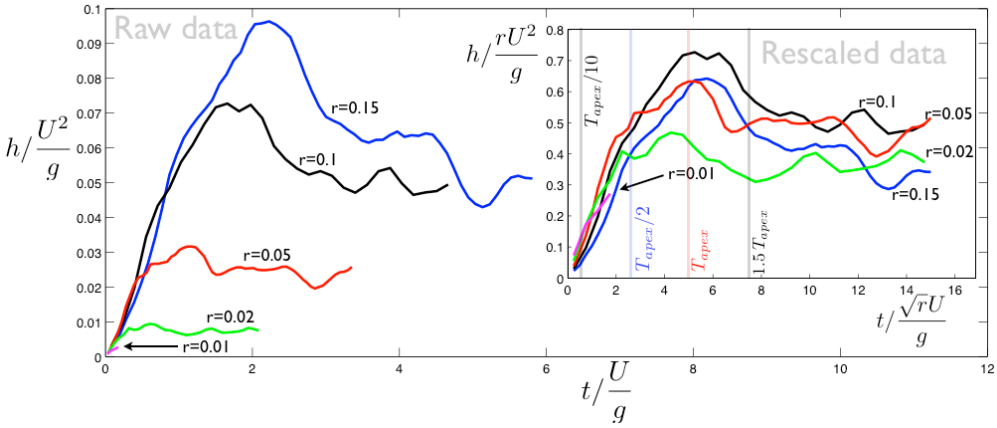

Figure 2.4: Effect of the density ratio on the evolution of the height of the wave. Inset: height and time are scaled with their theoretical values for the plateau. (From [9].)

of surface tension and viscosity (which is taken into account in the normal stress boundary condition only). Funada and Joseph [39] derived formulas for the growth rate and the wave speed, and employed neutral stability curves in order to compare their findings to experimental data referring to air-water flows. In general the critical value of velocity of stratified KH instability appears to be well predicted when the liquid layer is thin, otherwise it is overpredicted. The major reason of the disagreement between theory and experiments is that nonlinear effects play a major influence in the process of transition from stratified to slug flow, and therefore the finite-amplitude of the instability wave has to be taken into account starting from the early instants. As observed by Varga et al. [40], the treatment of the interface as an infinitely thin mixing layer (discontinuous interface) yields wavelengths which are incongruous with the experimental measurements. The inconsistency lies in the fact that in practical devices the shear between parallel flowing streams is produced by merging them from separate channels divided by a rigid boundary. This leads to the formation of a mixing layer having a continuous velocity profile, hence introducing a finite length scale.

A major difference from the theoretical work of [39] is that, while they considered a parallel flow configuration, with plug-velocity profile in both the fluids, here the flow is spatially devel-

oping, starting from a plug-plug profile at the channel entrance. In other terms, a physical situation analogous to that discussed in the experimental investigation of a round liquid jet by [40] is numerically analyzed. The sudden change of interface boundary condition produces the shear flow development and the emergence of a related finite-amplitude KH single wave, whose formation and break-up are studied in detail.

Model

A two-phase flow within a plane two-dimensional channel of height H and length L is analyzed by considering incompressible, immiscible and newtonian flow regimes. At the domain entrance boundary (left side), where the plug velocities of liquid and gas phases are denoted by U_l and U_g, respectively, the liquid occupies the region $0 < y < h_l$, while the gas is within the region $h_l < y < H$. Density and viscosity of liquid and gas are denoted by ρ_l and μ_l and by ρ_g and μ_g, respectively. The non-dimensional parameters governing the problem are Reynolds and Weber numbers of gaseous phase, defined as:

$$\mathrm{Re} = \frac{\rho_g U_g h_g}{\mu_g}, \qquad \mathrm{We} = \frac{\rho_g U_g^2 h_g}{\sigma}$$

(where σ is the gas-liquid surface tension, and h_g is the height of the gas region), the gas fraction $\alpha = h_g/H$ and density and viscosity ratios, $r = \rho_g/\rho_l$ and $m = \mu_g/\mu_l$. As an additional independent parameter one can consider the Reynolds number based on liquid phase or the velocity difference $\Delta U = U_g - U_l$. A sketch of the problem is shown in fig. 2.5, where the physical dimensions of the channel considered in the present investigation are also reported. No-slip boundary conditions are enforced at the channel walls, $y = 0$ and $y = H$.

Numerical experiments

Also in this case, the tool of numerical experimentation is the numerical simulation of Navier-Stokes equations for a system of two fluids. The code used is the plane two-dimensional version of

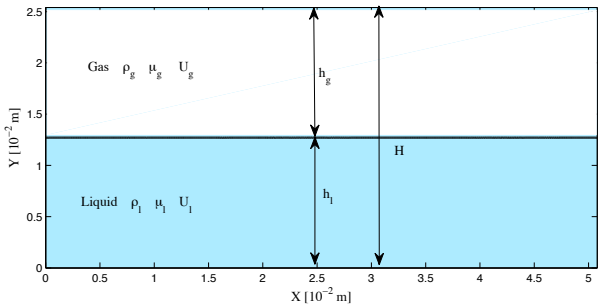

Figure 2.5: Schematic representation of the numerical domain. Both gas and liquid phases have a plug-velocity profile at channel entrance and the exit pressure is the atmospheric one. (From [10].)

an *ad hoc* in-house derived version of the popular public-domain SURFER code.

All the computations start assuming as initial condition plug velocity profiles in the gas and liquid phases separated by an undisturbed plane interface whose location is defined by the gas fraction α. All over the field the initial pressure is equal to the atmospheric value of 101.3 kPa, which is used also as constant outlet pressure.

The results hereafter presented refer to $\alpha = 0.5$, $r = 0.1$, $m = 0.018$. The physical domain is a channel having length $L = 5 \times 10^{-2}$ m and height $H = 2.5 \times 10^{-2}$ m. The influence of the surface tension was also investigated by varying the Weber number in the range from ∞ to 1×10^2, whilst gas Reynolds number is kept constant and equal to 5×10^3, and liquid Reynolds number is equal to 76.2. These values correspond to a velocity difference $\Delta U = 5.5$ m/s. In most cases a uniform 800×400 mesh (the length of 1×10^{-2} m is resolved by 160 grid cells) was sufficient in order to obtain convergent results as well as to simulate the very small droplets emerging from the film break-up. Numerical accuracy of the results was carefully estimated and a grid independence study was performed referring to the basic features (e.g. space-time evolution and interface shape) characterizing the single wave dynamics.

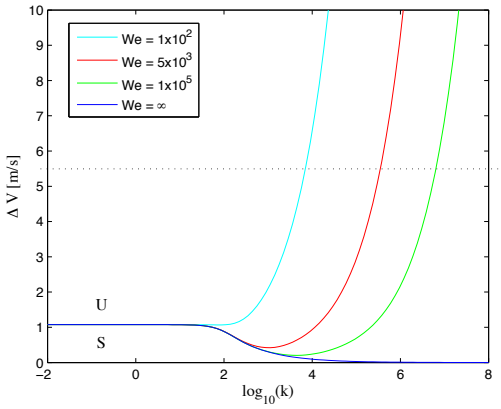

Figure 2.6: Neutral stability curves for the studied gas-liquid flow with a density ratio $r = 0.1$ and a viscosity ratio $m = 0.018$. The curves are obtained considering a gas-fraction $\alpha = 0.5$ and the four values of the Weber number used for the numerical simulations. (From [10].)

Results

As a preliminary consideration fig. 2.6 shows the neutral stability curves calculated using the viscous potential flow analysis explained in [39], and obtained for $\alpha = 0.5$ and four different Weber numbers. $\Delta V = U_g - U_l$ denotes the velocity difference between the two phases and k is the disturbance wavenumber. Note that when the surface tension is absent the flow is unstable for all wavenumbers. As expected, surface tension introduces a stability margin clearly evident at the higher We numbers, whereas for $\mathrm{We} = 1 \times 10^2$ the stability margin is influenced by viscosity. In any case, since all the present flow conditions refer to a velocity difference $\Delta V = 5.5$ m/s, the flow is expected to be unstable to any infinitesimal small disturbances. However, the flow configuration analyzed by [39] is parallel, whereas the present case features an intrinsic spatial development. As already mentioned in the introduction, this last occurrence is typical of practical devices where the mixing produces a continuous velocity profile relaxation that introduces in its turn a finite length scale. Hence, numerical computations have been carried out to simulate the appropriate unsteady free-interface flow field.

Fig. 2.7 shows typical colour maps of spatial distribution of pressure (relative to the atmospheric one) at the four Weber numbers considered before ($\mathrm{We} = \infty$; 1×10^5; 5×10^3; 1×10^2), in order to illustrate the stabilizing effect of the surface tension. The

interface shape, clearly depicted at the same early time instant of $t = 3 \times 10^{-3}$s, highlights the initial formation of a single traveling wave, which is much less pronounced at the lowest Weber number. It is evident that the emergence of the wave is due to the nonlinear amplification of finite-amplitude disturbances produced by the sudden change of inlet boundary condition. In more detail, just downstream of the channel inlet, merging of the two interacting currents produces a slow-down of the faster one (here the gas) and a speed-up of the slower one (the liquid). As a first consequence, in order to fulfill mass continuity requirement, the interface has to move towards the liquid, thus creating a wave valley. However, the normal stress balance, associated to this interface displacement, is not initially satisfied and the interface is pushed towards the faster gas, thus creating the wave crest. This mechanism is inherently nonlinear in the sense that the crest determines a local depression in the gas flowing over it (as can be predicted by means of the inviscid theory of small disturbances) which is transmitted to the liquid. As a final consequence, liquid is sucked into the crest giving rise to the nonlinear amplification occurrence. The standard KH mechanism, generating a wave train, is different because the flow remains parallel and the interface perturbation does not infer a suction mechanism. In fact, as will be discussed later on, the propagation velocity of the single wave may be evaluated by the equilibrium of the total pressure at the stagnation point located on the interface, whereas the velocity of the traveling waves of the classical KH comes out just from the mass continuity requirement.

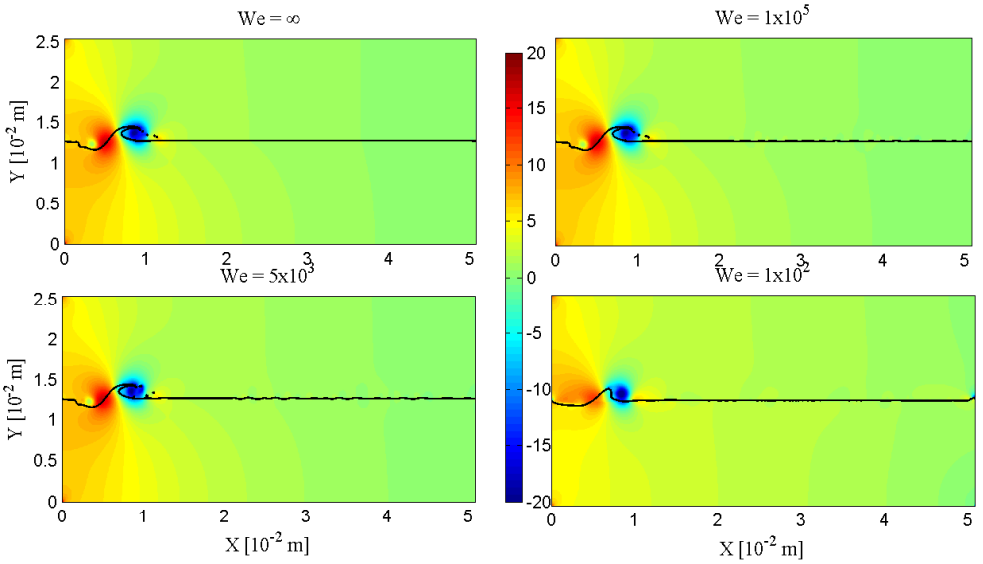

Figure 2.7: Color maps of relative pressure, measured in Pascal, for various Weber numbers at the time $t = 3 \times 10^{-3}$s. (From [10].)

As may be appreciated by looking at fig. 2.8, referring to $t = 8 \times 10^{-3}$ s, later on such a wave propagates downstream towards the not yet physically perturbed interface. Note also that its end rim breaks-up forming a certain number of small droplets. The maps reported in figs. 2.7 and 2.8 are reminiscent of the scenario illustrated by the experimental findings of [40] who proposed that the droplets are produced by a secondary Rayleigh-Taylor instability originating on the wave crests generated by a primary finite-amplitude KH instability.

The color maps reported depict clearly, especially for the higher time instant (fig. 2.8) quasi-periodic corrugations of the interface, which appear in the region not yet reached by the single-wave. The presence of such perturbations will be discussed later, in connection with the emergence of numerical errors leading to the formation of spurious flows of relatively small magnitude already mentioned above.

In regards to the basic characteristics of the single-wave, it is found that its propagation velocity, U_w, is constant when varying the Weber number. It is possible to estimate this velocity by

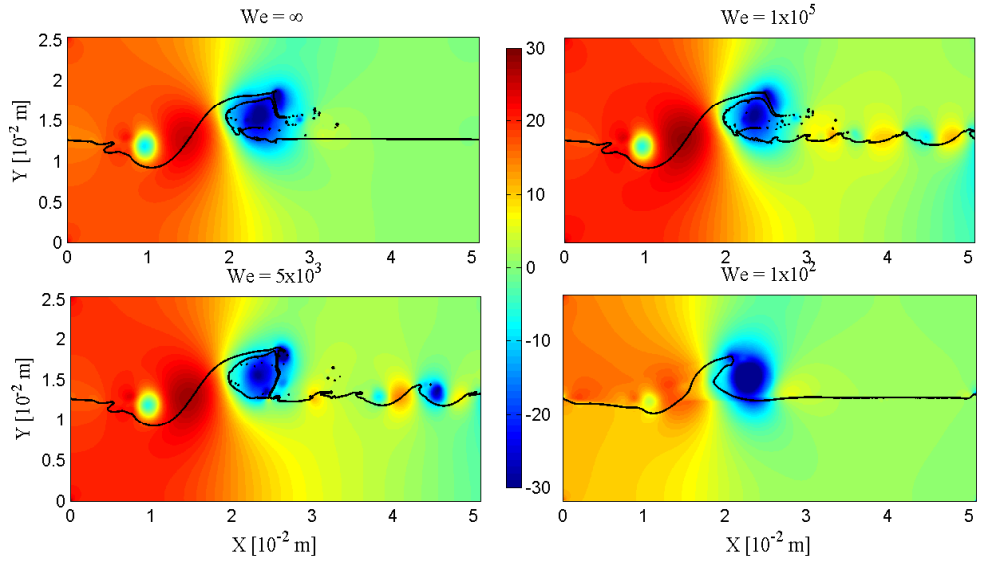

Figure 2.8: Color maps of relative pressure, measured in Pascal, for various Weber numbers at the time $t = 8 \times 10^{-3}$s. (From [10].)

means of a simple model. On the ground of the pressure color map depicted in fig. 2.9, where the streamlines are reported in a reference frame that moves with the wave, the balance of forces normal to the interface can be written:

$$P_g + \frac{1}{2}\rho_g (U_g - U_w)^2 = P_l + \frac{1}{2}\rho_l (U_l - U_w)^2 \qquad (2.5)$$

where P_g and P_l are the gas and the liquid-side pressure respectively.

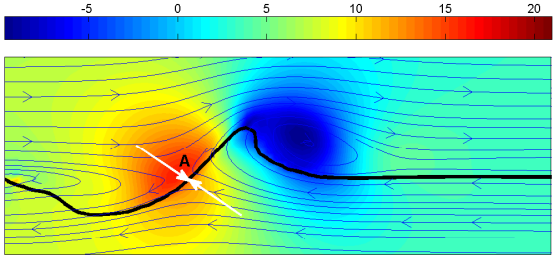

Figure 2.9: Color map of relative pressure, measured in Pascal, and streamlines for We = ∞ at $t = 1 \times 10^{-4}$s. (From [10].)

By assuming $U_l < U_w < U_g$ and by imposing local normal stress balance, $P_g = P_l$ (the effect of the surface tension can be neglected because the curvature is nearly null at the stagnation point A depicted in fig. 2.9, at least in the early instants), one obtains:

$$U_w = \frac{U_l + U_g\sqrt{r}}{1+\sqrt{r}}. \tag{2.6}$$

Thus, a valuable reference velocity coincides with the so called *Dimotakis speed*, i.e. the velocity of a generic vortex appearing in the two-dimensional fully developed mixing layer of two currents flowing with different velocities, [41]. For the present values of $U_l = 0.5$ m/s and $U_g = 6$ m/s, and $r = 0.1$, it is $U_w = 1.8$ m/s. This value is very close to the velocity observed for the numerically computed single wave at early times measured by following in time the movement of the first point of intersection between the wave and the position of the unperturbed interface (point A in fig. 2.9). The mean value of this velocity, calculated for $t \leq 5 \times 10^{-3}$ s, is 1.9 m/s. At later time instants we observed that the single wave accelerates and the *Dimotakis* velocity underestimates the propagation velocity. A representation of the movement of the reference point A for the wave is reported in fig. 2.10. Indeed, the very crude model employed in order to estimate the wave velocity can be applied just to early instants, when the shape of the wave is "bump-like". Afterwards, when nonlinear effects fully rule and the wave interface assumes the typical blunt shape depicted in the frames reported in fig. 2.8, separation of the gas stream past the wave renders reasonable the prediction of an acceleration.

The present results broaden the analysis of Hœpffner et al. [38] first of all because in the cited paper the wave is produced by an impulse force normal to the interface, whilst here it is generated by the sudden change of inlet boundary condition; furthermore, the Hœpffner's model is self-similar and the wave propagation velocity is constant, whereas we observed a wave acceleration. In the present contest the use of the *Dimotakis* formula is proved as well.

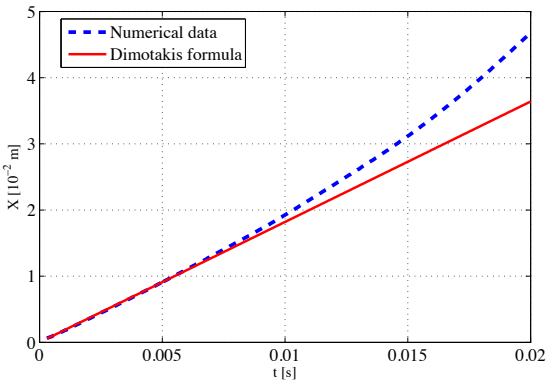

Figure 2.10: Space-time diagram of the position of point A of fig. 2.9 in which the *Dimotakis* formula (red line) is compared to the numerical data (blue dashed line). (From [10].)

Remarks

In section 1.1 the theory for a self-similar behavior of the KH instability has been extended to the case where gravity is present and a model for a nonlinear wave of gravity and wind has been elaborated. This wave initially grows until reaching a size at which the hydrostatic pressure drop balances the aerodynamic pressure drop. At this time, T_{apex}, a progressive collapse follows the apex of the growth preventing the emergence of a dissipative soliton that the idealized model (2.2) had left us to hope for. The model nevertheless provides insight into the growth process itself since the data for varying density ratio is reasonably gathered by the scaling of time as the square root of the density ratio and height as the density ratio in fig. 2.4.

The structure described can be identified with particular sea waves generated by wind, in other words we have studied the emergence and the evolution of very small waves resembling more to the process of the atomization, being no danger for the sailors, but playing an important role by creating much droplets: this wave, indeed, ejects much of its liquid body into airborne droplets as shown in fig. 2.3.

In section 1.2 a more physical configuration (considering the effects of both viscosity and surface tension) has been analyzed, always by means of numerical simulations based on VOF technique: the instability of a stratified two-phase gas-liquid flow in a

two-dimensional channel. In this case the emergence of the single KH wave is due to the sudden change of boundary condition at the channel entrance, from the discontinuous plug-plug velocity profile to the continuous one due to the formation of a mixing layer.

The propagation velocity of the wave has been numerically characterized and it has been theoretically analysed by a simple physical model, in order to highlight the differences from the classic KH wave velocity reported by Drazin [15].

The effects of the surface tension on the emergence of the single wave was studied by varying the Weber number from ∞ to 1×10^2. Moreover it was observed that the surface tension is the cause of small numerical errors, the spurious flows, in the region downstream of the single wave. Such spurious currents can be strongly reduced, or eliminated, by using more accurate numerical modelings, as shown by the results obtained by means of Gerris code, fig. 2.11. However, Gerris simulations confirm the emergence of a wavy behaviour of the interface downstream of the main single-wave (i.e., the still unperturbed part of the interface) which in the present problem is produced by a KH mechanism.

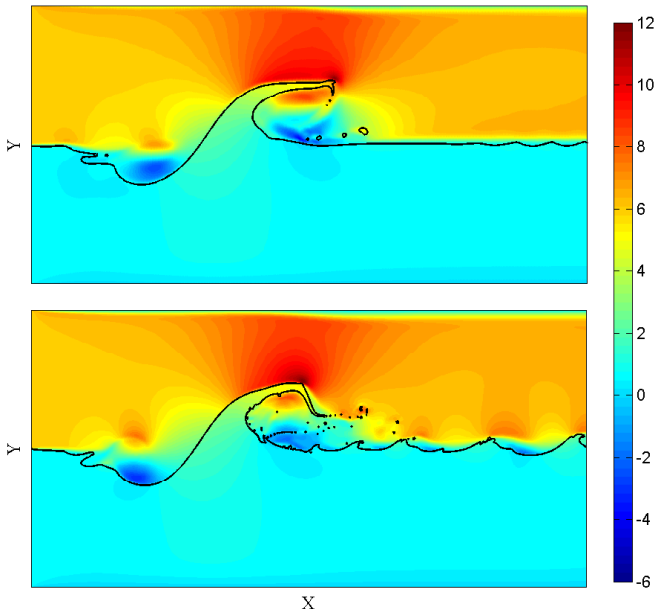

Figure 2.11: At the top a frame from the Gerris simulation and at the bottom a frame from our simulation for $We = 1 \times 10^5$. Color-maps represent the velocity magnitude, measured in m/s, at the time $t = 8 \times 10^{-3}$s. (From [10].)

Neglecting the problem of spurious flows, a "grid independence" study demonstrates that the Gerris code and our "in-house code" are in agreement with describing the basic features of the wave, i.e. the wave speed and its evolution in time. In fig.2.12 the space-time diagram of the wave position is reported as it is computed by the two different codes employed and with different grid refinements. The two "in-house code" executions discretize the whole domain by employing grids constituted by 600×300 and 800×400 nodes, to which a mesh spacing of respectively 8.47×10^{-5} m and 6.35×10^{-5} m corresponds. The Gerris simulations are carried out with three different levels of mesh refinement, namely Level 6, Level 8 and Level 9, corresponding to a minimum mesh spacing of respectively 3.97×10^{-4} m, 9.90×10^{-5} m and 4.90×10^{-5} m. The inset presents a zoom between the time instants 0.006-0.008 s showing a good agreement between the different simulations with a maximum dispersion of computed values of $x(t)$ equals to about 2×10^{-4} m.

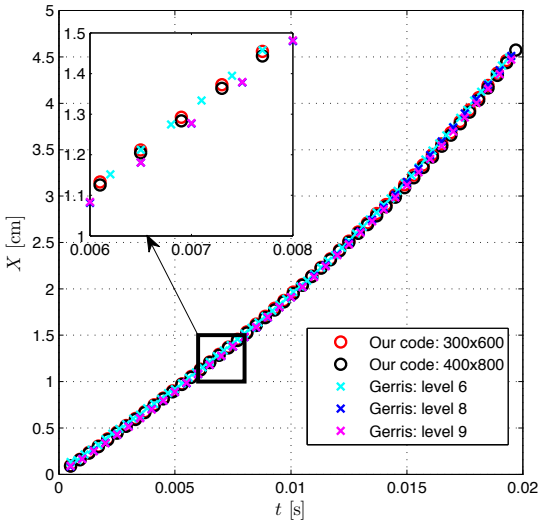

Figure 2.12: Space-time diagram of the wave position computed by the two different codes employed with different grid refinements.

In regard to the atomization problem, the evolution of this nonlinear wave is important to understand the mechanism of droplets formation. It is fair clarifying that, of course, the creation of droplets is a three dimensional phenomenon, but the KH primary instability of a liquid film under gravity is mainly two dimensional in short time. Moreover the main goal was only to study how this instability lead to the formation of a localized wave with a flapping tongue at the tip. This tongue is very fragile, weakly maintained by surface tension and it is stretched by the air flow away from the body of the wave and shaken and broken by the vortices that are shed periodically from the liquid obstacle.

2.3 Linear modal stability of viscous plane two-fluid Poiseuille flow

In this section we revisit the classical linear stability problem of two-fluid Poiseuille flow in a planar channel. Hydrodynamic stability of a thin layer of liquid bounded by a wall and sheared by gas plays an important role in many industrial processes such as lubrication system, atomization process, coating technology and

aviation applications, as the de-icing technology.

A pioneering analysis of the linear stability of two superimposed fluids of different viscosities in a channel was performed by Yih [16] who showed that viscosity stratification can induce instability in plane Couette-Poiseuille flow. The further huge amount of literature on the stability of two-phase flow shows that this type of flow is susceptible to instabilities of various kinds which have their origin in viscosity stratification, as demonstrated by Yih, density stratification, velocity profile curvature or shear effects. Indeed, unlike for the single-phase stability problem, where the Reynolds number is the only parameter, the formulation of two-phase stability problem requires at least six dimensionless parameters: viscosity, density and depth ratio, two Reynolds number and the Weber number.

In this section, considering the classification of instabilities made by Boomkamp and Miesen [42], we analyze the stability of a gas-liquid Poiseuille flow through an extensive parametric study, focalizing the attention on the occurrence of a mode coalescence phenomena between the interfacial mode, typical of two different fluids separated by an interface, and Tollmien-Schlichting mode, found in the classical hydrodynamic stability theory.

Model

The analyzed flow can be solved in cylindrical geometry, but because of its assumed symmetry, and especially if the liquid film is sufficiently thin, it can be considered two-dimensional.

Flow geometry is shown in fig. 2.13. Subscripts 1 and 2 denote the upper and the lower Newtonian fluid layer. Density, viscosity and thickness of the two fluids are expressed by ρ_i, μ_i and d_i, where $i = 1,2$. The flow is bounded by the wall of the channel and it is limited at the top by the axis of symmetry. The two layer are separated by an interface at $y = 0$ (note that in the reference system chosen, x denotes the streamwise direction and y the direction normal to the motion). Gravity effects are neglected.

The problem is non-dimensionalized with respect to the fluid 1.

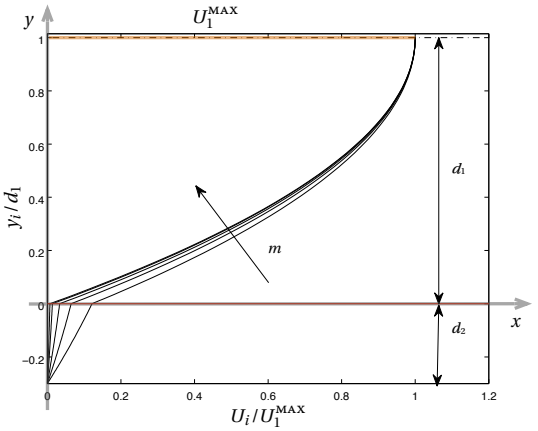

Figure 2.13: Base flow varying the viscosity ratio. d_1 is the thickness of the gas layer, d_2 is the thickness of the liquid layer.

It is possible to find out five dimensionless parameters

$$m = \frac{\mu_2}{\mu_1}, d = \frac{d_2}{d_1}, r = \frac{\rho_2}{\rho_1}, Re = \frac{U_1^{MAX}\rho_1 d_1}{\mu_1}, We = \frac{(U_1^{MAX})^2 \rho_1 d_1}{\sigma}$$

which are respectively the viscosity, the thickness and the density ratio, the Reynolds and the Weber numbers.

The base flow is a two-phase Poiseuille flow. The adimensionalized velocity profiles of the two layers are

$$\begin{cases} \dfrac{U_1(y)}{U_1^{MAX}} = -\dfrac{[\frac{1}{2}y^2 - y - \frac{d}{m}(\frac{d}{2}+1)]}{\frac{1}{2} + \frac{d}{m}(\frac{d}{2}+1)} & 0 \leqslant y \leqslant 1 \\ \dfrac{U_2(y)}{U_1^{MAX}} = \dfrac{\frac{1}{m}[-\frac{1}{2}y^2 + y + d(\frac{d}{2}+1)]}{\frac{1}{2} + \frac{d}{m}(\frac{d}{2}+1)} & -d \leqslant y \leqslant 0 \end{cases}$$

Stability problem

As in [16], the linear stability problem is formulated in two-dimensional cartesian reference system. We assume perturbations about the basic flow in the form of the non dimensional stream functions ψ_1 and ψ_2. The streamwise and cross-stream velocity components u and v are defined in both phase by

$$\begin{aligned} u_i &= \partial_y \psi_i \\ v_i &= -\partial_x \psi_i \end{aligned} \tag{2.7}$$

The unsteady infinitesimal disturbance can be expressed as

$$\psi_i(x, y, t) = \tilde{\psi}_i(y)\mathrm{e}^{\mathrm{i}k(x-ct)} \tag{2.8}$$

k is the streamwise wavenumber and c is a complex number, its real part represent the wave velocity while the imaginary part is the *growth rate* ($kc = \omega$, see section 1.3). A disturbance is unstable, stable and neutrally stable when the amplification factor is positive, negative and zero, respectively.

Substituting the 2.7 into the Navier-Stokes equations, eliminating the pressure terms and linearizing, we obtain the *Orr-Sommerfeld* equation for each layer

$$\begin{aligned}(U_1 - c)(\tilde{\psi}_1'' - k^2\tilde{\psi}_1) - U_1''\tilde{\psi}_1 &= \frac{1}{ikRe}(\tilde{\psi}_1'''' - 2k^2\tilde{\psi}_1'' + k^4\tilde{\psi}_1) \\ (U_2 - c)(\tilde{\psi}_2'' - k^2\tilde{\psi}_2) &= \frac{m}{ikrRe}(\tilde{\psi}_2'''' - 2k^2\tilde{\psi}_2'' + k^4\tilde{\psi}_2)\end{aligned} \tag{2.9}$$

The equations 2.9, together with the the boundary conditions, govern the stability problem.

The boundary condition at the wall, $y = -d$, are the classical *no slip* condition

$$\tilde{\psi}_2(-d) = \tilde{\psi}_2'(-d) = 0 \tag{2.10}$$

at $y = 1$ there is the condition of symmetry

$$\tilde{\psi}_1(1) = \tilde{\psi}_1''(1) = 0 \tag{2.11}$$

and at the interface, $y = 0$, we have to assure the continuity of the velocity

$$\begin{aligned}\tilde{\psi}_1(0) &= \tilde{\psi}_2(0) \\ \tilde{\psi}_1'(0) - \tilde{\psi}_2'(0) &= \tilde{\delta}(U_1'(0) - U_2'(0))\end{aligned} \tag{2.12}$$

the kinematic condition

$$\tilde{\psi}_1(0) = (U_1 - c)\tilde{\delta} \tag{2.13}$$

and the continuity of stress components

$$\begin{aligned}\tilde{\psi}_1''(0) - k^2\tilde{\psi}_1(0) &= m(\tilde{\psi}_2''(0) - k^2\tilde{\psi}_2(0)) \\ -\mathrm{i}kRe(c'\tilde{\psi}_1' + U_1'\tilde{\psi}_1) - (\tilde{\psi}_1''' - k^2\tilde{\psi}_1') + \mathrm{i}kRer(c'\tilde{\psi}_2' + U_2'\tilde{\psi}_2) \\ + m(\tilde{\psi}_2''' - k^2\tilde{\psi}_2'') - 2k^2\frac{m}{d}\tilde{\psi}_2' &= \mathrm{i}k^3ReS\frac{\tilde{\psi}_1}{c'}\end{aligned} \tag{2.14}$$

where $\tilde{\delta}$ is the perturbed interface, $c' = c - U(0)$ and $S = \frac{1}{We}$.

Writing the governing equations into a matrix form, we obtain a generalized eigenvalue problem

$$c\mathbf{M}\tilde{\mathrm{q}} = \mathbf{A}\tilde{\mathrm{q}} \tag{2.15}$$

introducing the perturbation vector $\tilde{\mathrm{q}} = [\tilde{\psi}_1, \tilde{\psi}_2, \tilde{\delta}]$, the unsteady operator **M** and the advection-diffusion operator **A**.

This problem has been discretized separately for each fluid by means of a *Chebyshev* pseudospectral code written in MATLAB programming language.

Results

We consider a gas-liquid flow with $r = 10$ and $m = 40$. These parameters are different from the air-water ones, but have however direct applications to liquid-gas atomization at high pressure. The other parameters varied are the Reynolds number, $Re = [100 - 5000]$, the Weber number and the depth ration, $d = [0.15, 0.2, 1, 8]$.

We start analyzing the effects of the increasing of n. In fig. 2.14 are reported the colour maps of the maximum growth rate and the neutral stability curves for the considered values of n and for $We = \infty$. For $d = 0.15$ the flow is unstable, while increasing the thickness of the lower fluid, already at $d = 0.2$, a neutral stability appears. With further increases of d the area of stability extends, but for $d > 1$, this trend inverts.

For $Re = 4000$ and $k = 1$, fig. 2.15 shows how the spectrum of the linearized Orr-Sommerfeld operator varies increasing d. As d increases, the the position of the leading eigenvalue shifts from the left to the right branch and for $d \geq 0.2$ the growth rate, c_i, is of one order of magnitude higher, as reported in fig. 2.16.

These data highlight that varying the thickness of the lower fluid, the nature of the leading eigenvalue changes. For $d \leq 0.2$, the most unstable mode is an *interfacial mode* (I) typical instability mechanism of thin liquid film injected into a fast gas stream. When the thickness of the lower fluid is slightly increased a new mechanism of instability due to a *mode coalescence* can be observed. This phenomenon occurs between the *Tollmien-Schlichting*

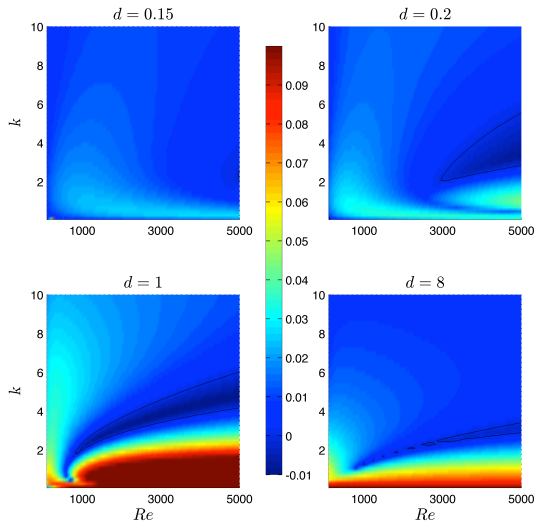

Figure 2.14: Colour maps of maximum growth rate varying d as a function of the axial wavenumbers k and Re for $m = 40$, $r = 10$ and $We = \infty$. The black lines represent the neutral stability curves.

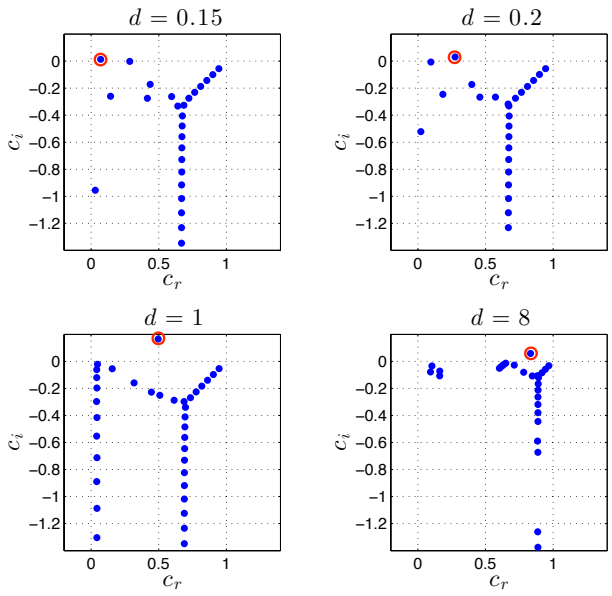

Figure 2.15: Spectrum of the linearized Orr-Sommerfeld operator for $k = 1$, $Re = 4000$, $We = \infty$ and varying the value of the thickness ratio d. The leading eigenvalue is circled in red.

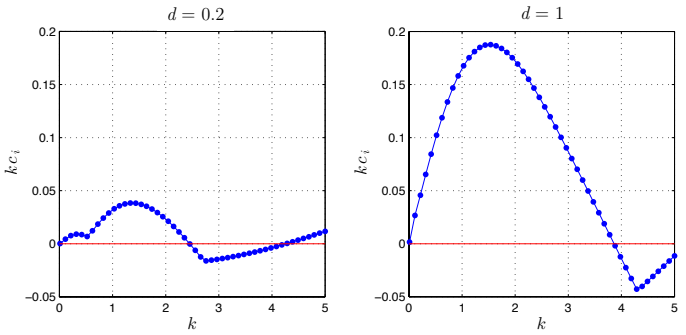

Figure 2.16: Maximum growth rate as a function of the streamwise wavenumber k for $r = 10$, $m = 40$, $Re = 4000$, $We = \infty$ and for two values of the thickness ratio $d = 0.2, 1$.

modes (TS) and the previous mentioned interfacial modes. The physics driving these two modes are quite different. The TS mode is caused by a combination of the vorticity production at the wall, the no-slip condition, and the viscous effect within the critycal layers and hence is also present in single-phase flows, while the I mode is driven by vorticity production at the interface due to a viscosity jump between the two fluids in play. As reported by [17], the critical parameter which introduces modes interaction is the film thickness.

Cohen and Hanratty [43] found experimentally some characteristics to identify an interfacial modes: the wavelength is from one to ten times the thickness of the liquid film and the wave speed is greater than the velocity at the interface. Analyzing the results obtained for $d = 0.2$, we find that the maximum growth rate, $kc_i = 0.039$, is riched by a disturbance characterized by $k = 1.33$. Thus the adimensional wavelength is of one order of magnitude greater than the liquid film thickness, $\lambda = 2\pi/k \sim 4.72$, and the adimensional disturbance speed is $c_r = 0.95$, while the velocity at the interface, adimensionalized respect to U_1^{MAX}, is $U(0) = 0.01$. These characteristics identify the leading eigenvalue as an interfacial mode.

For $d = 1$ the leading eigenvalue preserves the same wave velocity and wavelenght of an interfacial mode, $c_r = 0.95$ and $k = 1.54$, but the growth rate grows of one order of magnitude, $kc_i = 0.188$. Comparing the maximum growth rate as a function of k for $d = 1$ with the one reported in fig. 2.18, relative to a

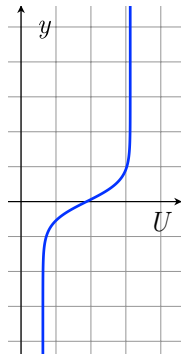

Figure 2.17: Hyperbolic tangent velocity profile of a mixing layer.

mixing layer with an hyperbolic tangent velocity profile, fig. 2.17, and for $Re = 4000$, governed only by the shear instability, we can note some similarities in the trend and in the order of magnitude.

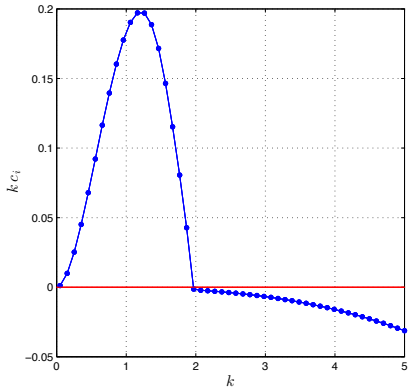

Figure 2.18: Growth rate as a function of the streamwise wavenumber k of the mixing layer for $Re = 4000$.

Indeed it is possible to deduce that when the thickness of the lower layer begins to grow, the mechanism of flow instability is due to a mode coalescence between I mode and TS mode.

It is interesting to investigate briefly the effects of surface tension on the stability of the studied flow. Varying the Weber number and fixing all the other parameters, $m = 40$, $r = 10$, $d = 0.2$, we obtain the neutral stability curves in fig. 2.19. The increase of surface tension has, as expected, a stabilizing effect, indeed for $We < 1000$ is possible to identify clearly a cutoff wavenumber k which divides the k-Re plane in two regions: the area above the cutoff wavenumber is stable, the one remaining below is unstable. Since the surface tension force is proportional to the curvature of the interface, and because the curvature is greater for short waves, its effects influence more the short waves modes, $k \geqslant 1$.

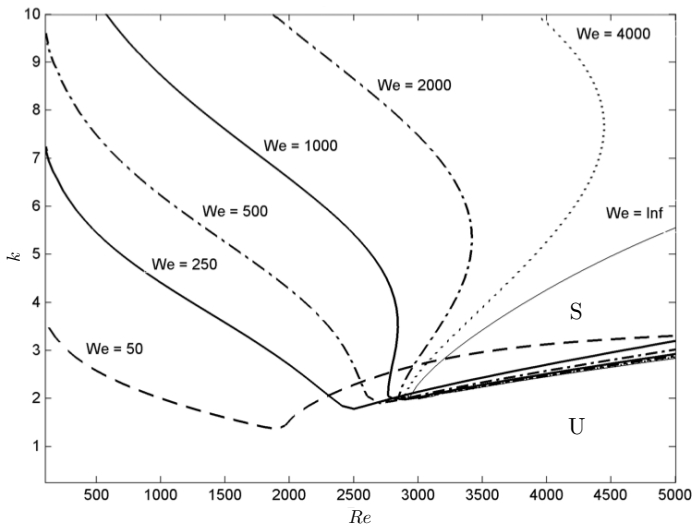

Figure 2.19: Effects of surface tension on the neutral curves for $d = 0.2$, $m = 40$ and $r = 10$.

Remarks

Unlike the single fluid problem, which results in a single unstable solution (Tollmien-Schlichting mode), the two-fluid problem has multiple unstable solutions (Tollmien-Schlichting and Interfacial modes). The parameters that influence the stability of the presented problem are the viscosity and density ratios of the two fluids, thickness of the sheared fluid layer and surface tension. For certain combinations of viscosity ratio and fluid thickness the Tollmien-Schlichting mode and the Interfacial modes interact resulting in a composite mode, that has the properties of both parent modes. A parametric study based on the different values of the thickness ratio and surface tension has been presented which has brought out some details of the mode coalescence and a parameters combination at which it occurs. In particular has been observed that for sufficiently thick sheared fluid layer, mode coalescence occurs between TS and I modes and when the lower fluid thickness increases, is not longer possible to distinguish the two separate modes and the composite mode dominates the instability problem. Another interesting feature is the increase of the amplification factors as the the thickness ration increases.

2.4 Concluding remarks

In this chapter we have analyzed the development of the instability of shear flows made up of two distinct immiscible fluids taking into account their different densities, viscosities and the tension acting at the interface that separates them. We have seen that when two immiscible fluids are flowing in parallel is common to witness the development of interfacial waves or even, for more rapid flows, the mixing of the two fluids as the surface eventually breaks into drops.

In industry such kind of flow forms the basis for the study of atomization. This has provided the motivation for the present work. The atomization process is characterized by the growth of initially wavy perturbations at the gas-liquid interface due to the classical KH mechanism, into more elongated liquid sheets. Three-dimensional destabilization of these sheets turns them into ligaments which could breakup into droplets. To describe the development of these structures, generated by the growth of nonlinear disturbances, direct numerical simulations are essential.

Our numerical results have revealed that the simple linear formulation of the KH theory, the mechanism that, as we have highlighted, sets the primary instability of a liquid film, cannot take into account many important real effects such as the finite thickness of the shear layer, the viscosity of the fluids and the nonlinear saturation of the initial disturbances.

Linear stability analysis, on the other hand, has allowed us to understand the physical character of the modes that govern primary instability. In particular it has been demonstrated that the viscosity ratio is the dominant factor of the instability: the viscosity jump at the interface produces the vorticity that drives the so called interfacial modes.

It has been possible to deduce how the linear stability problem of a two-phase flow is complicated considering all the parameters in play. Actually this has brought to the analysis of new and interesting phenomena such as the mode coalescence illustrated in the previous section. We have seen that, increasing the thickness of heavier fluid, I mode can have point of coalescence with TS mode generating a new mode that preserves some characteristics of the

typical instability mechanism of single-phase flow.

3

Stability of two-fluid flows in pipes

In this chapter we consider the dynamics of two immiscible fluids with different viscosities in circular pipes. Typical of these flows is the strong tendency to arrange themselves so that the low-viscous fluid is in the region of high shear. This has been explained by the *viscous-dissipation principle*, which postulates that the flow chooses an interface that could minimize viscous dissipation for a given flow rate, or, equivalently, maximize the volume flux for a given pressure gradient [44]. This "gift of nature" opens up very interesting possibilities for technological applications in which one fluid is used to lubricate another. An example is the lubricated pipelining in petroleum industries.

Water is often produced in large quantities with crude oil and the characteristics of this two-fluid flow are of great interest in horizontal pipelines transporting the crude oil to field treating facilities. The major beneficial effect of the introduction of water is the reduction of the pressure gradient along the pipeline and thus of the power necessary to pump a given quantity of oil [45]. Various arrangements of oil and water occur in experiments ([12], [46]):

- stratified flow with heavy fluid below;
- oil bubbles and slugs in water;
- a concentric oil core in an annulus of water (this is called Core-Annular Flow);

- wavy core flows;
- water in oil.

Of course, the flow pattern which appears most attractive from the viewpoint of pressure gradient reduction is the Core-Annular Flow (CAF).

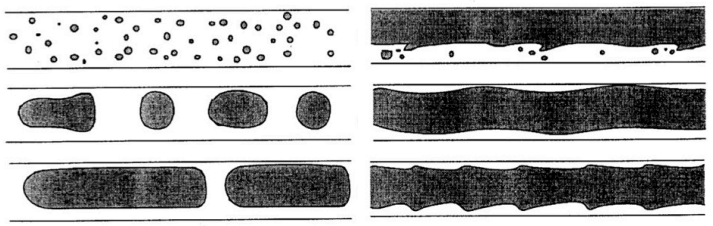

Figure 3.1: Flow types in horizontal oil-water flow in a pipe.

The science behind the technology of CAF has given rise to a large literature, in particular on stability studies. The flow types presented in fig. 3.1 are defined by stability, thus the theory of stability is the natural way to analyze the transition between them. Unfortunately most of the studies in literature are confined to "perfect" core-Annular flow (PCAF) only possible in horizontal pipes when the two fluids have the same density, such as to nullify gravity effects, and of interest in lubricated pipelining, for which linear stability analysis is reduced by normal mode to eigenvalue problem for ordinary differential equations. Studies on linear stability of PCAF were done by Hickox [47], Joseph et al. [48], Preziosi et al. [5], Joseph & Renardy [49] and many others. These stability analyses showed that this configuration is stable only when the more viscous fluid occupies most of the pipe, so the volume ration between the two fluids is a crucial factor. Actually, even in the case of a thin lubricating layer, the stability depends on flow conditions. For example, if the flow is slow, capillary instability is induced by interfacial tension. Inertia has a stabilizing effect [50] and the capillary instability can be completely stabilized by increasing the Reynolds number [5]. In general, the parameter range for which CAF is stable is very small.

Anyway the linear modal stability analysis cannot explain the transition to some flow types, like the emulsification of water in

oil, thus, looking at the comparison between theory and experiments, it is possible to see how the modal theory fails in some conditions. For this reason, in the present study we try to go beyond the classical results of modal stability analysis by carrying out *nonmodal stability analysis* of CAF taking into account three-dimensional perturbations, in light of the substantial transient growth found in the single-fluid pipe flow, [8].

3.1 Governing equations and parameters

Two liquids flowing in a cylindrical pipe of radius R_2 and infinite length are considered. The interface between the two liquids is given by $r = R(\theta, x, t)$, where t is time, (r, θ, x) are the cylindrical polar coordinates, and the corresponding components of velocity are denoted by $\mathrm{U} = (U, V, W)$. The region $0 \le r \le R_1$, where R_1 is a constant radius determined by the prescribed volumes of the two liquids in the unperturbed configuration, is occupied by the first liquid of viscosity and density μ_1 and ρ_1, respectively, while the second liquid (whose properties are denoted by μ_2 and ρ_2) is located in the region $R_1 \le r \le R_2$.

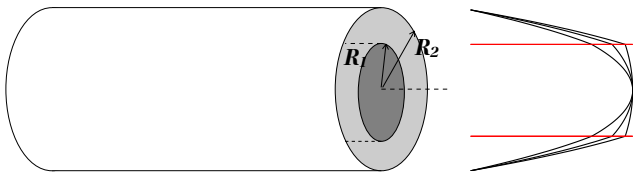

Figure 3.2: Geometry of Core-Annular Flow and base flow.

The equations of motion for an incompressible, Newtonian flow are:

$$\begin{cases} \rho_i \dfrac{\mathrm{DU}}{\mathrm{Dt}} = -\nabla P + \mu_i \nabla^2 \mathrm{U} \\ \mathrm{divU} = 0 \end{cases} \tag{3.1}$$

in which $i = 1$ when $0 \le r \le R_1$ and $i = 2$ when $R_1 \le r \le R_2$. Gravity term is neglected because we are considering two fluids

with the same density. Velocity have to satisfy the classical *no slip* condition at the pipe wall, $r = R_2$

$$\mathrm{U} = 0$$

and it is bounded at $r = 0$ by the *regularity conditions*. The equations on the interface, $r = R$, are

$$U = \frac{\partial R}{\partial t} + W\frac{\partial R}{\partial x} - \frac{V}{R}\frac{\partial R}{\partial \theta}$$
$$\langle \mathrm{U} \rangle = 0$$
$$-(\langle P \rangle + cT)\cdot \mathrm{n} + 2\langle \mu(\nabla \mathrm{U})^0_s \rangle \cdot \mathrm{n} = 0$$

in which the symbol $\langle\cdot\rangle$ represents the jump of a variable across the interface, c is the sum of the principal curvatures, T is the surface tension, $\mathrm{n} = \mathrm{n}_{12}$ is the normal to $r - R = 0$ from liquid 1 to 2. The first equation is the *kinematic condition* expressing as usual that the interface is a material surface; the other two equations represents six matching conditions corresponding to the continuity of three velocity components and the three stress components, the tangential stresses along axial and azimuthal directions and the normal stress along radial direction. Note that for the unperturbed flow the position of the interface corresponds to the radius of the core, $R = R_1$.

The base flow is modeled as *Hagen-Poiseuille* (HP) flow, driven by a prescribed pressure gradient, the velocity field being $\overline{\mathrm{U}} = (0, 0, \overline{W})$. Following [5], we have scaled the lengths with R_1 and the velocity with the centreline velocity,$\overline{W}(0) = W_0$, obtaining the following dimensionless velocity $\overline{W}(r)$:

$$\overline{W}(r) = \begin{cases} 1 - mr^2/(a^2 + m - 1), & 0 \le r \le 1 \\ (a^2 - r^2)/(a^2 + m - 1), & 1 \le r \le a \end{cases} \tag{3.2}$$

where $m = \mu_2/\mu_1$ is the viscosity ratio, and $a = R_2/R_1$ is the dimensionless outer radius of the pipe. Note that for the sake of simplicity the symbol r will denote hereafter the dimensionless radial coordinate. Equation 3.2 shows that $\overline{W}(r)$ is continuous across $r = 1$, but, because of the continuity of the shear stress across the interface, the derivatives of $\overline{W}(r)$ are different on the two sides of the domain at $r = 1$. Fig. 3.2 shows the base flow for

different values of m starting from the classic parabolic HP flow for $m = 1$.

Linearized equations and modal analysis

In order to perform the linear stability analysis, we classically perturb the base flow, so that the total velocity components, pressure and interface position are

$$\mathrm{U} = (u, v, \overline{W} + w), \quad P = \overline{P} + p, \quad R = R_1 + \delta(\theta, x, t) \tag{3.3}$$

where capital letters denote (total) perturbed quantities, small letters disturbances and bar refers to the base flow. δ is the interface disturbance.

After substituting the previous positions into the governing equations and the boundary conditions, it is possible to linearize them, following the classical steps of linear modal analysis, by assuming that quadratic perturbation terms are negligibly small. A further simplification is made by invoking quasi-cylindrical base flow assumption which means that the axial gradient are small, $\frac{\partial \overline{W}}{\partial x}$, and the general base flow can be approximated by $\overline{W} = \overline{W}(r)$. Thus the dimensionless linearized perturbation equations can be written:

continuity

$$\frac{1}{r}\frac{\partial (r\,u)}{\partial r} + \frac{1}{r}\frac{\partial v}{\partial \theta} + \frac{\partial w}{\partial x} = 0 \tag{3.4}$$

r-momentum

$$\frac{\partial u}{\partial t} + \overline{W}\frac{\partial u}{\partial x} = -\frac{\partial p}{\partial r} + \frac{1}{Re_i}\left[\nabla^2 u - \frac{u}{r^2} - \frac{2}{r^2}\frac{\partial v}{\partial \theta}\right] \tag{3.5}$$

θ-momentum

$$\frac{\partial v}{\partial t} + \overline{W}\frac{\partial v}{\partial x} = -\frac{1}{r}\frac{\partial p}{\partial \theta} + \frac{1}{Re_i}\left[\nabla^2 v - \frac{v}{r^2} - \frac{2}{r^2}\frac{\partial u}{\partial \theta}\right] \tag{3.6}$$

x-momentum

$$\frac{\partial w}{\partial t} + \overline{W}\frac{\partial w}{\partial x} = -\frac{\partial p}{\partial x} + \frac{1}{Re_i}\nabla^2 w \tag{3.7}$$

These equations have to be solved for both the inner and the outer field, occupied respectively by the the oil and the water. Re_i, in

fact, denotes the Reynolds number of each phase, $Re_i = \frac{W_0 R_1}{\nu_i}$. The corresponding variable's index (1 and 2) has been dropped just for simplicity.

The velocity components u, v, w have to respect the boundary condition $u = v = w = 0$ on $r = a$ and have to be bounded on $r = 0$. The conditions on the interface of the perturbation components have to be enforced always on the position of the unperturbed interface, $r = \eta = R_1/R_1$, due to the linearization process.

KINEMATIC CONDITION

$$u = \frac{\partial \delta}{\partial t} + \overline{W}\frac{\partial \delta}{\partial x} \tag{3.8}$$

CONTINUITY OF VELOCITY COMPONENTS

$$\begin{aligned} u &= v = 0 \\ w &= -\langle \frac{\partial \overline{W}}{\partial r} \rangle \delta \end{aligned} \tag{3.9}$$

CONTINUITY OF TANGENTIAL STRESS

$$\begin{aligned} \langle \frac{\zeta}{Re} \left[\frac{1}{2} \left(\frac{\partial v}{\partial r} + \frac{\partial u}{\partial \theta} - v \right) \right] \rangle = 0 \\ \langle \frac{\zeta}{Re} \left[\frac{\partial w}{\partial r} + \frac{\partial u}{\partial x} \right] \rangle = 0 \end{aligned} \tag{3.10}$$

CONTINUITY OF NORMAL STRESS

$$-\langle \zeta p \rangle + 2 \langle \frac{\zeta}{Re} \frac{\partial u}{\partial r} \rangle = \frac{J}{Re_1^2} \left(\frac{\partial^2 \delta}{\partial \theta^2} + \frac{\partial^2 \delta}{\partial x^2} + \delta \right) \tag{3.11}$$

where $\zeta_i = \rho_i / \rho_1$ is the density ratio, and J is the *Chandrasekhar* surface tension parameter, $J = \frac{T R_1}{a \rho_1 \nu_1}$. Note that the left side of eq. 3.11 involves jump terms whilst on the right hand side the Reynolds number is just Re_1. From these equations we obtain that the disturbance velocity component w is not continuous across the interface, second equation of 3.9, and its jump is proportional to the first derivative of the base flow $\overline{W}(r)$, different on the two side of the domain because of the continuity of shear stress for the base flow.

Fourier decomposition in azimuthal and axial direction, and temporal normal mode position, leads to the following distur-

bance quantities:

$$\begin{aligned}[u, v, w, p](r, \theta, x, t) &= [\mathrm{i}\tilde{u}, \tilde{v}, \tilde{w}, \tilde{p}](r) \cdot \mathrm{e}^{\mathrm{i}(n\theta + kx - \omega t)} \\ \delta(\theta, x, t) &= \tilde{\delta} \cdot \mathrm{e}^{\mathrm{i}(n\theta + kx - \omega t)}\end{aligned} \tag{3.12}$$

where $n \in \mathbb{Z}$ and $k \in \mathbb{R}$ are the azimuthal and the axial wave numbers, while ω is a complex number representing the temporal eigenvalue. The amplitude functions (eigenfucntions) are denoted by the symbol "~".

The dimensionless disturbances equations, 3.4-3.7, become

$$\begin{aligned}0 &= \left(\frac{\partial}{\partial r} + \frac{1}{r}\right)\tilde{u} + \frac{n}{r}\tilde{v} + k\tilde{w} \\ \omega\tilde{u} &= kW\tilde{u} - \frac{\partial\tilde{p}}{\partial r} + \frac{\mathrm{i}}{Re}\left[\left(\nabla^2_{n,k} - \frac{1}{r^2}\right)\tilde{u} - \frac{2n}{r^2}\tilde{v}\right] \\ \omega\tilde{v} &= kW\tilde{v} + \frac{n}{r}\tilde{p} + \frac{\mathrm{i}}{Re}\left[\left(\nabla^2_{n,k} - \frac{1}{r^2}\right)\tilde{v} - \frac{2n}{r^2}\tilde{u}\right] \\ \omega\tilde{w} &= kW\tilde{w} + k\tilde{p} + \frac{\mathrm{i}}{Re}\nabla^2_{n,k}\tilde{w}\end{aligned} \tag{3.13}$$

The boundary conditions for the outer field at the pipe wall are

$$\tilde{u}(a) = \tilde{v}(a) = \tilde{w}(a) = 0 \tag{3.14}$$

while at the axis of the pipe the amplitude functions have to satisfy the following *regularity conditions* (Ash and Khorrami [51])

$$\begin{aligned}&\tilde{u}, \tilde{v}, \frac{\partial\tilde{w}}{\partial r} = 0, \quad \tilde{p} \text{ finite} && \text{if} \quad n = 0 \\ &\frac{\partial\tilde{u}}{\partial r}, \tilde{u} + n\tilde{v}, \tilde{w}, \tilde{p} = 0 && \text{if} \quad |n| = 1 \\ &\tilde{u}, \tilde{v}, \tilde{w}, \tilde{p} = 0 && \text{if} \quad |n| > 1\end{aligned} \tag{3.15}$$

On the interface the conditions 3.8-3.11 become

$$\begin{aligned}
\langle\tilde{u}\rangle = \langle\tilde{v}\rangle &= 0 \\
\langle\tilde{w}\rangle + \langle\frac{\partial\overline{W}}{\partial r}\rangle\delta &= 0 \\
\tilde{u} - (k\overline{W} - \omega)\delta &= 0 \\
\langle\frac{\zeta}{Re}\left(\frac{\partial\tilde{w}}{\partial r} - \tilde{v} - n\tilde{u}\right)\rangle &= 0 \\
\langle\frac{\zeta}{Re}\left(\frac{\partial\tilde{w}}{\partial r} - k\tilde{u}\right)\rangle &= 0 \\
-\langle\zeta\tilde{p}\rangle + 2\mathrm{i}\langle\frac{\zeta}{Re}\frac{\partial\tilde{u}}{\partial r}\rangle &= \frac{J}{Re_1^2}(1-k^2-n^2)\tilde{\delta}
\end{aligned} \tag{3.16}$$

The governing equations 3.13, together with the boundary conditions, can be written into matrix form representing the following generalized eigenvalue problem

$$\omega\mathbf{M}\tilde{\mathrm{q}} = \left(\mathbf{L} + \frac{\mathrm{i}}{Re}\mathbf{V}\right)\tilde{\mathrm{q}} \tag{3.17}$$

where $\tilde{\mathrm{q}}$ contains inner and outer velocity and pressure variables, plus the displacement disturbance of the interface. $\mathbf{M}$ is the unsteady operator, $\mathbf{L}$ is the convection operator and $\mathbf{V}$ is the diffusive one.

To summarize, the problem 3.17 is characterized by five independent dimensionless parameters: m, a, ζ, J, Re_1 because the two Reynolds number are related by $Re_1/Re_2 = m/\zeta_2$. For sake of simplicity, according to [5], hereafter the two fluids are assumed to have the same density (thus ζ_2=1) and the parameter J will be taken fixed to the value $J = 2102$. The analysis hence has been made by varying m, a and the Reynolds numbers.

Numerical treatment

The generalized eigenvalue problem 3.17 has been discretized separately for each fluid phase by means of a Chebyshev pseudospectral code written in MATLAB programming language. For both fluids, the finite domain is mapped to the standard interval $[-1, 1]$ via a linear transformation. The *DMSuite* package of [23] has been used in order to obtain the discretized differential operators. Boundary conditions on pipe wall and axis are enforced

by the technique of replacing rows and interface conditions are treated as boundary conditions for each phase.

The spectral discretization of the spatial operator in equations has been used also to compute the transient growth function $G(t)$. The *Matrix Exponential* technique of [20] has been employed by adapting their schemes to the two-fluid flow case. Whereas the long-term behaviour is dominated by the least-stable eigenmode only, a set of eigenmodes is involved in the initial increase of energy density. To be sure of get the real value of this amplification, a convergence check based on the value of G_{MAX}, the maximum value of the transient growth curve, has been implemented in the used code. The number of the eigenfunctions taken to compute $G(t)$, N_f, increases till the difference between the value of G_{MAX} of the previous and the last calculation is less than a fixed tolerance value, $(G_{\mathrm{MAX}}(\mathrm{new}) - G_{\mathrm{MAX}}(\mathrm{old})) < 0.00001$. The convergence is always reached with $N_f \leq 80$. The eigenfunctions are sorted with respect to the imaginary part of the associated eigenvalue. An example of the dependence of G_{MAX} on N_f is shown in fig. 3.3.

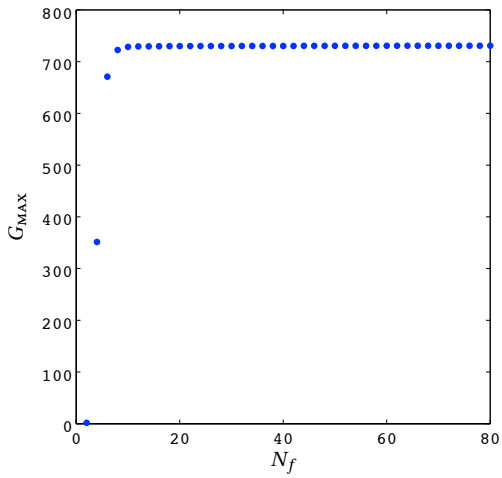

Figure 3.3: Dependence of the maximum energy amplification, G_{MAX} on the number N_f of included eigenfunctions. The used parameters are $k = 0$, $n = 1$, $a = \sqrt{2}$, $Re_2 = 3000$, and $m = 0.75$

The so called *optimal perturbation* has been calculated via *Singular Value Decomposition* (SVD) procedure (see [20]).

Three different versions of the code have been developed by modifying the system of equation 3.13. The first version of the

code (4 × 4 version) resolves the previous system of equations in the variable $\tilde{u}, \tilde{v}, \tilde{w}, \tilde{p}$; the second version (3 × 3) is obtained eliminating the variable $\tilde{p}$ by means of the x-Momentum equation; the last version (2 × 2) is obtained eliminating the two variable $\tilde{p}$ and $\tilde{w}$ using respectively x-Momentum and the Continuity equations. A convergence study has been performed for these codes: for most of the computations a total number of 170 collocation points has been adopted and an *ad hoc* procedure has been developed in order to split the total number of collocation points between the two phases, depending on the values of a and m.

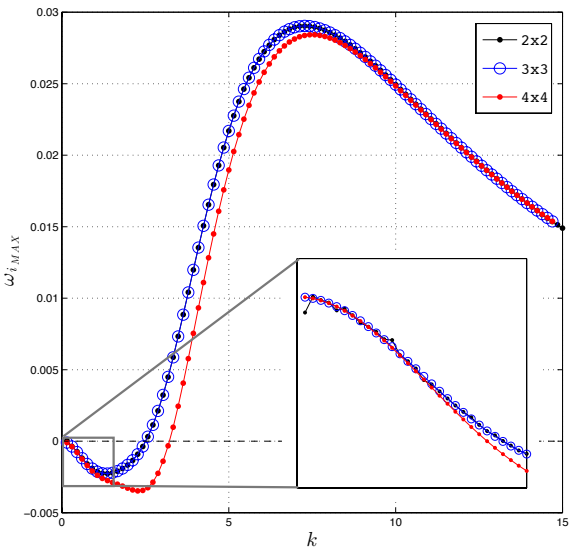

Figure 3.4: Growth Rate as function of the wavenumber k for $a = 1.43$, $m = 0.5$, $Re_1 = 26.42$, $J = 0$. The three curves have been computed by means of different versions of the used code. In the inset a zoom of the area $0 \leq k \leq 1$ is reported.

The validation of each code has been carried out reproducing the maximum growth rate curve reported in fig. 2 of Preziosi et al. [5]. In fig. 3.4 it is possible to notice that the 3 × 3 version of the code is the one that best fit the results of both the others two: the 2 × 2 achieves reliable results for $k > 1$, while the 4 × 4 is of high accuracy for $k \to 0$. This is due to the maximum order of derivative present in the system of equations used in the codes: the more the derivative order is high, the more significant accuracy errors may appear. For example in the 2 × 2 code we find forth-degree derivatives and for this reason, although this code is the best one in terms of computation time, the 3 × 3 is the more

convenient concerning accuracy.

3.2 Nonmodal instability of Core-Annular Flow

In order to compare the results of this section with the standard single fluid flow in a pipe, we use a mean Reynolds number defined as $Re_m = \frac{\overline{\rho}\overline{W_0}R_2}{\overline{\mu}}$ where $\overline{\mu} = \frac{R_1^2\mu_1 + (R_2^2 - R_1^2)\mu_2}{R_2^2}$. A similar relation holds for $\overline{\rho}$.

Firstly some illustrative example of eigenvalue stability analysis are considered for two typical configurations.

The most unstable growth rate is reported in figs. 3.5 and 3.6 as a function of axial wavenumber k and of Reynolds number, for the cases $m = 0.5$ and $a = 1.15$ (fig. 3.5) and $m = 0.75$ and $a = \sqrt{2}$ (fig. 3.6) and for the first four azimuthal modes $n = 0, 1, 2, 3$. These figs. show the maximum growth rate in function of both the external Reynolds number Re_2 (right vertical scale) and of the mean Reynolds number Re_m (left vertical scale). The continuous black line corresponds to the marginal stability. The case relative to fig. 3.5 is representative of a *narrow gap* physical situation, while that of fig. 3.6 is relative to an equal volume flux configuration.

One may see that passing from the narrow gap to the *wide gap* case produces a remarkable change in the topology of the unstable region. The narrow gap case is more stable in the sense that there are ranges of low Reynolds numbers in which the flow is stable for all wavenumbers, while in the wide gap case a Reynolds independent instability is detected, which is confined only to axisymmetric disturbances ($n = 0$) and affects long waves ($k < 1$).

Note that in both cases the maximum growth rate (related to the so-called *interfacial mode*, at least in the unstable regions) is quite small in the dimensionless units employed here, scaled by W_0/R_1. For this type of flow a generalized capillary instability (i.e. a capillary instability modified by shear) affecting very low Reynolds numbers and long waves, is already documented by previous researcher (for example figs. 8-15 of [5]). In the presented computations this instability is out of the range of Reynolds number discussed in fig. 3.5, while in fig. 3.6 it merges with the upper branch of unstable modes.

The results of non-modal analysis of the case relative to fig. 3.5

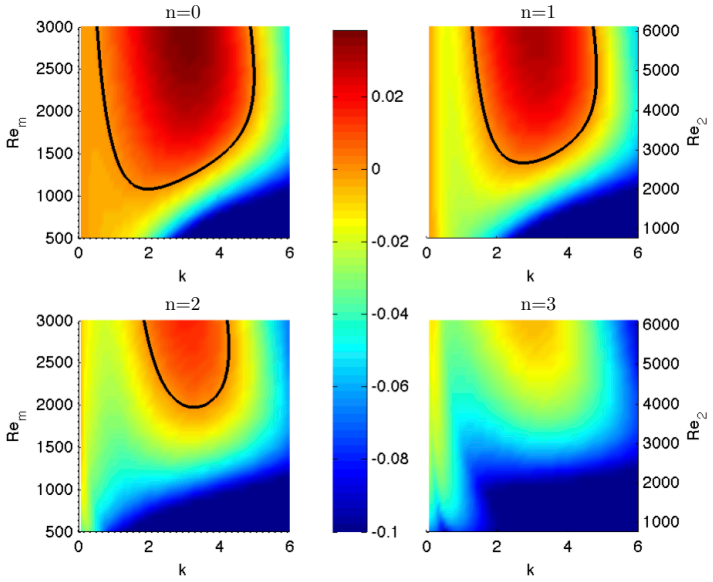

Figure 3.5: Maximum growth rate of the most unstable disturbances as a function of axial wavenumber k and Reynolds number. $m = 0.5$, $a = 1.15$. (From [11]).

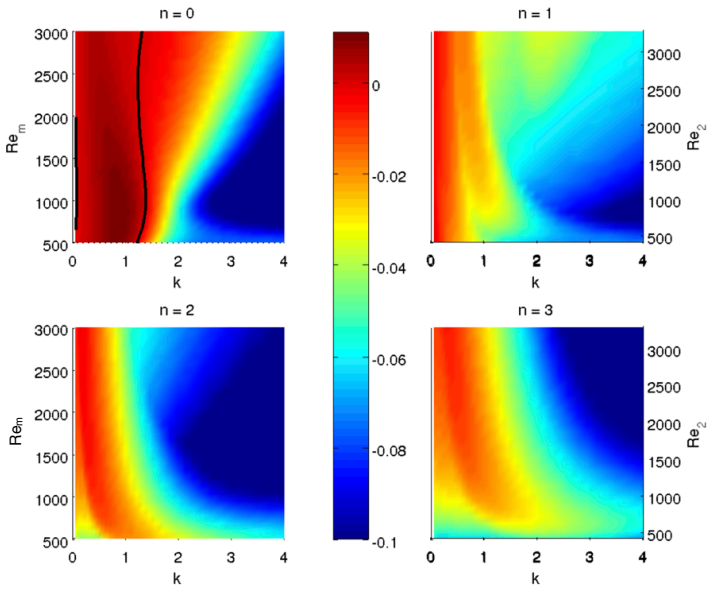

Figure 3.6: Maximum growth rate of the most unstable disturbances as a function of axial wavenumber k and Reynolds number. $m = 0.75$, $a = \sqrt{2}$. (From [11]).

are reported for azimuthal wavenumbers $n = 1$ and 2 in fig. 3.7. The color-map is relative to the natural logarithm of the maximum value G_{MAX} attained by the growth function over different values of k and of Reynolds number. The blank areas in this figure, and in the subsequent fig. 3.9, are relative to regions in which an exponential instability is present, for which G_{MAX} is infinite. For this particular narrow gap case the level of energy amplification of axisymmetric disturbances ($n = 0$), as well as of disturbances having higher azimuthal wavenumbers (not shown herein) is quite small and hence the cases $n = 1$ and 2 have been selected as the most dangerous from the point of view of the transient amplification of disturbances.

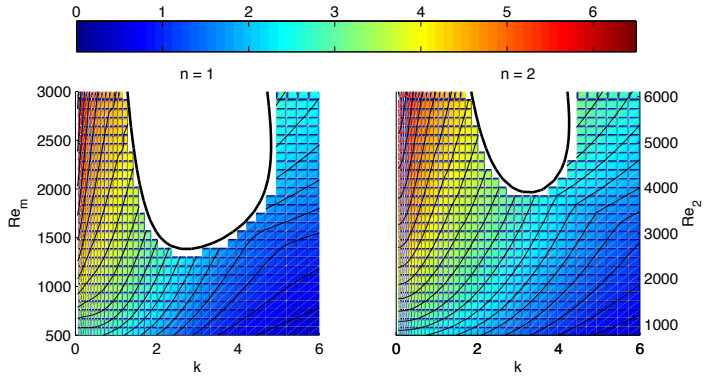

Figure 3.7: Natural logarithm of maximum non-modal amplification of energy G_{MAX} as a function of axial wavenumber k and of Reynolds number. $m = 0.5$, $a = 1.15$. (From [11]).

It is evident that long waves are affected by significant transient amplification, which increases by increasing Reynolds number; however, the regions in which the transient growth is higher are also regions of eigenvalue instability at different axial wavenumbers. As already discussed, the growth rates of these exponential instability is quite low, and hence one may conjecture that in some situations the algebraic growth of asymptotically stable long waves disturbances can be fast enough to overcome the slow exponential growth of energy of unstable disturbances at short times. Moreover, a third effect should be considered: nonmodal mechanisms can affect also the evolution of exponentially unstable modes at short times, enhancing their growth in a transient period before the exponential growth sets in. In this situation the physical rel-

evance of transient growth effects has to be carefully discussed and hereafter a comparison of energy evolution between different perturbations, obtained under the combined effect of modal and nonmetal mechanism is shown in fig. 3.8.

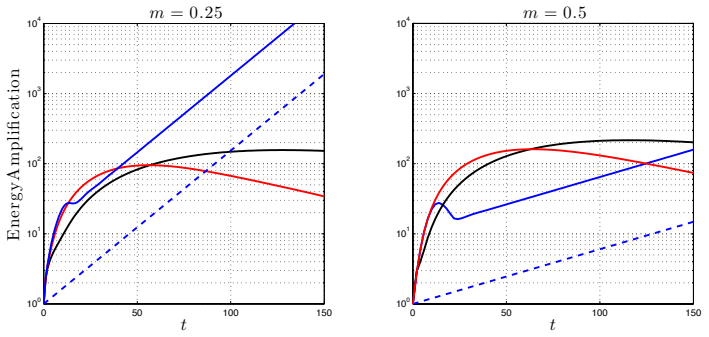

Figure 3.8: Energy amplifications of different perturbation for $Re_m = 2000$, $a = 1.15$ and two different viscosity ratios: $m = 0.25$ and $m = 0.5$. In both figures the solid blue line represents the transient energy growth of two asymptotically unstable disturbance ($k = 2$ $n = 1$), whose growth rate is reported as a dotted line. Black and red lines represent the transient growth of two asymptotically stable disturbances: for $m = 0.25$, $k = 0.001$ $n = 1$ (black line) and $k = 0.001$ $n = 2$ (red line); for $m = 0.5$, $k = 0.01$ $n = 1$ (black line) and $k = 0.01$ $n = 2$ (red line). (From [11]).

In this figure two typical situations, relative to $Re_m = 2000$ and $m = 0.25$ and $m = 0.5$, are depicted. In the lower viscosity ratio case (left figure) although the exponential instability of $k = 2$ $n = 1$ disturbance (blue line) has a quite low growth rate ($\omega_i = 0.025$) it is affected by non normality of the governing operator in such a way that at short times it reaches higher levels of energy which are comparable to purely algebraically growth of asymptotically stable disturbances for $k = 0.001$ $n = 1$ (black line) and for $k = 0.001$ $n = 2$ (red line). In the right figure the effects of non normality on the unstable disturbance $k = 0.01$ $n = 1$ are less pronounced and asymptotically stable long wave disturbances are able to accumulate energy more efficiently at short times are observed.

The results of non-modal analysis for the case of fig. 3.6 are reported in fig. 3.9. Significant transient growths occur for all helical modes ($n \geq 1$) and affect long and mid-range wavenumbers, while for axisymmetric disturbances the non modal amplification is practically negligible. This situation is different from the previous one, since the region of exponential instability is now present only for axisymmentric disturbances, for which G_{MAX} levels are quite low (the maximum being around 10). Hence the exponential instability is expected to play a minor influence at short time instants, when higher levels of amplification should be reached by

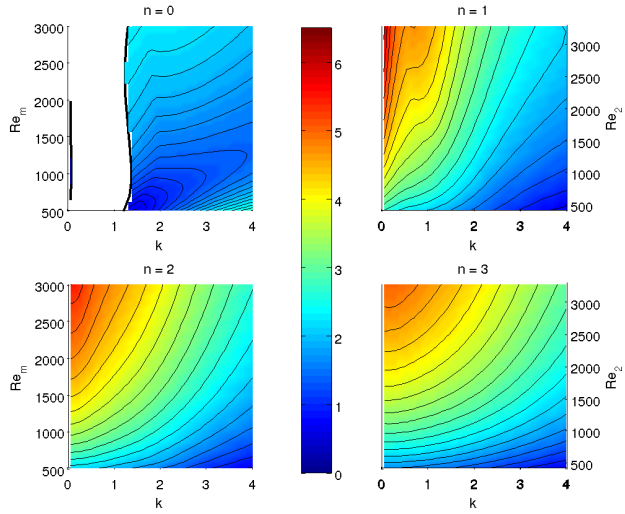

Figure 3.9: Natural logarithm of maximum amplification of energy G_{MAX} as a function of axial wavenumber k and of Reynolds number. $m = 0.75$, $a = \sqrt{2}$. (From [11]).

non-symmetric disturbances, for which non-modal mechanisms are effective.

The main question arising in this situation is if the nonmodal mechanism of non axisymmetric azimuthal wavenumbers is able to yield levels of energy amplification sufficiently high to break up the flow before the slow exponential instability, affecting axisymmetric disturbances, sets in. This question cannot be answered by considering the values of G_{MAX} alone, as it is done in figs. 3.7 and 3.9, because they do not give any information on the times at which the maximum energy amplification occurs.

The values of the energy amplification $G(t)$ as a function of time t are reported in fig. 3.10 for the usual azimuthal and axial wavenumbers and the same parameters of fig. 3.9, at the fixed value of Reynolds number $Re_m = 3000$. The horizontal line depicted in the upper left panel of the figure (relative to $n = 0$) indicates the critical wavenumber separating exponentially stable and unstable disturbances. The region below this line represents energy amplifications due to unstable disturbances which are going to grow monotonically in time. In all the other cases the energy amplifies trough a transient nonmodal mechanism and

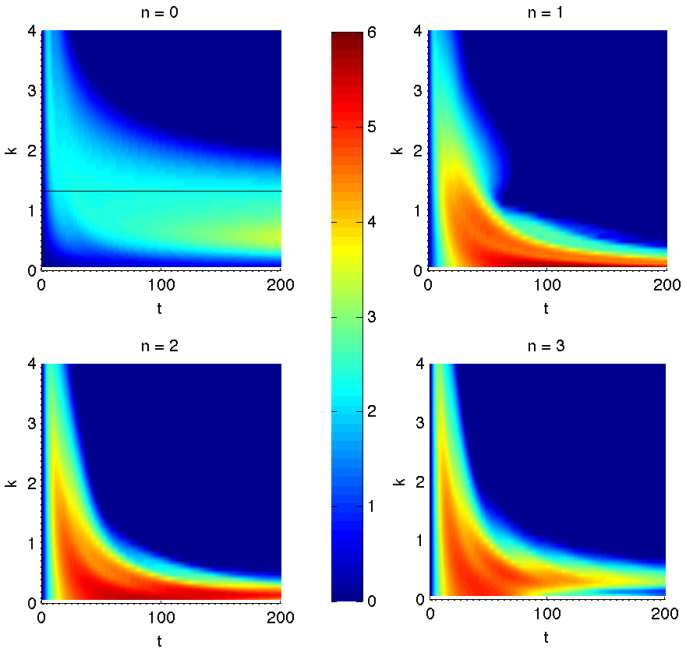

Figure 3.10: Natural logarithm of energy amplification G as a function of non-dimensional time t and of axial wavenumber k. $m = 0.75$, $a = \sqrt{2}$ and $Re_m = 3000$. The solid line for $n = 0$ indicates the critical wavenumber separating exponentially stable and unstable disturbances. (From [11]).

hence the growth function is going to decay as time increases. In fact, fig. 3.10 shows that at intermediate times the highest levels of energy amplification (up to 400) are reached by stable spiral disturbances having long waves ($k \ll 1$), well before the slow exponentially unstable axisymmetric disturbances reach a sufficiently high amplitude. This situation has been encountered also at different values of Reynolds number and m.

In order to give some insights on the observable structures in real flows, the analysis of the so-called *optimal perturbations* is considered. It is worth to recall that the optimal perturbations are defined as the initial perturbations, of velocity and displacement variables, that undergo the maximum value of the gain function $G(t)$ and hence experience the maximum energy amplification during their time evolution. Our analysis focuses on the particular case of radius ratio $a = \sqrt{2}$ and mean Reynolds number of 2500. The structures of the optimal perturbation in the r-θ plane are reported in fig. 3.11 for the case $n = 1$ and for two values of the

viscosity ratio ($m = 0.9$ and $m = 0.3$) and of the axial wavenumber ($k = 0.01$ and $k = 1$). The red circumferences show the location of the unperturbed interface. The values of m and k have been chosen with the following motivations. The two cases $m = 0.9$ and $m = 0.3$ highlight the differences between present results and the classical results of non-modal instability of the HP flow of a single fluid in a pipe ($m = 1$). The structure of the optimal perturbations in this particular single phase configuration (see Schmid and Henningson [20]) is very similar to the case $m = 0.9$ illustrated in the left column of fig. 3.11. On the other hand, the two values $k = 0.01$ and $k = 1$ are relative to two different amplification mechanisms; the former ($k = 0.01$) is pertinent to planar disturbances and is already present in the single fluid (planar disturbances have been shown to be the most dangerous perturbations in the nonmodal amplification for HP flow), while the latter ($k = 1$) is relative to a new mechanism of energy amplification which is peculiar of two-fluid flows, as will be briefly discussed hereafter.

The optimal perturbation for $k = 0.01$ remains basically unchanged both in the "almost-single-fluid" case $m = 0.9$ and in the full two-fluid case $m = 0.3$. This indicates that the long-wave mechanism of energy amplification encountered in the two-fluid system is basically the same as the typical one present in the single-fluid flow, namely a "lift-up" mechanism of streamwise vortices generating streamwise streaks. On the contrary, the optimal perturbation relative to $k = 1$ for the case $m = 0.9$ has a different nature since it dramatically changes when the viscosity ratio is reduced to the value $m = 0.3$. Thus, the energy amplification due to the nonnormal character of the linearized two-fluid operator at moderate wavenumbers (e.g., the case $n = 1$ $k \approx 1$) is peculiar of the two-fluid system and the perturbations that experience the maximum transient amplifications are of 'ring' type, with most of the structure confined within the annular region of the less viscous fluid.

In order to highlight the differences and the similarities between the CAF and the Hagean-Poiseuille flow, the effect of viscosity ratio on G_{MAX} are show in fig. 3.12. The viscosity ratio is increased from 0.1 (black line) to 0.7 (red line). The presence

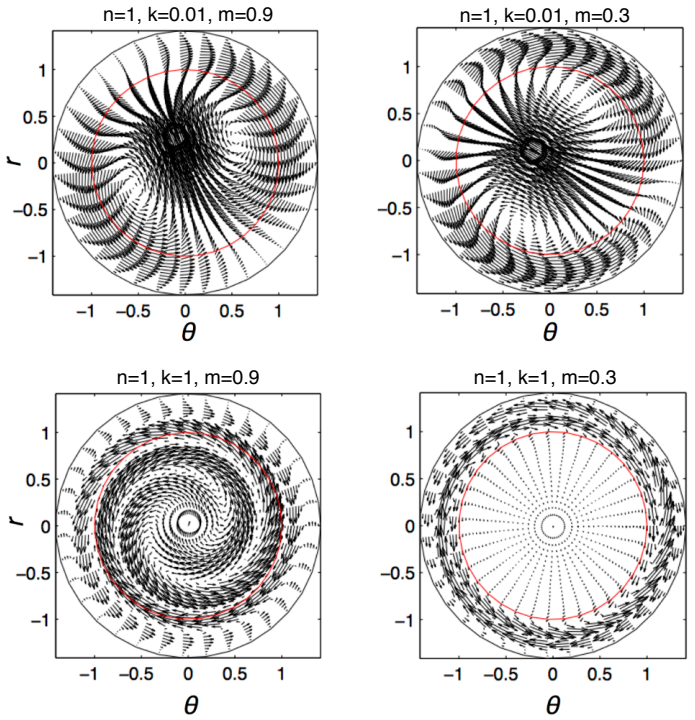

Figure 3.11: Selected optimal perturbations in the $r-\theta$ plane. $a=\sqrt{2}$ and $Re_m = 2500$. Left column $m = 0.9$, right column $m = 0.3$. (From [11]).

of two zones of high transient growth is clearly visible especially for the smaller values of m at $n = 1$ (remember that small m implies a strong discontinuity in first derivative of the base flow): the first one is characterized by long waves, typical transient growth found in single-fluid pipe flow (as just said referred to fig. 3.11), the second one is characterized by $k > 1$. These latter transient phenomena are peculiar of two-fluid pipe flow, and, in effect, increasing m the values of the energy amplification of these disturbances decrease. Anyway also for CAF the highest level of energy are reached by the long wave mechanisms for $n = 1$.

To support the similarities between two-fluid and single fluid flow in pipes, the distribution and the relative fractions of total energy among streamwise, radial and azimuthal velocity components of the two optimal perturbations shown in fig. 3.11 for $m = 0.3$ have been computed and reported in fig. 3.13. As shown by Bergstrom [52] for the single-phase flow (his results are repre-

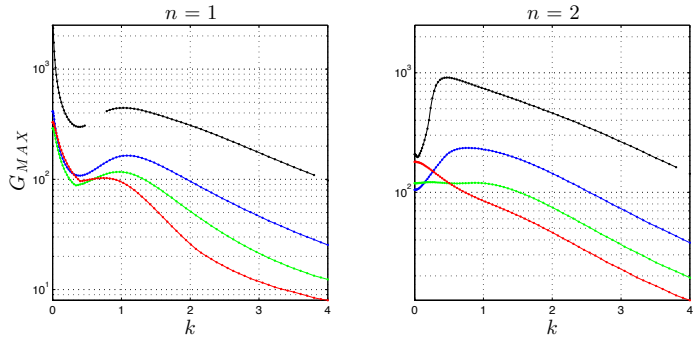

Figure 3.12: Logarithm in base ten of maximum nonmodal amplification energy G_{MAX} as a function of the axial wavenumber, k, for $Re_m = 2500$, two values of n and four different viscosity ratios: $m = 0.1$ (black line), $m = 0.3$ (blue line), $m = 0.5$ (green line) and $m = 0.7$ (red line).

sented by the dotted lines), for $k = 0.01$ at $t = 0$ almost all energy is in the azimuthal and radial components (respectively the read and blue lines) while negligible energy is in the streamwise component. When t is increased, the streamwise component starts to dominate rapidly: this is the only component that grows for small k. For $k = 1$ almost all the amplification is related to the streamwise component too, but here also the other components exhibit an amplification from their initial values, especially the azimuthal one. These results show that the energy distribution between the velocity components has basically the same behavior both in CAF and in HP flow.

To investigate the dependence on the time at which a perturbation achieves its maximum possible energy amplification, initial disturbances reaching their optimal amplification at chosen times, t_0, have been computed (t_0 are different from t_{MAX}, the time characterizing G_{MAX}). Recall that at time $t = t_0$ the curves displaying the energy density of these particular initial disturbances are tangent to the maximum growth curve. In fig. 3.14 the maximum growth curve for $Re_m = 2500$, $m = 0.3$, $a = \sqrt{2}$, $n = 1$ and two different values of k, $k = 0.01$ and $k = 1$ (see the optimal perturbation in the right column of fig. 3.11) are reported by the black dashed lines, while the blue lines represent the energy evolution of some initial perturbations tangent at the maximum growth curve in the points marked by the red dots. The results shown in this fig. lead to the conclusion, already discussed for HP flow in [8], that for a disturbance almost two-dimensional ($n = 1$ and $k = 0.01$) the

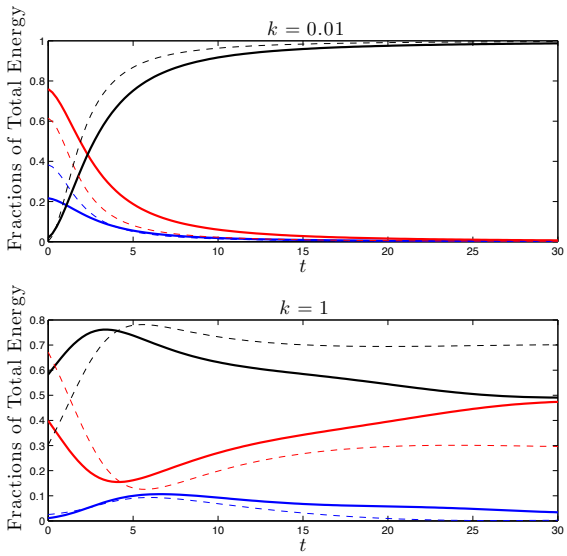

Figure 3.13: Relative fractions of total energy for different components of velocity for CAF at $Re_m = 2500$, $m = 0.3$ and $a = \sqrt{2}$ (solid line) and for Hagen-Poiseuille flow at $Re = 2500$. The computation refers to two different disturbance at $n = 1$: $k = 0.01$ and $k = 1$. The black line represents the axial component of velocity and the red and the blue lines represent respectively the azimuthal and radial ones. The energy associated to surface tension is not reported, since it is negligible.

shape of any initial perturbations is very similar to the one of the optimal perturbation, for which $t_0 = t_{\text{MAX}}$. On the other hand, for a three-dimensional disturbance ($n = 1$ and $k = 1$) the choice of t_0 influences much the evolution of the initial perturbations: the curves representing their energy density in fig. 3.14 have indeed a shape different from the maximum growth curve.

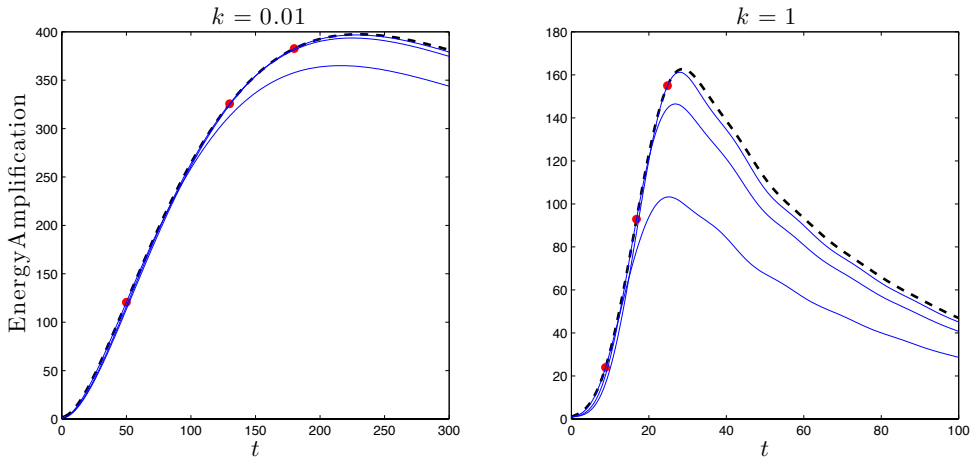

Figure 3.14: Maximum growth curve (dashed black line) and energy amplification of different initial disturbances (blue lines) tangent at the maximum growth curve at times marked by the red dots for $Re_m = 2500$, $m = 0.3$, $a = \sqrt{2}$, $n = 1$ and $k = 0.01$ (on the left) and $k = 1$ (on the right).

3.3 Comparison with experiments

In light of the results on transient growth in CAF discussed in the previous section, a review of the stability analysis made by Preziosi et al. [5] (PCJ), based on the experimental paper of [12], (CGH), is presented here. CGH identified a window of parameters that assure the stability of CAF to small disturbances, but they also observed two different type of flow instability: some situations in which the interface of CAF breaks up into bubble and slugs and others characterized by emulsifications or water drops in the oil. The analysis of PCJ can explain the first kind of the observed flow pattern as a result of a long wave instability due to surface tension (*capillary instability*) and the size of bubbles and slugs are given by the wavelength of the fastest growing wave. The second type of CAF instability, visible in the experiments 1, 5, 6, 9 and 10 of CGH, is unexplained by PCJ, as they state in their paper: "[...]The smaller water bubbles shown in Experiments 6 and 9 and the oil bubbles in Experiment 10 are unexplained by this analysis. They could arise as a reaction to turbulence in the water, or as kind of secondary instability of slugs."

The attention is focused in particular on the experiments 6, 9 and 10. These experiments are asymptotically unstable only for

♯	a	Re_1	l_{exp}	l_{th}	$\omega_{\text{i MAX}}^{\text{PCJ}}$	$\omega_{\text{i MAX}}$
6	1.5	406.90	>15.75	12.1856	$5.8597\text{x}10^{-3}$	$5.9524\text{x}10^{-3}$
9	1.81	795.97	6 or 15.75	66.3405	$5.3989\text{x}10^{-4}$	$5.3848\text{x}10^{-4}$
10	2.65	433.70	2.70	4.4199	$1.8272\text{x}10^{-2}$	$9.7256\text{x}10^{-4}$

Table 3.1: Comparison between the experiments of [12] here considered and the theory. $\omega_{\text{i MAX}}^{\text{PCJ}}$ is the maximum growth rate reported by [5] while $\omega_{\text{i MAX}}$ is the maximum growth rate calculated with our pseucospectral code using the *Golden Section Search* technique, with a 10^{-4} tolerance, to find the maximum and with $N = 170$ allocation points.

axisymmetric modes, $n = 0$. In fig. 3.15 the maximum growth rate is reported as a function of the axial wavenumber k: it is clearly visible that the maximum growth rates, in particular concerning the experiments 9 and 10, are very small in the dimensionless units employed here, $\mathcal{O}(10^{-4})$, so these disturbances need a very long time to grow significantly.

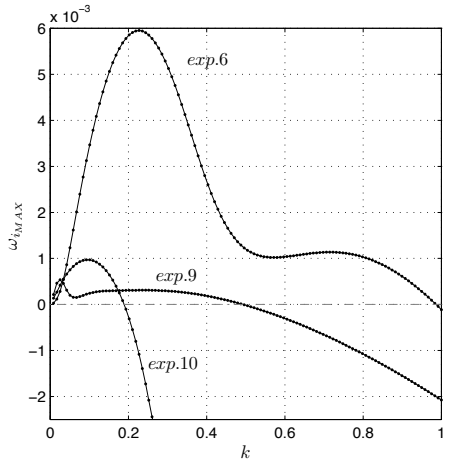

Figure 3.15: Maximum growth rate of the most unstable axisymmetric modes as a function of axial wavenumber k for the considered experiments of [12].

The color-map in fig. 3.16 reports the most unstable growth rate as a function of axial wavenumber and of Reynolds number of the core for the exp. 6. The continuous black line corresponds to the marginal stability curve computed with the used pseudospectral code (the 3×3 version), while the continuous blue line corresponds to the marginal stability calculated by PCJ. Their spectral code, based on a 3×3 system and on $N \geq 14$ allocation points, seems to fail at higher Reynolds number and at $k \geq 1$, but it is able to catch the disturbance that leads to the asymptotic instability. The values of the maximum growth rate found by PCJ are compared with the ones calculated by the 3×3 in table 3.1: there is a good agreement for exp. 6 and 9, but not for the exp. 10.

Experiment 6

The fig. 3.16 highlights that this flow is affected, for $n = 0$, by a Reynolds independent long-wave ($k \leq 1$) instability. The highest values of the maximum growth rate are concentrated in the low Re_1 region and are related to the so-called *interfacial mode*. As already discussed in section 2.3, this long-wave instability is induced by surface tension and represents a generalized capillary instability. PCJ conjectured that it is this instability to lead to the formation of oil slugs and bubbles in water.

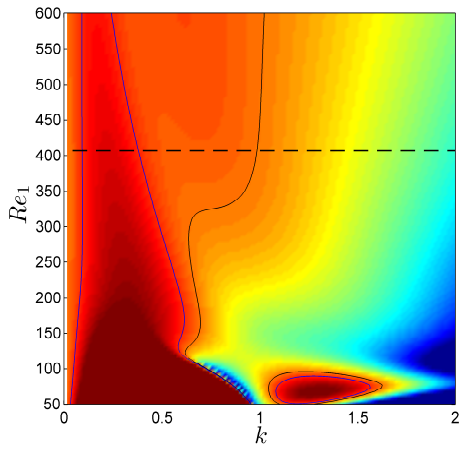

Figure 3.16: Maximum growth rate of the most unstable axisymmetric disturbances as a function of axial wavenumber k and Reynolds number of the core Re_1 for $a = 1.5$. The continuous black line correspond to the marginal stability curve obtained using our pseudospectral code while the continuous blue line correspond to the marginal stability curve reported by [5]. The dashed black line marks the Re_1 of exp. 6, $Re_1 = 406.9$.

The results of nonmodal analysis for the exp. 6 are reported in fig. 3.17. The color-maps in fig. 3.17-(a) represent the logarithm in base ten of the maximum value reached by the growth function, G_{MAX}, over different values of k and Re_1. For all the cases studied, long waves are affected by significant transient amplifications which increase with increasing Re_1 for non-axisymmetric disturbances. The maximum transient growth at the experiment conditions are reported in fig. 3.17-(b).

On the left of fig. 3.18 there is a comparison between the energy amplification of the disturbances that reach the maximum G_{MAX} at $n = 1, 2, 3$ and the most unstable axisymmetric mode. As just seen in fig. 3.8, one can observe that nonmodal mechanisms affect also the evolution of exponentially unstable modes at short times before the exponential growth sets in. Of course

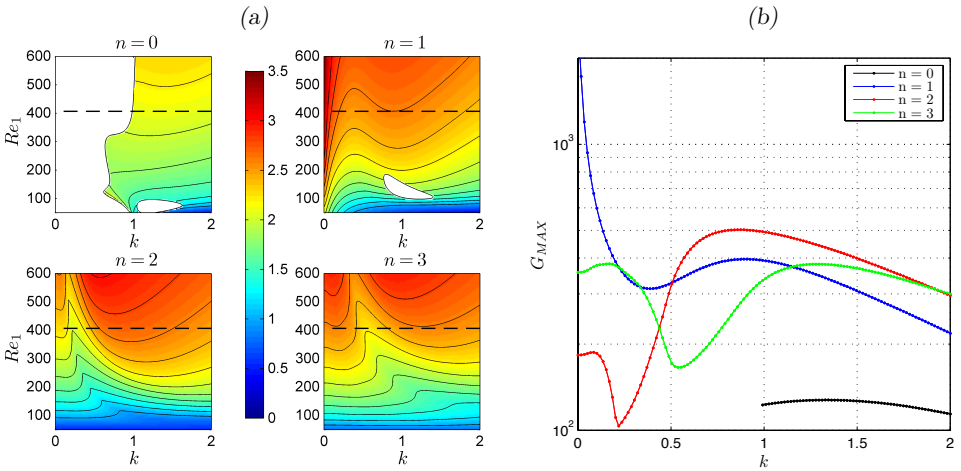

Figure 3.17: Fig.(a): Logarithm in base ten of maximum nonmodal amplification energy G_{MAX} as a function of axial wavenumber k and the Reynolds number Re_1 for $a = 1.5$. The blank areas represent the region of modal instability. Fig.(b): Logarithm in base ten of maximum nonmodal amplification energy G_{MAX} as a function of axial wavenumber k for the considered Reynolds number, $Re_1 = 406.9$, marked by a dashed black line in the fig.(a).

the effects on nonnormality mark more strongly the disturbances asymptotically stable that accumulate greater amounts of energy in a transient period. It is evident that for $n > 1$ the maximum of the growth function decreases, but these disturbances grow more rapidly in the initial stage of the amplification ([52], [8]).

Considering the optimal perturbation relative to the disturbance that reaches the highest level of energy in the shortest time, $k = 0.86242$ and $n = 2$, the evolution of the kinetic energy of the annulus and of the kinetic energy of the core are reported separately on the right of fig. 3.18: all the energy amplification is clearly related to the annulus. The energy associated to surface tension has not been reported since it is negligible.

As a further proof that the nonmodal energy amplifications are due to the water in the annulus, in fig. 3.19, on the left, is represented the ϵ-pseudospectrum at the conditions of exp. 6 for the $k = 0.86242$ $n = 2$ disturbance. The transient effects due to nonnormality can be better inferred from the pseudospectrum of the operator (see [53]): the figure clearly shows that the left branch of the spectrum, the one referred to the annulus, is affected by the more striking nonnormality. In particular this branch show the typical three-branch structure of the HP flow spectrum [20] and, as for HP flow, the eigenvalues at the intersection point of the

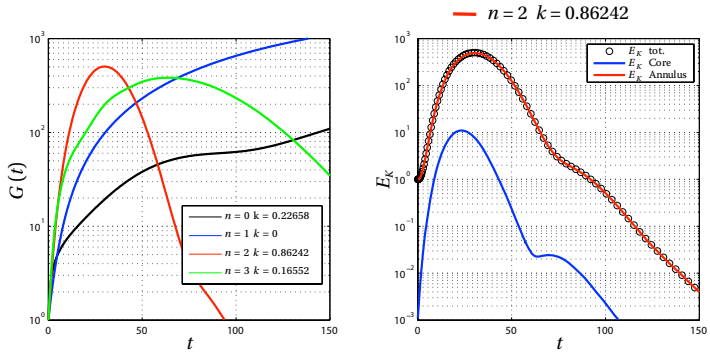

Figure 3.18: On the left: energy amplification of the perturbations that reach the highest value of G_{MAX} for $n > 0$ and of the most unstable mode for $n = 0$ at the condition of exp. 6: $Re_1 = 406.9$, $a = 1.5$. On the right: components of the energy amplification of the disturbance $n = 2$ $k = 0.86242$ (red line in fig. on the left). All the amplification is related to the kinetic energy, E_K, of the annulus.

three eigenvalue branch are the more sensible to nonnormality. On the right of fig. 3.19 there is an example of eigenvectors of the three velocity components related to the mode marked in blue.

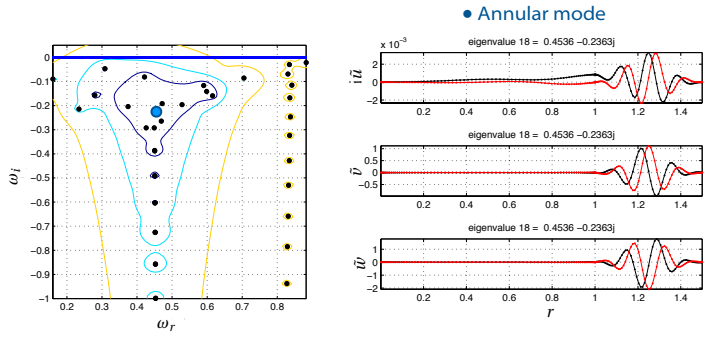

Figure 3.19: On the left: boundaries for the ϵ-pseudospectrum of the linearized operator for $Re_1 = 406.9, k = 0.86242$ and $n = 2$. From outside in, the curves correspond to $\epsilon = 10^{-2}, 10^{-3}, 10^{-4}$. It is evident how the nonnormality is concentrated in the branch of the spectrum representing the annulus. On the right: from top to bottom, the eigenfunctions correspond to the three velocity components, $i\tilde{u}, \tilde{v}, \tilde{w}$, referred to the eigenvalue marked in blue.

Experiment 9

The color-maps in fig. 3.20-(a) report the values of G as a function of the non dimensional time t and k for the conditions of the experiment 9. At short times the highest levels of energy amplification are reached by modal stable spiral disturbances characterized by long and mid-range wave, $k \leq 1$, while no relevant growth are present for $n = 0$ even at long times. Comparing this experimental situation with exp. 6, the Reynolds number and annulus radius are increased, $Re_1 = 795.97$, $a = 1.81$: these two parameters are there-

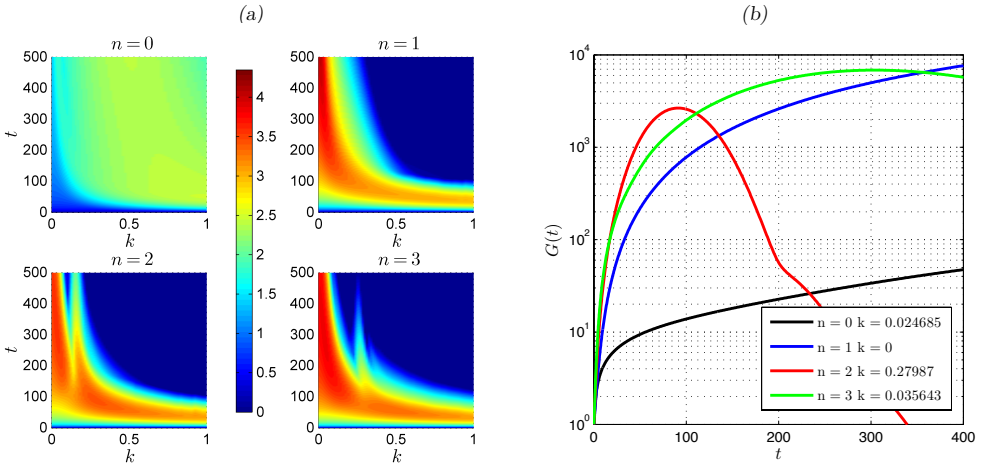

Figure 3.20: Fig.(a): Logarithm in base ten of energy amplification G as a function of non-dimensional time t and of axial wavenumber k at $Re_1 = 795.97$ and $a = 1.81$ (exp. 9). Fig.(b): Energy amplification of the perturbations that reach the highest value of G_{MAX} for $n > 0$ and of the most unstable mode for $n = 0$ at the condition of exp.9: $Re_1 = 795.97$, $a = 1.81$.

fore both responsible for the higher values of nonmodal energy amplification.

The transient growth of the perturbations that reach the maximum G_{MAX} are reported in fig. 3.20-(b) in which they are also compared with the most unstable mode, $k = 0.024685$ $n = 0$, whose level of energy is of two order smaller than the ones of spiral modes.

In fig.3.22 there is the ϵ-pseudospectrum of the disturbance that reaches the highest amplification of nonmodal energy at shortest time, $n = 2$ $k = 0.27987$, the red line in fig.3.20. As in the exp.6, the essence of nonnormality is localized in the left branch of the spectrum. The eigenvectors of the velocity components for three different modes are reported in the subsequent three images in fig. 3.22: clockwise we have the eigenvectors of the interfacial mode which leads to the asympotical instability, the eigenvectors of a core mode and the eigenvectors of an annular mode.

Also for the exp.9, both the separation of kinetic energy into the annulus and the core components in fig. 3.21, and the ϵ-pseudospectrum in fig. 3.22, show that the nonmodal instability is governed by the annulus.

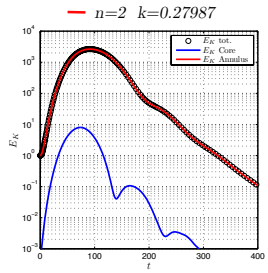

Figure 3.21: Components of the energy amplification of the disturbance $n = 2$ $k = 0.27987$ (the red line on the right of fig. 3.20).

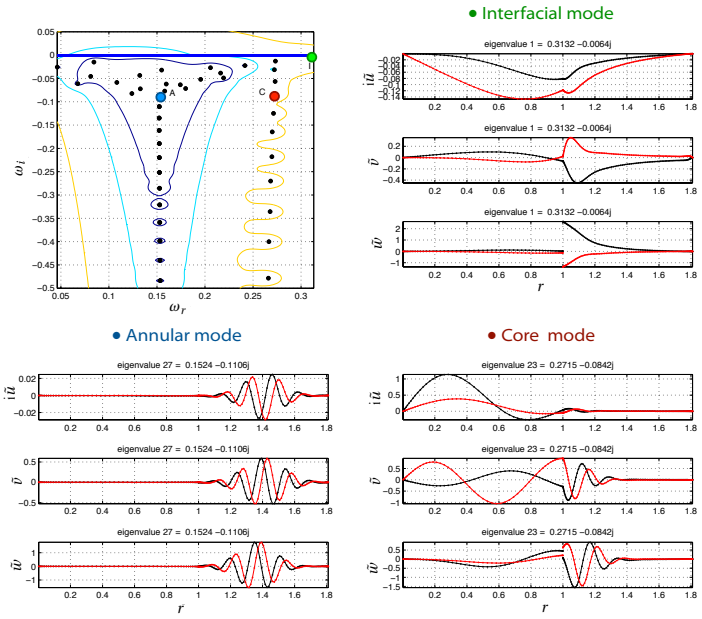

Figure 3.22: Boundaries for the ϵ-pseudospectrum of the linearized operator for $Re_1 = 795.97, k = 0.27987$ and $n = 2$. From outside in, the curves correspond to $\epsilon = 10^{-2}, 10^{-3}, 10^{-4}$. It is evident how the nonnormality is concentrated in the branch of the spectrum representing the annulus. Clockwise: eigenfunctions of the three velocity components, $i\tilde{u}, \tilde{v}, \tilde{w}$, referred to the eigenvalue I marked in green, *interfacial mode*; eigenfunctions of the three velocity components referred to the eigenvalue C marked in red, *core mode*; eigenfunctions of the three velocity components referred to the eigenvalue A marked in blue, *annular mode*.

Experiment 10

The same situation is observed for the conditions of exp. 10. Transient growth of different disturbances are compared on the left side of fig. 3.23. The maximum value of G is reached by $n = 1$ $k = 0$ disturbance; the components of its kinetic energy are reported on the right side of fig. 3.23 and in fig. 3.24 the ϵ-pseudospectrum linked to it. In this case the spectrum is markedly different from the previous, showing just one branch, and the ϵ-pseudospectrum extends into the unstable half-plane even for moderate contour levels.

For all the experimental conditions analyzed the largest amplification of nonmodal energy is for $n = 1$ and $k = 0$. The optimal perturbations obtained for this disturbance are shown in fig. 3.25. The perturbations reach their maximum intensity in the annulus region and increasing this area they tends to the classical structure found in HP flow: a pair of strong counter-rotating vortices. The longwave mechanism of energy growth in two-fluid system is hence the lift-up mechanism present in the single-fluid flow, as

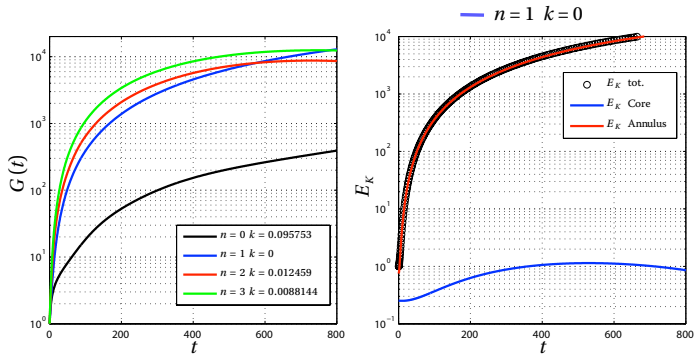

Figure 3.23: On the left: energy amplification of the perturbations that reach the highest value of G_{MAX} for $n > 0$ and of the most unstable mode for $n = 0$ at the condition of exp.10: $Re_1 = 433.7$, $a = 2.65$. On the right: components of the energy amplification of the disturbance $n = 1$ $k = 0$ (the blue line on the left). All the amplification is related to the kinetic energy, E_{K}, of the annulus.

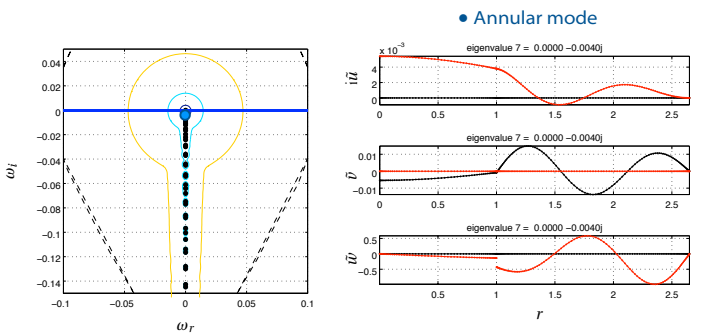

Figure 3.24: On the left: boundaries for the ϵ-pseudospectrum of the linearized operator for $Re_1 = 433.7, k = 0$ and $n = 1$. From outside in, the curves correspond to $\epsilon = 10^{-2}, 10^{-3}, 10^{-4}$ and the dashed line represents the boundary of the numerical range. On the right: eigenfunctions of the three velocity components, $i\,\tilde{u}, \tilde{v}, \tilde{w}$, referred to the eigenvalue marked in blue.

reported into commenting fig. 3.11, in which it has been showed that the amplification of this kind of disturbances is overall due to the growth of the streamwise velocity component.

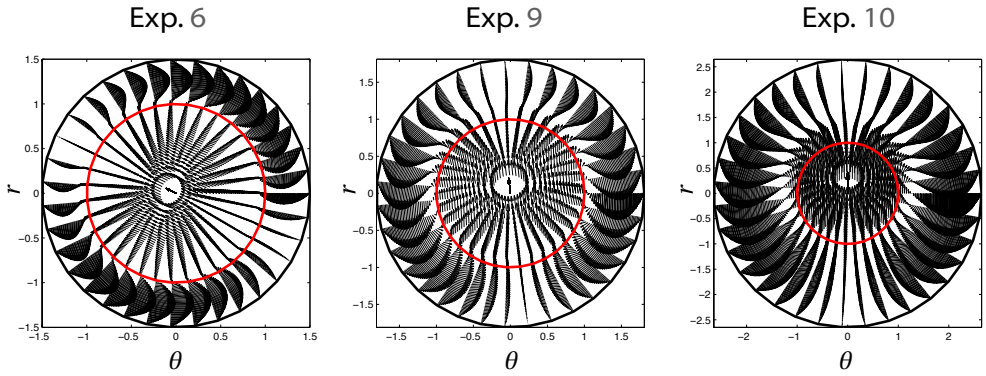

Figure 3.25: Optimal perturbations for $n = 1$ and $k = 0$ for the three experimental conditions considered.

3.4 Concluding remarks

In this chapter the problem of the linear stability of the horizontal pipe flow of an equal density oil-water mixture, arranged as a Core-Annular Flow, has been reconsidered from the point of view of nonmodal analysis in order to asses the effects of nonnormality of the linearized Navier-Stokes operator on transient evolution of small perturbations. The aim of this investigation has been to analyze the cases in which poor agreement occurs between the predictions of linear modal theory and the classical experiments of CGH.

The presence of remarkable levels of transient growth has been found for both asymptotically stable and unstable configurations. In particular the parameter studies have revealed that the maximum amplification of initial energy is experienced by disturbances with no streamwise dependence ($n = 1$ and $k = 0$, two-dimensional planar disturbances) in analogy with HP flow.

As demonstrated by analyzing both the ϵ-pseudospectrum and the division of kinetic energy into the core and the annulus components, the energy growth is correlated to the water in the

annulus and it reaches higher values increasing the radius and/or the Reynolds number of this region.

The viscosity ratios used for the present analysis are not very relevant for lubricated pipelining applications (m in practice is less than 0.002, as showed in the more recent experiments of Sotgia et al. [54]), anyway, from fig. 3.26, it is possible to see how the present analysis is conservative since G_{MAX} increases decreasing the value of m .

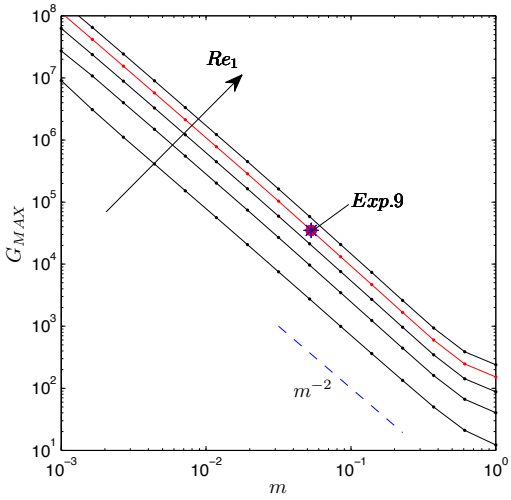

Figure 3.26: Curves of G_{MAX} as a function of the viscosity ratio m for different Re_1 and for $a = 1.81$. The curve in red corresponds to $Re_1 = 795.97$ and the point starred in blue represents the conditions of exp.9. Decreasing the value of m, and so increasing the value of the Reynolds number of the annulus, Re_2, G_{MAX} scales perfectly with $m^{-2} \sim Re_2^2$.

Moreover in this fig. the classic quadratic scaling of G_{MAX} with $1/m \sim Re_2$, typical of shear flows close to the transition, is clearly visible. Therefore these linear transient mechanisms may have significant implications to explain the transition to turbulence of CAF, and, stated their nature, they allow to reinforce the conjecture of PCJ that in CAF the transition to turbulence is due to the water in the annulus.

4

Conclusions

A concluding summary is proposed as an overview of the main results reported in this thesis.

Accurately predicting and understanding the behavior of two-fluid flows is a problem of great industrial and scientific interest. In this thesis an analysis of instabilities affecting these flows has been carried out with particular attention to atomization process and lubricating pipelining.

In chapter 2 gas-liquid flows have been investigated by means of both VOF simulations and linear stability theory in conditions very close to those of atomization experiments. Actually, only a part of the atomization process has been considered: the formation of a liquid film and its primary breakup.

Generally a liquid film of fuel is exposed to an high-velocity gas flow that induces perturbations at the interface. These perturbations quickly grow becoming nonlinear and producing ligaments that eventually break into drops. The instability governing this mechanism is a Kelvin-Helmholtz (KH) instability modfied by viscous and nonlinear effects, as proved by VOF simulations. They have shown the emergence and the evolution of a single nonlinear KH wave in two different flow configurations. This structure is fundamental to understand how drops are produced, because allows to analyze the behavior of a single ligament. The KH single wave has been deeply characterized in terms of propagation

velocity and amplification law through simple analytical models.

An useful tool to figure out the physical properties of the leading primary instability mechanisms is the linear stability analysis. Its results usually display a good agreement with numerical simulations at early times, before that nonlinear effects take the control. Indeed, linear theory has allowed to verify that the instability emerging in simulations is mainly due to the viscosity jump at the interface. This jump produces the vorticity at the base of the so-called interfacial mode. It has been seen that in particular flow conditions an interfacial mode may be combined with a Tollmien-Schlichting mode, present also in single-fluid flows, giving rise to a new mode, peculiar of two-fluid flows.

In chapter 3 an oil-water flow in a horizontal circular pipe, arranged as Core-Annular Flow (CAF), has been analyzed using linear nonmodal theory.

This flow is of importance in petroleum industry since significant savings in pumping power can be derived from the water-lubricated transportation of crude oil. Therefore, in order to identify the range of parameters suitable for application, the physical understanding of the phenomena that could bring to an instability of CAF is of great interest.

A linear nonmodal analysis has let go beyond the results already present in literature and figure out the mechanisms that lead to particular flow configurations. Linear modal analysis is only able to justify the formation of regular structures, such as oil bubbles and slugs, due to axisymmetric disturbances, but it cannot explain some irregular flow patterns characterized by emulsification or water drops in oil.

A detailed investigation, conducted in wide regions of parameters space, has highlighted the occurrence of remarkable transient growth for both asymptotically stable and unstable configurations. A study of characteristic times of modal and nonmodal mechanisms has demonstrated that at intermediate times the highest levels of energy amplification are reached by stable spiral disturbances well before that the slow exponentially unstable axisymmetric disturbances reach a sufficiently high amplitude.

It has been verified that the range of physical parameters in

which such temporal separation between exponentially stable and unstable disturbances occurs, correspond to the experimental findings unexplained by modal analysis.

Optimal perturbations have been determined. Their structure exhibits many analogies with the ones typical of Hagen-Poiseuille flow. In particular they are characterized by a streamwise independence and almost all the energy amplification is related to the streamwise component of the perturbation velocity.

At last, regarding the ϵ-pseudospectra, the structure of optimal perturbations and the different amounts of kinetic energy referred to the core and to the annulus of the spiral disturbances with the highest transient growth, it is clear that the transient mechanisms of energy amplification are correlated to the annulus. Moreover, the quadratic dependence of the maximum of transient growth on the Reynolds number of the annulus may represent a further proof that the water plays an important role in the transition to turbulence.

Bibliography

[1] P. Yecko. Disturbance growth in two-fluid channel flow: the role of capillarity. *Int. J. Multiphase Flow*, 34:272–282, 2008.

[2] M. J. South and A. P. Hooper. Linear growth in two-fluid plane Poiseuille flow. *J. Fluid Mech.*, 381:121–139, 1999.

[3] B. Lafaurie, C. Nardone, R. Scardovelli, S. Zaleski, and G. Zanetti. Modelling merging and fragmentation in multiphase flow with SURFER. *J. Comput. Phys.*, 113:134–147, 1994.

[4] S. Popinet. An accurate adaptive solver for surface-tension driven interfacial flow. *J. Comp. Phys.*, 228:5838–5866, 2009.

[5] L. Preziosi, K. Chen, and D. D. Joseph. Lubricated pipelining: stability of Core-Annular Flow. *J. Fluid Mech.*, 201:323–356, 1989.

[6] J. Eggers and E. Villermaux. Physics of liquid jets. *Rep. Prog. Phys.*, 71:036601, 2008.

[7] G. Tryggvason, R. Scardovelli, and S. Zaleski. *Direct Numerical Simulation of Gas-Liquid Multiphase Flow*. Cambridge University Press.

[8] P. J. Schmid and D. S. Henningson. Optimal energy density growth in Hagen-Poiseuille flow. *J. Fluid Mech.*, 277:197–225, 1994.

[9] A. Orazzo and J. Hœpffner. The evolution of a localized nonlinear wave of the Kelvin-Helmholtz instability with gravity. *Phys. Fluids*, 24:112106, 2012.

[10] A. Orazzo, G. Coppola, and L. de Luca. Single-wave Kelvin-Helmholtz instability in nonparallel channel flow. *Atomization Sprays*, 21:775–785, 2011.

[11] G. Coppola, A. Orazzo, and L. de Luca. Non-Modal Instability of Core-Annular Flow. *Int. J. Nonlinear Sci. Numer. Simul.*, 13:405–415, 2012.

[12] M. E. Charles, G. W. Govier, and G. W. Hodgson. The horizontal pipeline flow of equal density oil-water mixtures. *Can. J. Chem. Eng.*, 39:17–36, 1961.

[13] J. Koplik, J. R. Banavar, and J. F. Willemsen. Molecular dynamics of Poiseuille flow and moving contact line. *Phys. Rev. Lett.*, 60:1282–1285, 1988.

[14] P. S. Laplace. *Oeuvres complètes de Laplace, tome IV*. 1805.

[15] P. G. Drazin. *Introduction to Hydrodynamics Stability*. Cambridge University Press, 2002.

[16] Chian-Shun Yih. Instability due to viscosity stratification. *J. Fluid Mech.*, 27:337–352, 1967.

[17] Serkan Özgen. Coalescence of Tollmien-Schlichting and interfacial modes of instability in two–fluids flows. *Phys. Fluids*, 20:044108, 2008.

[18] Y. Renardy. Instability at the interface between two shearing fluids in a channel. *Phys. Fluids*, 28:3441, 1985.

[19] A. P. Hooper and W. G. C. Boyd. Shear-flow instability at the interface between two viscous fluids. *J. Fluid Mech.*, 128:507, 1982.

[20] P. J. Schmid and D. S. Henningson. *Stability and transition in shear flow*. Springer, 2001.

[21] S. Malik and A. P. Hooper. Three-dimensional disturbances in channel flows. *Phys. Fluids*, 19:052102, 2007.

[22] L. N. Trefethen. *Pseudospectra of matrices*. Longman, 1992.

[23] J. A. Weideman and S. C. Reddy. A MATLAB differentiation matrix suite. *ACM Transaction on Mathematical Software*, 26: 465–519, 2000.

[24] J. P. Boyd. *Chebyshev and Fourier Spectral Methods*. DOVER Publications.

[25] L. N. Trefethen. Computation of pseudospectra. *Acta Numerica*, 8:247–295, 1999.

[26] C. W. Hirt and B. D. Nichols. Volume of fluid (VOF) method for the dynamics of free boundaries. *J. Comput. Phys.*, 39: 201–226, 1981.

[27] J. Li. Calcul d'interface affine par morceaux (piecewise linear interface calculation). *C. R. Acad. Sci. Paris*, 320:391–396, 1995.

[28] B. J. Parker and D. L. Youngs. *Two and three dimensional Eulerian simulation and fluid flow with material interface*. Atomic Weapons Establishment, Aldermaston, UK, 1992.

[29] J. E. Pilliod and E. G. Puckett. *Second order accurate volume-of-fluid algorithms for tracking material interfaces*. Lawrence Berkeley National Laboratory, 1997.

[30] D. Gueyffier, J. Li, A. Nadim, R. Scardovelli, and S. Zaleski. Volume-of-fluid interface tracking with smoothed surface stress methods for three-dimensional flows. *J. Comput. Phys.*, 152:423–456, 1998.

[31] J. Brackbill, D. B. Kothe, and C. Zemach. A continuum method for modeling surface tension. *J. Comput. Phys.*, 100: 335–354, 1992.

[32] R. Peyret and T. D. Taylor. *Computational method for fluid flow*. Springer-Verlag.

[33] S. Popinet. Gerris: a tree-based adaptive solver for the incompressible Euler equation in complex geometries. *J. Comput. Phys.*, 190:572–600, 2003.

[34] M. M. François, S. J. Cummis, E. D. Dendy, J. M. Sicilian, and M. W. Williams. A balaced-force algorithm for continuous and sharp interfacial surface tension models within a volume tracking framework. *J. Comput. Phys.*, 213:141–173, 2006.

[35] Y. Renardy and M. Renardy. PROST: A parabolic reconstruction of surface tension for the Volume-Of-Fluid Method. *J. Comp. Phys.*, 183:400–421, 2002.

[36] Hermann Helmholtz. On discontinuous movements of fluids. *Phil. Mag. series 4*, 36:337–346, 1868.

[37] William Thomson. Hydrokinetic solutions and observations. *Phil. Mag. series 4*, 42:362–377, 1871.

[38] J. Hœpffner, R. Blumenthal, and S. Zaleski. Self-similar wave produced by local perturbation of the Kelvin-Helmholtz shear-layer instability. *Phys. Rev. Lett.*, 106:104502, 2011.

[39] T. Funada and D. D. Joseph. Viscous potential flow analysis of Kelvin-Helmholtz instability in a channel. *J. Fluid Mech.*, 445:263–283, 2001.

[40] C .M. Varga, J. C. Lasheras, and E. J. Hopfinger. Initial breakup of a small-diameter liquid jet by a high-speed gas stream. *J. Fluid Mech.*, 497:405–434, 2003.

[41] P. E. Dimotakis. Two-dimensional shear-layer entrainment. *AIAA Journal*, 24:1791–1796, 1986.

[42] P. A. M. Boomkamp and R. H. M. Miesen. Classification of instabilities in parallel two-phase flow. *Int. J. Multiphase Flow*, 22:67–88, 1996.

[43] L. S. Cohen and T. J. Hanratty. Generation of waves in the concurrent flow of air and liquid. *AIChE Journal*, 11:138–144, 1965.

[44] D. L. MacLean. A theoretical analysis of bicomponent flow and the problem of interface shape. *Trans. Soc. Rheol.*, 17: 385–399, 1973.

[45] M. E. Charles and P. J. Redberger. The reduction of pressure gradients in oil pipelines by the addition of water: numerical analysis of stratified flow. *AIChE*, 1960.

[46] R. V. A. Oliemans and G. Ooms. Core-Annular Flow of oil and water through a pipeline. *Multiphase Science & Technology*, 2, 1986.

[47] C. E. Hickox. Instability due to viscosity and density stratification in axisymmetric pipe flow. *Phys. Fluids*, 14:251–262, 1971.

[48] D. D. Joseph, Y. Renardy, and M. Renardy. Instability of the flow of immiscible liquids with different viscosities in a pipe. *J. Fluid Mech.*, 141:309–317, 1985.

[49] D. D. Joseph and Y. Y. Renardy. *Fundamentals of two-fluids dynamics*. Springer–Verlag, 1993.

[50] K. Chen and D. D. Joseph. Lubricated pipelining: stability of core–annular flow. Part 4. Ginzburg-Landau equations. *J. Fluid Mech.*, 227:226–260, 1991.

[51] R. L. Ash and M. R. Khorrami. "Vortex Stability" in *Fluid Vortices*. pages 317–372. Kluwer, 1995.

[52] Lars Bergstrom. Optimal growth of small disturbances in pipe flow. *Phys. Fluids*, 5:2710–2720, 1993.

[53] A. Meseguer and L. N. Trefethen. Linearized pipe flow to Reynolds number 10^7. *J. Comp. Phys.*, 186:178–197, 2003.

[54] G. Sotgia, P. Tartarini, and E. Stalio. Experimental analysis of flow regimes and pressure drop reduction in oil-water mixtures. *Int. J. Multiphase Flow*, 34:1161–1174, 2008.